AD-783 329

RESEARCH IN SEISMOLOGY

Frank Press, et al

Massachusetts Institute of Technology

Prepared for:

Air Force Office of Scientific Research
Advanced Research Projects Agency

1974

ia

REPORT DOCUMENTATION PAGE		READ INSTRUCTIONS BEFORE COMPLETING FORM
1. REPORT NUMBER AFOSR - TR -74 -1254	2. GOVT ACCESSION NO.	3. RECIPIENT'S CATALOG NUMBER AD 783329
4. TITLE (and Subtitle) RESEARCH IN SEISMOLOGY		5. TYPE OF REPORT & PERIOD COVERED Interim 4/1/73 - 3/31/74
		6. PERFORMING ORG. REPORT NUMBER
7. AUTHOR(s) Frank Press Keiiti Aki M. Nafi Toksöz Sean C. Solomon		8. CONTRACT OR GRANT NUMBER(s) F44620-71-C-0049
9. PERFORMING ORGANIZATION NAME AND ADDRESS Massachusetts Institute of Technology Cambridge, MA 02139		10. PROGRAM ELEMENT, PROJECT, TASK AREA & WORK UNIT NUMBERS 62701E AO 1827-10
11. CONTROLLING OFFICE NAME AND ADDRESS Advanced Research Projects Agency/NMR 1400 Wilson Boulevard Arlington, VA 22209		12. REPORT DATE ▬▬▬, 1974
		13. NUMBER OF PAGES 187
14. MONITORING AGENCY NAME & ADDRESS(If different from Controlling Office) Air Force Office of Scientific Research/NP 1400 Wilson Boulevard Arlington, VA 22209		15. SECURITY CLASS. (of this report) UNCLASSIFIED
		15a. DECLASSIFICATION/DOWNGRADING SCHEDULE

16. DISTRIBUTION STATEMENT (of this Report)

Approved for public release, distribution unlimited.

17. DISTRIBUTION STATEMENT (of the abstract entered in Block 20, if different from Report)

18. SUPPLEMENTARY NOTES

19. KEY WORDS (Continue on reverse side if necessary and identify by block number)

Attenuation	Seismic arrays	Surface waves
Body waves	Seismic discrimination	Wave propagation
Earthquakes	Seismology	
Earth structure	Source mechanism	

20. ABSTRACT (Continue on reverse side if necessary and identify by block number)
This report summarizes work conducted during the last year under the contract Research in Seismology. These investigations fall within the four broad topics: (1) Theoretical and observational studies of source mechanisms of earthquakes and underground nuclear explosions; (2) Wave propagation in heterogeneous and anisotropic media; (3) Regionalization of earth structure; (4) Array and data processing techniques for event detection and location. All publications and theses completed during the contract year are listed.

DD FORM 1473 1 JAN 73   EDITION OF 1 NOV 65 IS OBSOLETE

Department of Earth and Planetary Sciences

Massachusetts Institute of Technology

Cambridge, Massachusetts   02139

RESEARCH IN SEISMOLOGY

Annual Report to

Air Force Office of Scientific Research

1 April 1973 - 31 March 1974

ib

ABSTRACT

This report summarizes work conducted during the last year under the contract Research in Seismology. These investigations fall within the four broad topics: (1) Theoretical and observational studies of source mechanisms of earthquakes and underground nuclear explosions; (2) Wave propagation in heterogeneous and anisotropic media; (3) Regionalization of earth structure; (4) Array and data processing techniques for event detection and location. All publications and theses completed during the contract year are listed.

TABLE OF CONTENTS

1. SUMMARY

In this annual report we review work completed under
the contract Research in Seismology during the year
1 April 1973 through 31 March 1974. Within the broader
problem of discriminating earthquakes from underground
nuclear explosions, we have conducted a number of specific
investigations of seismic source and wave propagation
studies.

The problems considered can be grouped into four
major subject areas:

    (1)   Source mechanisms of earthquakes and explosions

    (2)   Seismic wave propagation

    (3)   Earth structure

    (4)   Arrays and data processing

In the following sections we include abstracts of papers
in each category either published or soon to be published.
Recently completed work is discussed in greater detail.
We also list all publications and theses supported under
this project during the contract year.

A major fraction of our effort was devoted to continuing
our theoretical and observational studies of the source
mechanisms of earthquakes and underground nuclear explosions.
Work by Abe on two earthquakes in Japan and by Aki and co-
workers on NTS explosions demonstrated the powerful insight
possible by combining careful near-field and far-field
observations of seismic sources. A very important result
of the study of Aki and others was that the reduced

displacement potential for nuclear explosions is closer to
an impulse than to a step function, providing an explana-
tion for the success of the M_s - m_b discrimination criterion
for events of $m_b \geq 4$.

Other work on seismic source phenomena included Brown's
study of premonitory changes in seismic wave velocities in
the source region of strike-slip earthquakes in Japan,
continuation by Singh and Rosenman of their calculations
of displacements and stresses associated with various
sources in a viscoelastic earth, and Richter and Johnson's
novel explanation for very deep earthquakes as associated
with standing waves on a mineralogical/chemical transition
boundary at 650 km depth in the mantle.

Several wave propagation studies were completed. Wang
solved the problem of wave propagation in weakly anisotropic
media for certain geometries of wave paths and symmetry
directions, with direct application to Rayleigh and P_n waves
in the oceanic upper mantle. Reasenberg and Aki measured
changes in the in situ seismic velocity in the shallow crust
due to tidal stresses. Kuster and Toksöz derived the elas-
tic moduli of a two-phase medium using a wave-scattering
approach, and applied their model to rocks with dry and
water-saturated cracks.

Much of our attention was devoted to regionalization
of earth structure, particularly to the study of areas
within and adjacent to Asia. In his M.S. thesis, Chapman

measured the dispersion characteristics of Rayleigh waves in the Arctic Ocean region and inferred the crustal structure beneath the Arctic Ocean basin, the spreading Nansen ridge and the continental shelves. He also interpreted earthquakes in northeast Asia as due to interaction between the Eurasian and American plates. Solomon and Butler outlined a procedure for locating seismically inactive slabs of subducted lithosphere by use of travel-time residuals; the technique may be useful in looking for such an ancient slab proposed to lie beneath the Urals. Solomon and Julian studied the effects on body-wave propagation paths of the laterally heterogeneous velocity structure beneath active spreading centers. Such effects can explain the observation that normal-faulting earthquakes on ridge crests appear from first-motion diagrams to be accompanied by a superimposed 'explosion' source.

In the area of arrays and data processing, Shlien and Toksöz extended their automatic phase identification algorithms for array data to make use of two arrays running concurrently. The techniques were tested on LASA and NORSAR records. Ambuter and Solomon built a seismic recording package using an event-recording scheme based on a continuously updated semiconductor memory; the scheme results in far less storage capacity and easier later interpretation than do conventional continuous recording methods.

2. SOURCE MECHANISMS OF EARTHQUAKES AND EXPLOSIONS

2.1 Seismic Source Function for an Underground Nuclear Explosion by Keiiti Aki, Michel Bouchon, and Paul Reasenberg (abstract)

The reduced displacement potential obtained from close-in observation of seismic displacement during an underground explosion usually takes the form of a step function with or without a small overshoot. Theoretical prediction by shock-wave calculation appears to agree with the close-in data. The step-function source has also been supported by the observations on Rayleigh waves at periods longer than 10 sec. We found, however, some inconsistency between the published data on residual potentials obtained from close-in data and those on seismic moments obtained from long-period Rayleigh waves. It appears that only about 1/3 of the residual potential is transmitted to the far-field at long periods. This discrepancy is, however, consistent with several observations made on teleseismic signals suggesting an impulse rather than a step as the primary form of the potential function. New observations of the two NTS events at distances 2.6 to 7.8 km using wide dynamic range, wide-band accelerometers, combined with data from the far-field, support a large overshoot 4 to 5 times the residual value. This result accounts for the efficiency of the M_s- m_b discriminant between earthquakes and explosions with m_b

around 4 and greater. The compaction of the source volume
by spalling was suggested as a possible mechanism for the
large overshoot.

2.2 Precursory Changes in VP/VS Before Strike-slip Events

by Raymon Brown (abstract)

P and S-wave travel time data collected in southwestern
Japan by means of a five station microearthquake array are
used to construct Wadati plots. The slopes of these plots
(VP/VS-1) are then examined as a function of time. The
largest deviations of VP/VS are of the order of 5%. The mag-
nitude of any premonitory changes in VP/VS observed here
will therefore be less than any previously reported. Two
of the largest events recorded by the array (M = 5.0) for
which there is enough data show a premonitory increase above
the mean and then a decrease below the mean and finally a
rise to the mean shortly before the event. The nature of
the changes before both events agree in magnitude and time.
The time from the minimum VP/VS to the time of the events
scales in agreement with previous investigations. The
region of Japan studied in this paper is one characterized
by shallow, predominantly strike-slip events.

2.3 <u>Stress Relaxation in a Semi-Infinite Viscoelastic Earth Model</u> by Martin Rosenman and Sarva Jit Singh (abstract)

Expressions for quasi-static surface stresses resulting from a finite, rectangular, vertical, strike-slip fault in a Maxwellian viscoelastic half-space are derived. Contour maps are obtained in some representative cases. It is found that all nonvanishing stress components at the free surface die exponentially with time. This is in contrast to the behavior of the displacements and strains which, in general, do not vanish for large times.

2.4 <u>Stability of a Chemically Layered Mantle</u> by Frank M. Richter and Carl E. Johnson (abstract)

A system of two immiscible fluid layers and heated from below is analyzed to determine its stability to convective motions. The model is applicable to the mantle if some fraction of the density increase with depth results from changes in chemical composition. For different parameter ranges, three modes of instability are possible: (1) convection of the entire depth of the fluid, (2) separate convection within each layer, and (3) overstability in the form of standing waves on the interface between layers. Earth models that include an increase in density due to iron enrichment below 650 km suggest that mantle convection

can exist above and below but not through the 650-km level.
The model results are combined with a prior understanding
of mineralogical phase changes to suggest a possible
mechanism for the deepest earthquakes.

2.5 Seismic Displacement and Ground Motion Near a Fault: The Saitama Earthquake of September 21, 1931 by Katsuyuki Abe (abstract)

The dislocation parameters of the Saitama earthquake
(M = 7.0, 36.15°N, 139.24°E) of September 21, 1931, are
determined on the basis of the first-motion data, the
aftershock area, and the close-in seismograms obtained by
a low-magnification seismograph. The earthquake represents
a left-lateral strike-slip faulting on a plane, dipping
80° towards N 196°E, with the size of 20 km (length) x 10 km
(width). The strike of the fault plane is found to be
almost parallel to that of the eastern extension of the
Median Tectonic Line. A synthetic study suggests that the
rupture grows bilaterally at a velocity of 2.3 km/sec.
The rise time and the final dislocation of the linear ramp
dislocation time function are determined as 2 sec and
100 cm, respectively. The corresponding particle velocity
of the fault dislocation is estimated to be 50 cm/sec.
The near-source ground displacements and ground motions
inferred from the above seismic fault model are found to

be remarkably consistent with the data on the high precision levelling and on the field survey on the direction to which artificial structures collapsed.

2.6 Fault Parameters Determined by Near- and Far-Field Data: The Wakasa-Bay Earthquake of March 26, 1963 by Katsuyuki Abe

Summary

The source process of the Wakasa-Bay earthquake (M = 6.9, 35.80°N, 135.76°E, depth 4 km) which occurred near the west coast of Honshu Island, Japan, on March 26, 1963, is studied on the basis of the seismological data. Dynamic and static parameters of the faulting are determined by directly comparing synthetic seismograms with observed seismograms recorded at seismic near and far distances. The De Hoop-Haskell method is used for the synthesis. The average dislocation is determined to be 60 cm. The overall dislocation velocity is estimated to be 30 cm/sec, the rise time of the slip dislocation being determined as 2 sec. The other fault parameters determined, with supplementary data on the P-wave first motion, the S-wave polarization angle and the aftershocks, are: source geometry, dip direction N 144°E, dip angle 68°, slip angle 22° (right-lateral strike-slip motion with some dip-slip component);

fault dimension, 20 km length x 8 km width; rupture velocity, 2.3 km/sec (bilateral); seismic moment, 3.3×10^{25} dyne cm; stress drop, 32 bars. The effective stress available to accelerate the fault motion is estimated to be about 40 bars. The approximate agreement between the effective stress and the stress drop suggests that most of the effective stress was released at the time of the earthquake.

1. Introduction

One of the most important factors in the dynamic process of faulting is a dislocation velocity. This dynamic parameter is directly related to the effective stress available to accelerate the fault motion. Such effective stress can be estimated from the dislocation velocity (e.g. Kanamori, 1972). Since the effective stress primarily controls the near-source acceleration (Brune, 1970), its estimate may provide the possible maximum ground acceleration expected of not only a certain earthquake but a future earthquake. As the determination of such dynamic parameters is so far very scanty, detailed study on the fault dynamics for individual earthquake is important not only for understanding the physics of earthquakes but also for providing the potential data for earthquake engineering.

From this point of view, we will attempt to determine, for the Wakasa-Bay earthquake of March 26, 1963, the dislocation velocity as well as various static parameters such as fault geometry, fault dimension and dislocation. The near-field seismograms as well as the far-field seismograms are available for this earthquake. Most of the fault parameters will be determined by means of a direct comparison between synthetic seismograms and observed seismograms.

2. The Wakasa-Bay earthquake of 1963

2.1. Redetermination of the hypocenter

The Wakasa-Bay earthquake (M = 6.9) occurred on
March 26, 1963, to the north of Kyoto, near the west coast
of Honshu island, Japan (see fig. 5). The hypocenters of
the main shock and the four large aftershocks (M = 4.8~5.2)
were redetermined on the basis of the P times as reported
in the Seismological Bulletin of the Japan Meteorological
Agency (JMA) and the International Seismological Center
(ISC) for the year 1963. The Jeffreys-Bullen travel-time
table was used. We made the relocation of the main shock
for two cases: (1) all the stations with epicentral
distance $\underline{\Delta} \leq 90°$ were used; (2) stations with $\underline{\Delta} \leq 11°$
were used. The stations used in the case (2) belong to JMA.
We used exclusively the JMA stations for the four aftershocks,
since the world-wide data are very scanty. In all cases
the threshold of the O-C residual (observed minus computed
P time) was set at 4 sec: as a result for the main shock,
three data were discarded in the first case, and five data
were discarded in the second case. The number of stations
included in each set is shown in the inset of fig. 1. Also
shown is the number of stations located in NE, SE, SW and
NW quadrants around the epicenter.

The root-mean-square (RMS) of the O-C residuals

for various restrained depths are shown in fig. 1, where
the stability of the depth determination is shown. The RMS
of O-C was found to increase as the depth increased,
favoring a shallow focal depth. However, it is well known
that the focal depth cannot be constrained very well for P
times alone. The residuals at nearby stations are strongly
affected by the focal depth. This feature is demonstrated
in fig. 2, where the O-C residuals at nearby stations with
$\Delta \leq 1°$ are given for five focal depths. It is evident that
the O-C residuals increase systematically and sharply as
the depth increased. These observations lead to a conclusion
that the foci of the main shock and the aftershocks are
very shallow, not deeper than 10 km. In the following, we
will use, for the main shock, the hypocenter parameters
determined for the second case: origin time $21^h 34^m 38.5^s$;
latitude 35.80°N; longitude 135.76°E; depth 4 km. Fig. 3
shows the epicenters of the main shock and the aftershocks
which occurred within twenty-four hours after the main
shock. The epicenter data except for the shocks treated
above are taken from the bulletin of JMA.

2.2. Source geometry

The source geometry of the main shock was determined
by Ichikawa (1971) who used the P-wave first-motion data
reported in various seismological bulletins, and

tentatively by Stauder and Bollinger (1965) who used mainly
the S-wave polarization angle data. As the hypocenter is
redetermined here, we anew determine the source geometry.

The first-motion data of P waves are obtained from
the long-period seismograms from the World Wide Standard
Station Network (WWSSN). We supplement them by the data
reported in the Seismological Bulletin of JMA and the data
given by Stauder and Bollinger (1965). These data are
plotted on the Wulff grid as shown in fig. 4. The lower
hemisphere of the focal sphere was projected. Though two
nodal planes can be defined by the compression and dilatation
fields, we introduce the S-wave data to find a more precise
source-geometry. The 15 data of polarization angle are
taken from Stauder and Bollinger (1965), in which the
polarization angles were determined from particle motion
diagrams of S phase recorded on WWSSN seismograms. We used
Hirasawa's (1966) method. The focal depth of the earthquake
is placed at 4 km. The two nodal planes thus determined
are remarkably consistent with the P wave data as shown in
fig. 4 by solid lines. The dip direction, the dip angle
and the slip angle are: $\underline{\phi} = 144°$, $\underline{\delta} = 68°$, $\underline{\lambda} = 22°$ for
one plane and $\underline{\phi} = 243°$, $\underline{\delta} = 69°$, $\underline{\lambda} = 156°$ for another
plane. The standard deviation of the polarization angles
is 23°. Although some inconsistent data exist in the
P-wave first motions, the present solution is believed to

be very good as far as both the first motion and the polarization angle data are concerned.

From the mechanism diagram alone, it is not possible to select the actual fault plane out of the orthogonal nodal planes. The spatial distribution of the aftershock provides the key to the selection. The after-shocks are distributed at relatively shallow depths and over the area elongated in a northeast-southwest direction (fig. 3). The aftershocks are more densely distributed to the south-east of the main shock epicenter than to the north-west, suggesting the fault dipping to the south-east. It follows that the actual dislocation took place over the plane striking in N 54°E and with a dip angle of 68°SE. The size of the fault plane is estimated as 20 km length x 8 km width from the extent of the aftershock area. The present solution suggests that the earthquake represents an almost right-lateral strike-slip faulting with some dip-slip component.

3. Interpretation of near-field seismograms

3.1. Data and method of analysis

Records of a near-source ground motion were obtained at Maizuru observatory, 50 km away from the epicenter, and Abuyama observatory, 106 km away from the epicenter. Fig. 5 shows the locations of the earthquake and the observatories.

The instrument operated at Maizuru observatory is a strong-motion seismograph with a low magnification: its constants are always fixed to be To (free period of pendulum) = 6.0 sec, ε (damping ratio) = 8, and V (static magnification) = 1.0. The instrument operated at Abuyama observatory is a low-magnification and long-period seismograph: the seismogram includes a calibration pulse from which the instrumental constants can be determined as To = 28 sec, ε = 2.3 and V = 1.1. The seismograms are shown in fig. 6.

In order to obtain fault parameters, we computed synthetic seismograms for various fault models and compared them with the observed seismograms. In computing the dynamic near-field displacement the integral expressions given by Haskell (1969) were numerically double-integrated over a fault plane (see also, De Hoop, 1958). It is assumed that the dislocation takes place simultaneously over the fault width w and propagates at a constant velocity v along the fault length. The temporal variation of the dislocation is given as the form of a ramp function of rise time τ, that is

$$G(t) = \begin{cases} 0 & t < 0 \\ t / \tau & 0 \leq t \leq \tau \\ 1 & t > \tau \end{cases} \qquad (1)$$

Since the method applies only to an infinite homogeneous medium, the comparison should be made only for the first several cycles of body waves. A free-surface effect was included simply by doubling the amplitude calculated for an infinite medium. Velocities of P and S waves are placed at 6.0 km/sec and 3.5 km/sec, respectively.

3.2 Interpretation

In subsequent calculations, we assume several fault parameters as follows: $\phi = 144°$, $\delta = 68°$, $L = 20$ km, $w = 8$ km. From fig. 3 the rupture is considered to start at the center of the fault, and to propagate bilaterally along the strike of the fault. With these constraint we can finally control the rupture velocity, the rise time, and the final dislocation.

From the tentative examination of radiation patterns, Maizuru is found to be located near the loop direction for S waves, and near the node direction for P waves. On the other hand, Abuyama is found to be located nearest to the node direction for S waves: the predominant wave following P waves may be considered to be surface waves, probably Rayleigh waves, in view of the late arrival time. On these grounds we use only the S wave portion for the Maizuru record, and the P wave portion for the Abuyama record, for a reliable estimate of fault parameters.

Various combinations of rise times (1, 2, 3, 4, 5 sec) and rupture velocities (1.0, 1.5, 2.3, 3.0, 3.4 km/sec) are assumed in an attempt to deduce the most probable values. Synthetic seismograms are given in fig. 7, for several combinations of rise time and rupture velocity. A rise time and a rupture velocity affect mainly the initial slope and duration time, respectively. Comparison with the observed data suggests that combinations of a rise time of 2 sec and a rupture velocity near 2.3 km/sec provide an overall agreement. The amount of the dislocation is independent of the nature of the wave form, and it simply scales the amplitude. The observed seismograms are compared, in amplitude, with the synthetic seismograms calculated for $\tau = 2$ sec and $v = 2.3$ km/sec. We obtain the dislocation of 62 cm and 68 cm for the Maizuru and Abuyama records, respectively; the average is 65 cm.

Although the dislocation simply scales the amplitude, the amplitude is very sensitive to both the rupture velocity and the rise time. For example, the amplitude tends to increase with the rupture velocity increased, as shown in fig. 7. If the dislocation can be independently determined, the present estimate of v and τ may be fairly confirmed. From this reason we try to analyze far-field seismograms to determine the dislocation independently.

4. Interpretation of far-field seismograms

4.1. Data and method of analysis

The copies of the long-period seismograms from the WWSSN stations were collected. We used horizontal components for 7 S-waves, and vertical components for 12 P-waves. Fig. 8 shows the theoretical radiation pattern of P, SH and SV waves, and the azimuthal distribution of the stations used. It is to be noted in fig. 8 that the SH motion excels the SV motion in amplitude at a few stations located in both the north-east and north-west directions. With this geographical filter we exclusively used the S waves predominated by SH waves, in order to avoid any possible contamination which may result from reflection and refraction. The stations and other pertinent data used here are listed in Table 1.

For the interpretation of the seismograms, synthetic seismograms are computed for various propagating fault models. For the computation, we employed the Haskell's (1964) method which gives the far-field displacement in an infinite homogeneous medium. The setup of modeling a fault source is described in the preceding section. In the framework of this model, the far-field displacement can be expressed in a good approximation, as the form of a trapezoidal pulse by

$$\vec{u}_c = C \ (M_o/t_c) \ f(t; \ \tau \ , \ t_c) \tag{2}$$

where

$$C = \frac{\vec{R}_{\theta\varphi}^c}{4\pi\rho \, v_c^3} \tag{3}$$

$$f(t; \ \tau \ , \ t_c) = G(t - \frac{r_0}{v_c}) - G(t - \frac{r_0}{v_c} - t_c) \tag{4}$$

$$t_c = \frac{L}{v} (1 - \frac{v}{v_c} \cos\theta \ ) \tag{5}$$

In these expressions $\vec{u}_c$ = far-field displacement (suffix c denotes to P, SH, SV waves), M_o = seismic moment, $\vec{R}_{\theta\varphi}^c$ = radiation pattern, ρ density, v_c = wave velocity, r_0 = distance from the source origin, θ = angle between the ray path and rupture direction. The displacement source time function $G(t)$ is defined in eq. 1. $\underset{\wedge}{\ }$ Equation 4 is illustrated in fig. 9. Equation 2 is readily generalized to bilateral rupture by

$$\vec{u}_c = (C/2) \ M_o \left[\ f(t; \ \tau \ , \ t_c^1) \ / \ t_c^1 \right.$$

$$\left. + f(t; \ \tau \ , \ t_c^2) \ / \ t_c^2 \right] \tag{6}$$

where

$$t_c^1 = \frac{L}{2v} (1 - \frac{v}{v_c} \cos\theta \ ) \tag{7}$$

$$t_c^2 = \frac{L}{2v} (1 + \frac{v}{v_c} \cos\theta \ ) \tag{8}$$

For a direct comparison between synthetic and observed seismograms, various corrections must be included.

Such corrections take care of the geometrical spreading, the instrumental response, the amplitude and phase distortions due to a layered crust (Haskell, 1960, 1962), and the amplitude and phase distortions due to the anelasticity of the Earth (Futterman, 1962). All these responses were included in frequency domain. The instrumental response was calculated from the Hagiwara's (1958) formula: the parameters are T_0 = 30 sec, T_g = 100 sec, h_p = 1, h_g = 1, and σ^2 (coupling factor) = 0.1. The attenuation factor and the crustal structure are the same as those used by Fukao (1970). The S waves are synthesized from both SH and SV waves.

4.2. Interpretation

For the computation of synthetic seismograms, we use eq. 6. In the present study take-off angles of the ray paths range from 15° to 22° for both P and S waves. This small range of take-off angles and the poor azimuthal coverage of the stations are not good enough to adequately determine the rupture velocity. Then the rupture velocity is constrained at 2.3 km/sec. In these cases, the rupture term, $(v/v_c) \cos \theta$, in eq. 7 and 8 is evaluated to be less than 0.1 to 0.2. This term is very small as compared with unity, so that we may neglect them. Then, we can simply place $\langle tc \rangle = t_c^1 = t_c^2$ in eq. 6. Since the wave form at far field is not very sensitive to the rise time because of the

anelasticity of the medium, we reasonably assume $\tau = 2$ sec.
With these parameters we can compute synthetic seismograms
so as to vary $\langle t_c \rangle$ and M_o. The parameters $\langle t_c \rangle$ and M_o
affect mainly the width of the initial pulse and the ampli-
tude, respectively.

A direct comparison of the best fit synthetic
seismograms with the observed seismograms is shown in fig. 10
for S waves and in fig. 11 for P waves. In the present
study it is attempted to fit only the first half cycle. It
can be seen in terms of $\langle t_c \rangle$ and M_o the synthetic seismograms
explain reasonably the observed wave forms of at least
the first half cycle of both S and P waves. The discrepancy
after the first half cycle of the pulse arrival is probably
due to the effect of the free surface near the source.
Actually a good agreement of general features between the
observed and synthetic wave forms has been obtained at
least for deep earthquakes (e.g., Fukao, 1970; Mikumo, 1971).

By a direct comparison between the synthetic and
observed seismograms for the pulse width and the amplitude
of the first half cycle of the S and P waves, we obtain the
results for $\langle t_c \rangle$ and M_o (Table 1). The seismic moment is
determined as 2.6×10^{25} dyne-cm for S waves and 3.3×10^{25}
dyne-cm for P waves; the average value is 3.0×10^{25} dyne-cm.
According to the slip dislocation theory of the faulting
(Aki, 1966), the slip dislocation $\langle D \rangle$ averaged over the

fault area can be readily estimated from $\langle D \rangle = M_o / \mu S$, where μ is the rigidity and S is the fault area. Using the values $M_o = 3.0 \times 10^{25}$ dyne-cm, $\mu = 3.4 \times 10^{11}$ dyne/cm^2, $S = 20 \times 8$ km^2, we have $\langle D \rangle = 55$ cm.

We can also estimate the fault length from $\langle t_c \rangle$. We obtain $L = 17 \pm 8$ km. The poor accuracy of the result is partly due to the simplification of the rupture term. The point to be emphasized here is that the fault length estimated from the aftershock area is not significantly different from that estimated from the seismic waves.

5. Dislocation velocity and effective stress

We obtained $\langle D \rangle = 65$ cm from the seismic near-field data and $\langle D \rangle = 55$ cm from the teleseismic data, independently. We consider that the agreement is reasonably good. As described before, this close agreement gives us confidence in the previously obtained results, in particular, $\tau = 2$ sec and $v = 2.3$ km/sec. The amount of dislocation, 60 cm, is used in the following discussion.

The dislocation velocity (the velocity of one side of the fault with respect to the other) can be determined from the dislocation-time history during the earthquake. Since the rise time which represents the time required for the completion of the dislocation at a point on the fault has been obtained, we can determine the overall dislocation

velocity dividing the final dislocation by the rise time. with $\langle D \rangle$ = 60 cm and τ = 2 sec, the result is

$$\langle \dot{D} \rangle = \langle D \rangle / \tau = 30 \text{ cm/sec} \qquad (9)$$

Then, the overall particle velocity of the faulting (one-half the velocity of one side of the fault with respect to the other) is estimated to be 15 cm/sec.

The dislocation velocity is directly related to the effective stress which accelerates the fault motion. Kanamori (1972) has related the overall dislocation velocity with the effective stress, summarizing the presently available dynamic-dislocation models of the faulting. According to his summary, the most practical expression for a bilateral fault of finite length and a finite rupture velocity is given by

$$\sigma_{eff} = (1 + \frac{\beta}{v}) \frac{\mu}{\beta} \frac{\langle \dot{D} \rangle}{2} \qquad (10)$$

where σ_{eff} is the effective stress, β the shear velocity, v the rupture velocity, μ the rigidity and $\langle \dot{D} \rangle$ the overall dislocation velocity. Using β = 3.5 km/sec, v = 2.3 km/sec, μ = 3.4 x 10^{11} dyne/cm^2, $\langle \dot{D} \rangle$ = 30 cm/sec, we obtain the effective stress of 37 bar.

Using the slip dislocation theory of faulting (Knopoff, 1958), we can estimate the static fault parameters such as the stress drop $\Delta \sigma$, the strain drop $\Delta \varepsilon$, and

the released strain energy $\underline{W}$. The formulas used here are:

$$\Delta \sigma = \frac{4}{\pi} \frac{\mu <D>}{W} \; , \quad \Delta \varepsilon = \frac{\Delta \sigma}{\mu}$$

$$W = \frac{2}{\pi} \mu <D>^2 L \tag{11}$$

The results are: $\underline{\Delta \sigma}$ = 32 bar; $\underline{\Delta \varepsilon}$ = 0.94 x 10^{-4}; $\underline{W}$ = 1.6 x 10^{21} erg. The stress drop is about the same order as that for large shallow earthquakes which occurred beneath the trench along the Pacific coast (e.g. Abe, 1972). The stress drop refers to the difference in stress before and after the formation of the fault, but not to the prevailing tectonic stress. However, it is to be noted that the stress drop is about the same as the effective stress. This approximate equality suggests that most of the effective stress which had been acting on the fault prior to the earthquake was released at the time of the earthquake.

6. Discussion and conclusion

Some major earthquakes occurred in the neighboring regions of the Wakasa-Bay earthquake (M = 6.9) of 1963. Major destructive shocks are the Tottori earthquake (M = 7.4) of 1943 and the Fukui earthquake (M = 7.3) of 1948. Kanamori (1972, 1973) obtained, from the analysis of close-in seismograms, the overall dislocation velocity of 83 cm/sec for the Tottori earthquake and 100 cm/sec for the

Fukui earthquake. The two earthquakes represent a predominant strike-slip faulting. We note that these estimates are about three times as large as the dislocation velocity of the Wakasa-Bay earthquake. In other words, it is such a difference of the overall dislocation velocity that suggests a significant difference in the stress level in the respective epicentral areas.

We further note that the earthquakes cited above represent almost the complete release of the effective stress at the time of the earthquake. This feature is what might be expected of a purely elastic rebound in which the stored stress is released instantaneously following a brittle fracture. In such a case, the stress drop is indicative of the effective tectonic stress and then the dislocation velocity can be eventually interpreted in terms of the stress drop. By replacing eq. 10 by

$$\langle \dot{D} \rangle \approx \frac{2\beta}{\mu} (1 + \frac{\beta}{\upsilon})^{-1} \Delta\sigma \qquad (12)$$

we can estimate the overall dislocation velocity. In the limit of $\upsilon = \beta$, as a rough approximation, eq. 12 gives

$$\langle \dot{D} \rangle \approx (\frac{\beta}{\mu}) \Delta\sigma \qquad (13)$$

This relation may be useful for predicting the overall dislocation velocity expected for a future large earthquake, for example, if stress drops are determined for small

earthquakes occurring at the expected localities.

On the basis of the seismic near-field seismograms, the far-field seismograms and the aftershocks, the source process of the Wakasa-Bay earthquake of March 26, 1963, are studied. Synthetic seismograms were computed for various fault models and were compared with the observed seismograms to obtain appropriate fault parameters. The results can be summarized as follows.

Hypocenter: origin time 21^h 34^m 38.5^s, latitude
35.80°N, longitude 135.76°E, depth 4 km,

Fault geometry: dip direction N 144°E, dip angle 68°,
slip angle 22°,

Fault motion: right-lateral strike-slip motion
with some reverse dip-slip component,

Fault dimension: length 20 km, down-dip width 8 km,

Rupture velocity: 2.3 km/sec (bilateral),

Seismic moment: 3.3×10^{25} dyne-cm,

Average dislocation: 60 cm,

Stress drop: 32 bar,

Strain drop: 0.94×10^{-4},

Rise time: 2 sec,

Overall dislocation velocity: 30 cm/sec,

Effective stress: 40 bar.

It is concluded that the earthquake represents a nearly complete release of the effective stress. For such a case,

the overall dislocation velocity is approximately given by the relation, $\langle \dot{D} \rangle \approx (\beta / \mu) \Delta \sigma$, where β is the shear wave velocity, μ the rigidity, and $\Delta \sigma$ the stress drop.

Acknowledgment

References

Abe, K. (1972). Mechanisms and tectonic implications of the 1966 and 1970 Peru earthquakes, Phys. Earth Planet. Interiors 5, 367-379.

Aki, K. (1966). Generation and propagation of G waves from the Niigata earthquake of June 16, 1964, Bull. Earthquake Res. Inst., Tokyo Univ. 44, 73-88.

Brune, J.N. (1970). Tectonic stress and the spectra of seismic shear waves from earthquakes, J. Geophys. Res. 75, 4997-5009.

DeHoop, A.T. (1958). Representation theorems for the displacement in an elastic solid and their application to elastodynamic diffraction theory, Thesis, Technische Hogeschool, Delft.

Fukao, Y. (1970). Focal process of a deep focus earthquake as deduced from long period P and S waves, Bull. Earthquake Res. Inst., Tokyo Univ. 48, 707-727.

Futterman, W.I. (1962). Dispersive body waves, J. Geophys. Res. 67, 5279-5291.

Hagiwara, T. (1958) A note on the theory of the electromagnetic seismograph, Bull. Earthquake Res. Inst., Tokyo Univ. 36, 139-164.

Haskell, N.A. (1960). Crustal reflection of plane SH waves,
J. Geophys. Res. 65, 4147-4150.

Haskell, N.A. (1962). Crustal reflection of plane P and SV
waves, J. Geophys. Res. 67, 4751-4767.

Haskell, N.A. (1964). Total energy and energy spectral density
of elastic wave radiation from propagating faults,
Bull. Seism. Soc. Am. 54, 1811-1841.

Haskell, N.A. (1969). Elastic displacements in the near-field
of a propagating fault, Bull. Seism. Soc. Am. 59, 865-908.

Hirasawa, T. (1966). A least squares method for the focal
mechanism determination from S wave data, Bull. Earthquake
Res. Inst., Tokyo Univ. 44, 901-918.

Ichikawa, M. (1971). Reanalyses of mechanism of earthquakes
which occurred in and near Japan, and statistical studies
on the nodal plane solutions obtained, 1926-1968, Geophys.
Mag. 35, 207-274.

Kanamori, H. (1972). Determination of effective tectonic stress
associated with earthquake faulting: The Tottori earth-
quake of 1943, Phys. Earth Planet. Interiors 5, 426-434.

Kanamori, H. (1973). Mode of strain release associated with
major earthquakes in Japan, Ann. Rev. Earth Planet. Sci. 1,
213-239.

Knopoff, L. (1958). Energy release in earthquakes, Geophys. J. 1, 44-52.

Mikumo, T. (1971). Source process of deep and intermediate earthquakes as inferred from long-period P and S waveforms, 2. Deep-focus and intermediate-depth earthquakes around Japan, J. Phys. Earth, Tokyo 19, 303-320.

Stauder, W. and G.A. Bollinger (1965). The S Wave Project for Focal Mechanism Studies, Earthquakes of 1963, Inst. Tech. Saint Louis Univ. 91 pp.

Figure Captions

Fig. 1 The root-mean-square (RMS) of the observed minus computed P times (O-C residuals) versus focal depth. The total number of stations in the NE, SE, SW and NW quadrants is shown in the inset.

Fig. 2 O-C residuals at nearby stations for 5 focal depths. Approximate distribution of 7 stations ($\Delta \leq 1°$) is shown on the bottom.

Fig. 3 Distribution of the aftershocks within 24 hours after the main shock.

Fig. 4 The P-wave first motion and the S-wave polarization angle obtained for the Wakasa-Bay earthquake of March 26, 1963. The lower half of the focal sphere is projected on the Wulff grid. ϕ is the dip direction measured clockwise from the north and δ is the dip angle. The solid curves show the nodal plane solution determined by the S wave data.

Fig. 5 The fault geometry of the Wakasa-Bay earthquake of 1963. The locations of the Maizuru and Abuyama seismological observatories are shown.

Fig. 6 Seismograms of the Wakasa-Bay earthquake of 1963 recorded at Maizuru and Abuyama. T_0 is the free period of pendulum, ε the damping ratio and V the static magnification.

Fig. 7 Observed seismograms and synthetic seismograms

calculated for various values of rise time τ and rupture velocity v. The dislocation $\langle D \rangle$ is held constant.

Fig. 8   Radiation patterns of P, SH and SV waves for the take-off angle of $20°$. The azimuthal distribution of the stations used is shown.

Fig. 9   General form of the source time function $f(t; \tau, t_c)$ in the Haskell model. The cases for $\tau < t_c$ and $\tau > t_c$ are shown. Both areas are equal to t_c.

Fig. 10   Comparison of the observed far-field seismograms of S waves with the best fit synthetic seismograms. Amplitude is normalized.

Fig. 11   Comparison of the observed far-field seismograms of P waves with the best fit synthetic seismograms. Amplitude is normalized.

Table 1. Station data, pulse width and seismic moment

Station	Δ (°)	φ (°)	i_p (°)	S waves		P waves	
				$\langle t_s \rangle$ (sec)	M_o (10^{25} dyne-cm)	$\langle t_p \rangle$ (sec)	M_o (10^{25} dyne-cm)
ALQ	88.82	46.64	15	-	-	3	2.1
ATU	83.36	312.48	16	7	1.4	3	4.2
CCG	66.82	4.05	20	-	-	3	3.0
COP	76.89	330.93	18	4	2.9	3	4.0
COR	72.72	47.29	19	7	4.1	-	-
GDH	75.04	3.42	18	-	-	4	3.7
GOL	86.12	42.63	15	-	-	4	3.0
GSC	82.20	51.97	16	7	2.5	-	-
IST	78.27	312.29	17	-	-	2	3.0
KON	75.04	334.87	18	-	-	2	4.0
MNN	88.26	32.42	15	-	-	3	2.4
NUR	68.83	330.33	19	4	2.1	2	3.5
STU	83.33	327.65	16	5	2.4	3	3.3
UME	68.51	334.51	20	5	3.1	2	3.3

Δ, distance; ϕ, azimuth; i_p, take-off angle of P wave; M_o, seismic moment; $\langle t_s \rangle$ and $\langle t_p \rangle$, pulse width of S and P waves, respectively.
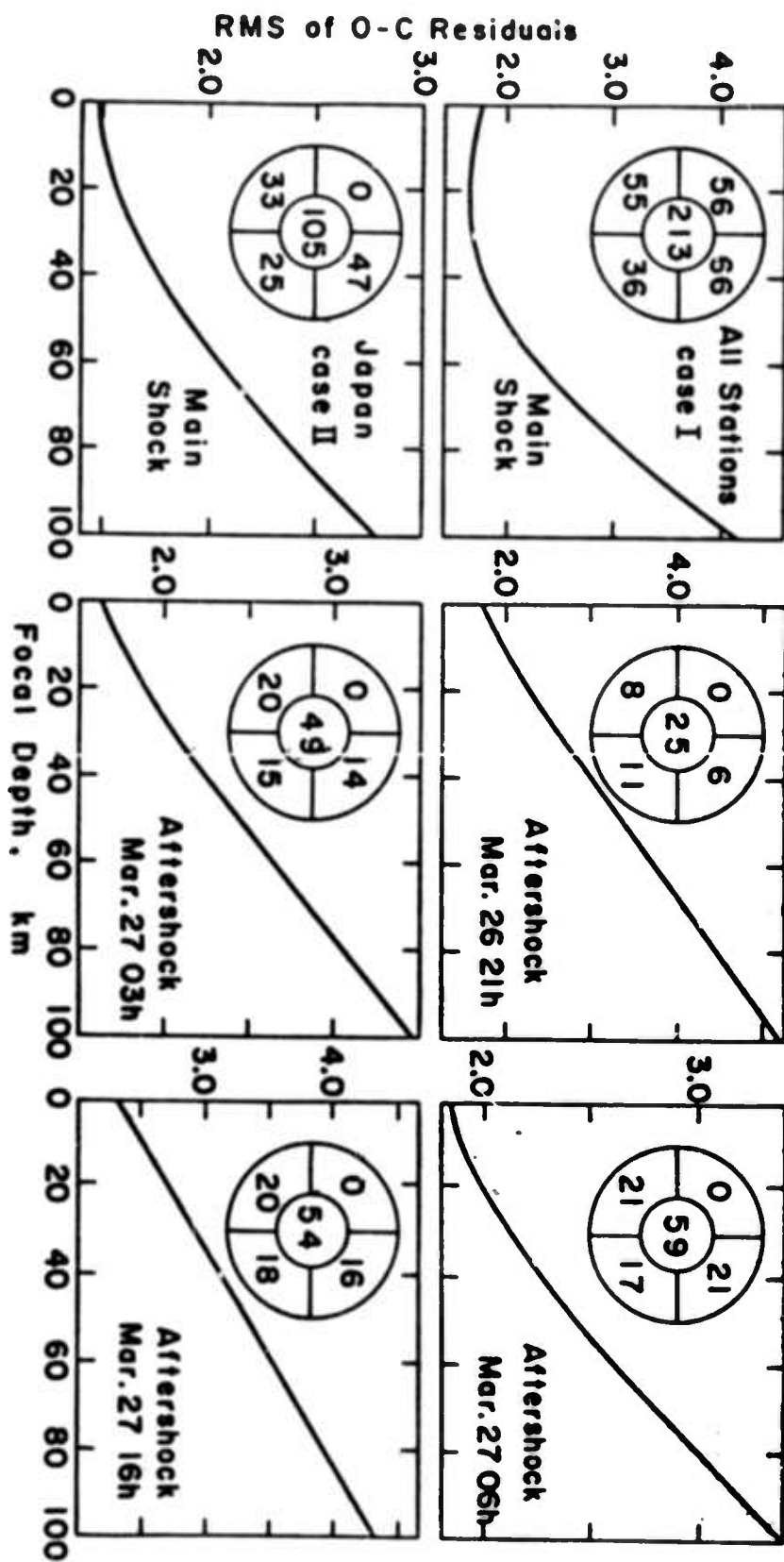
Fig. 1

Fig. 2
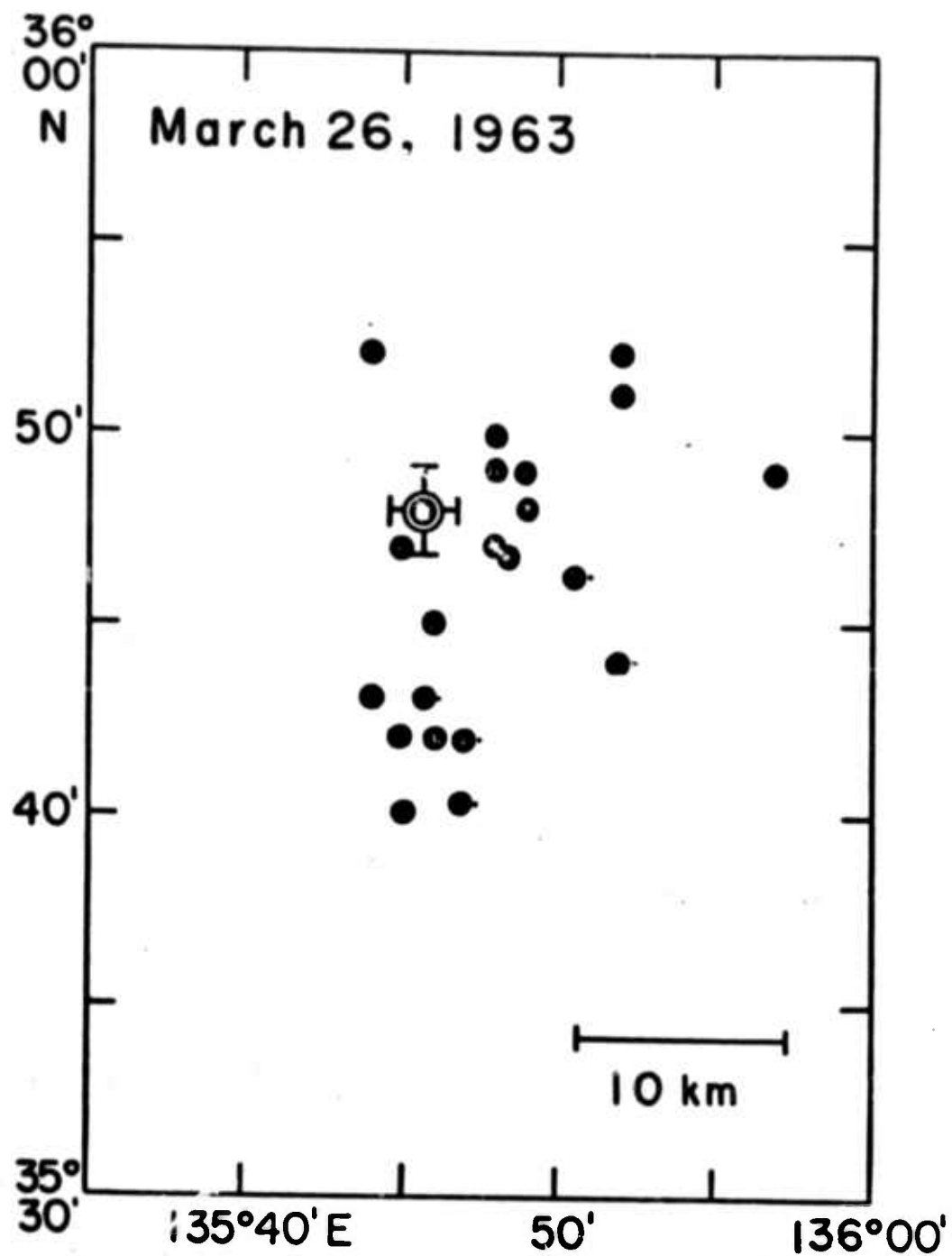
Fig. 3
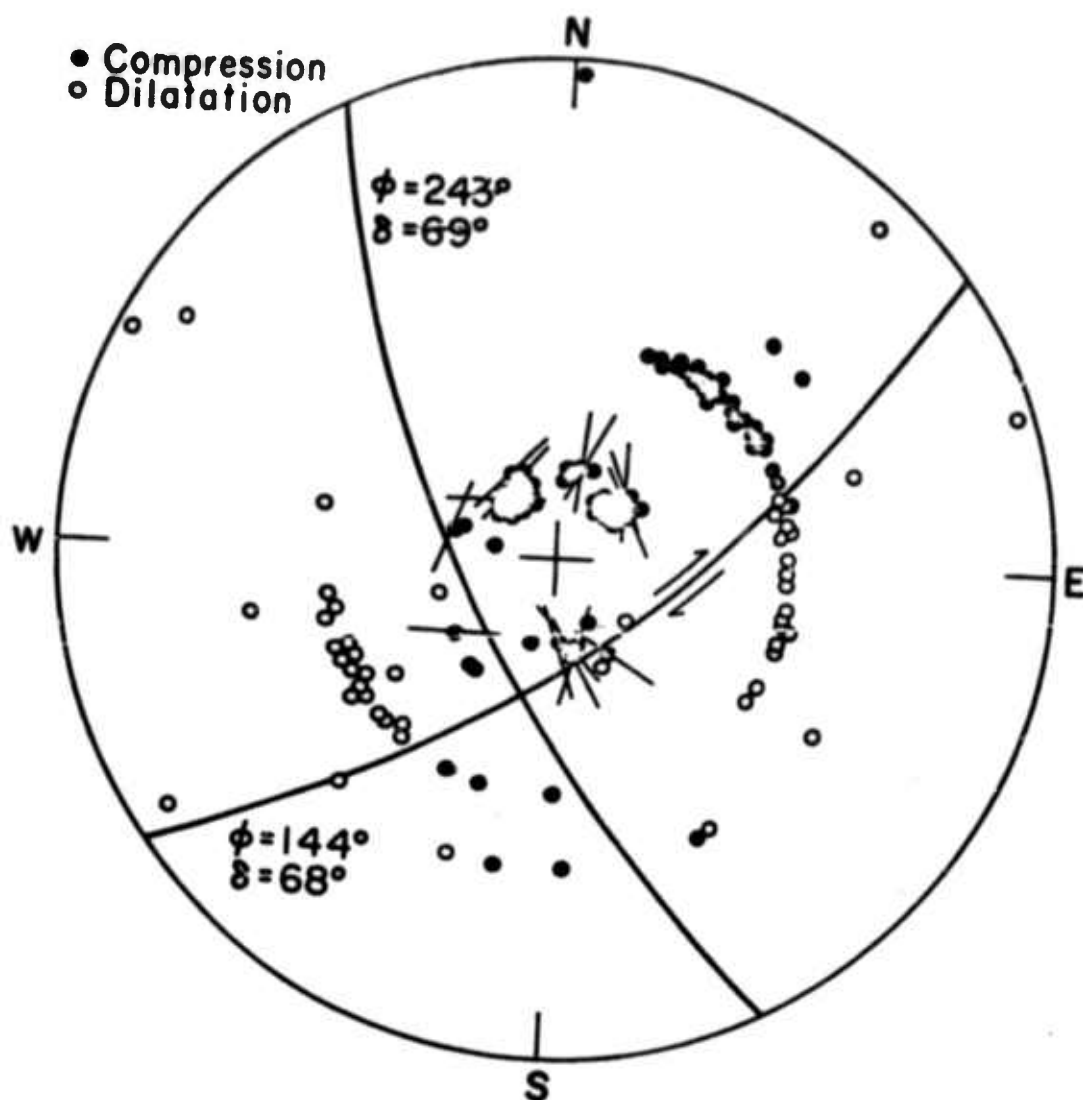
Fig. 4
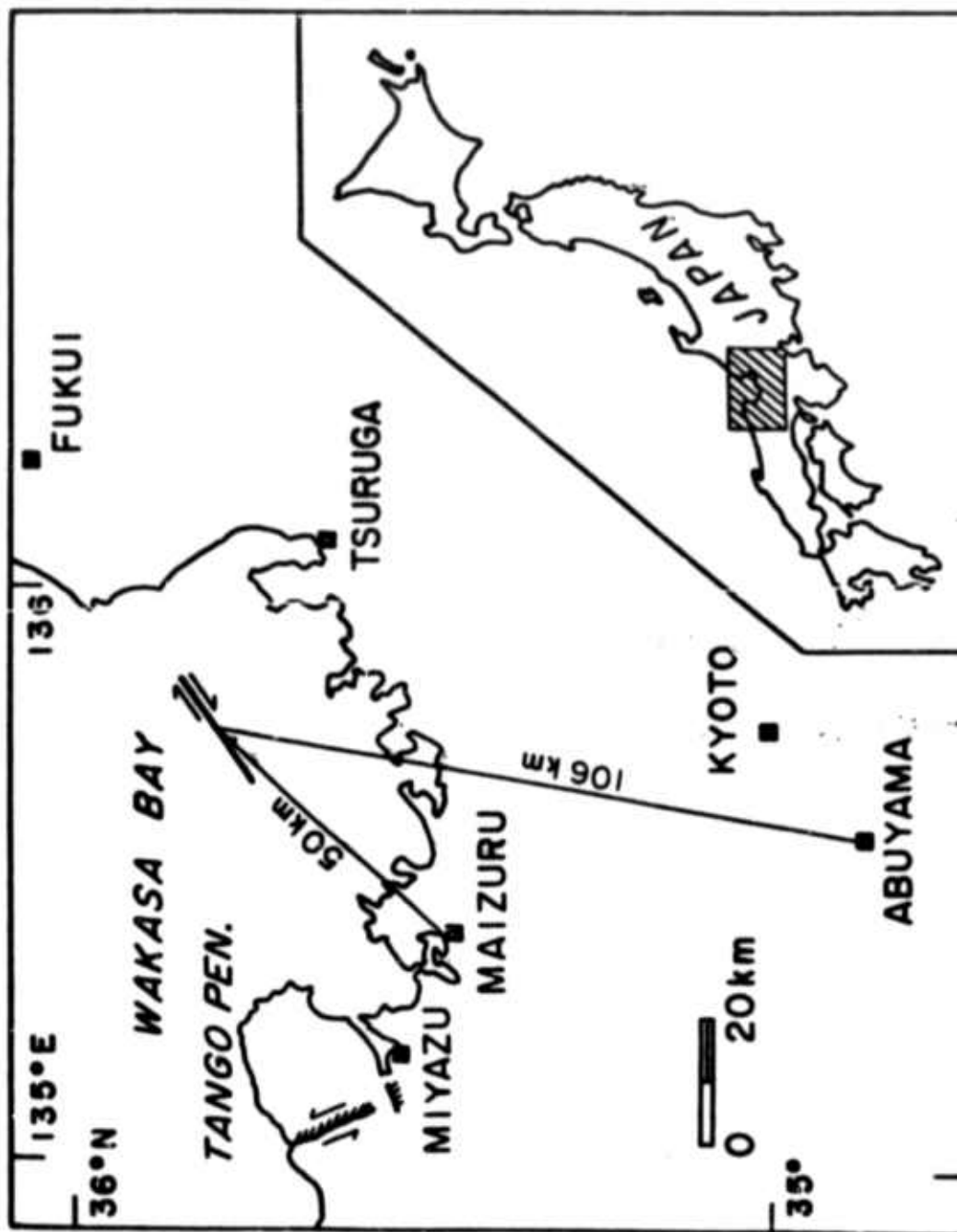
Fig. 5
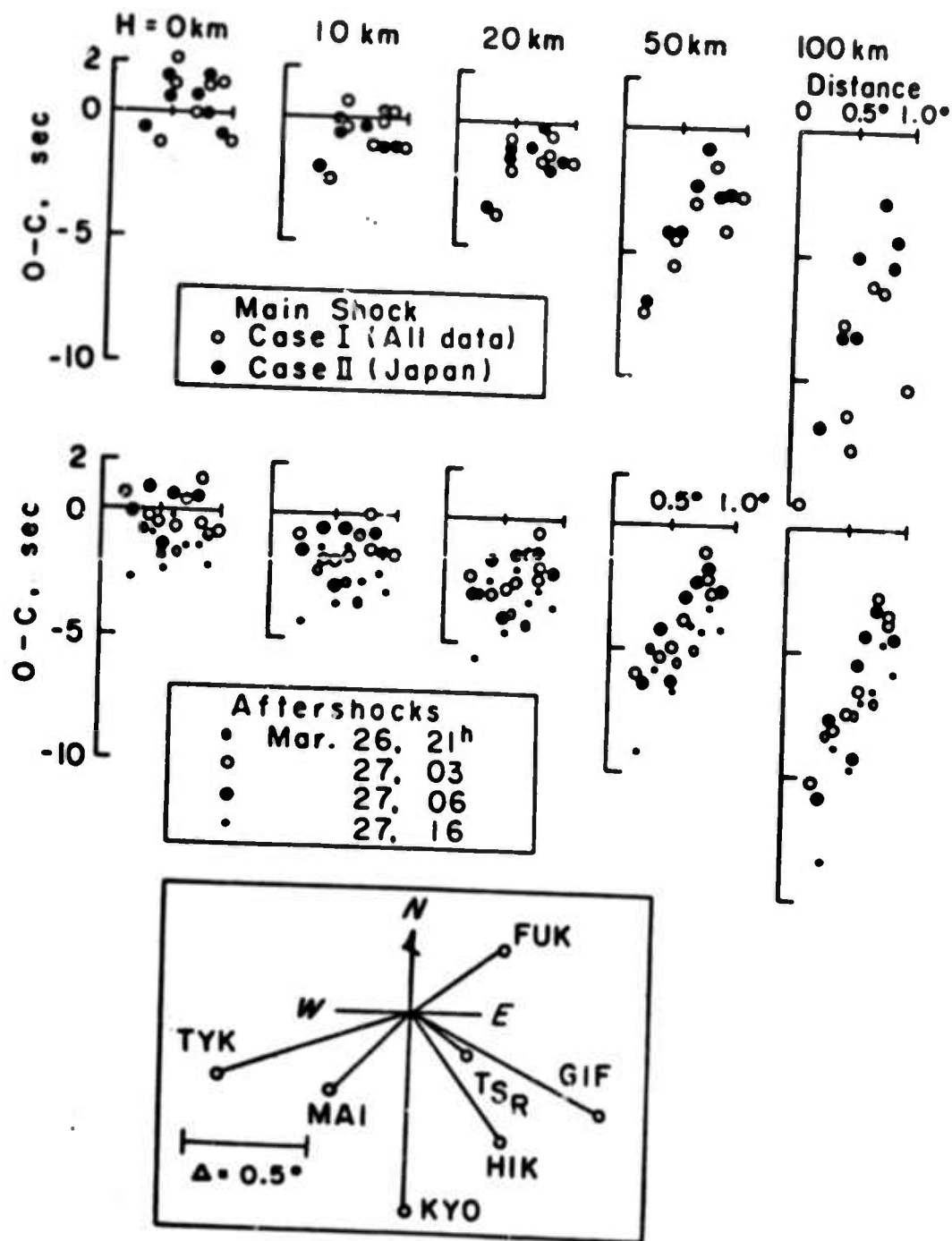
MAIZURU   Δ = 50 km
(To = 6 sec, ε = 8, v = 1)

1 cm

N
S

1 min

March 26, 1963

ABUYAMA   Δ = 106 km
(To = 28, ε = 2.3, v = 1.1)

1 cm

S
N

March 26, 1963

1 min

NS   March 26~27   1963

Fig. 6
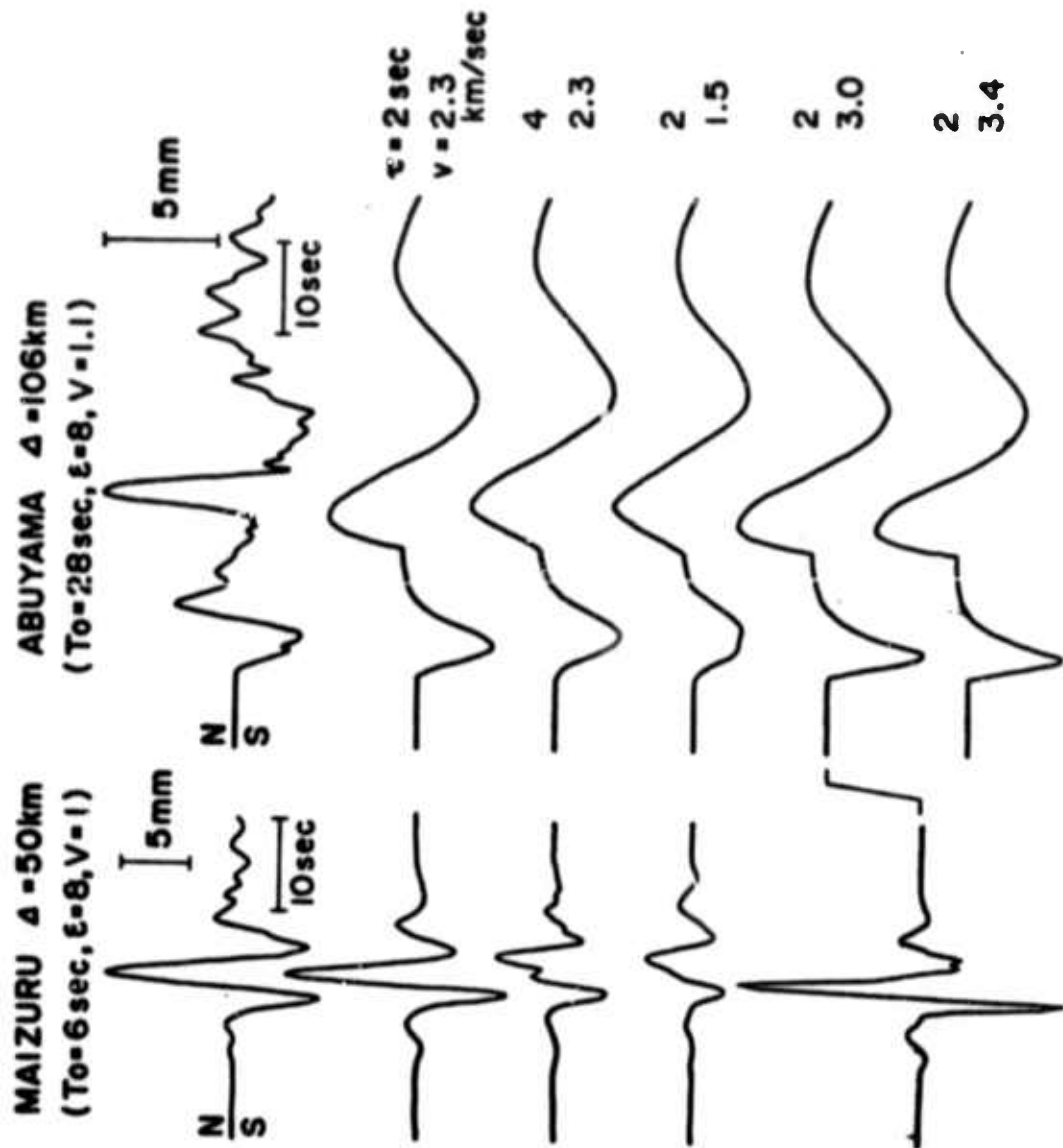
Fig. 7
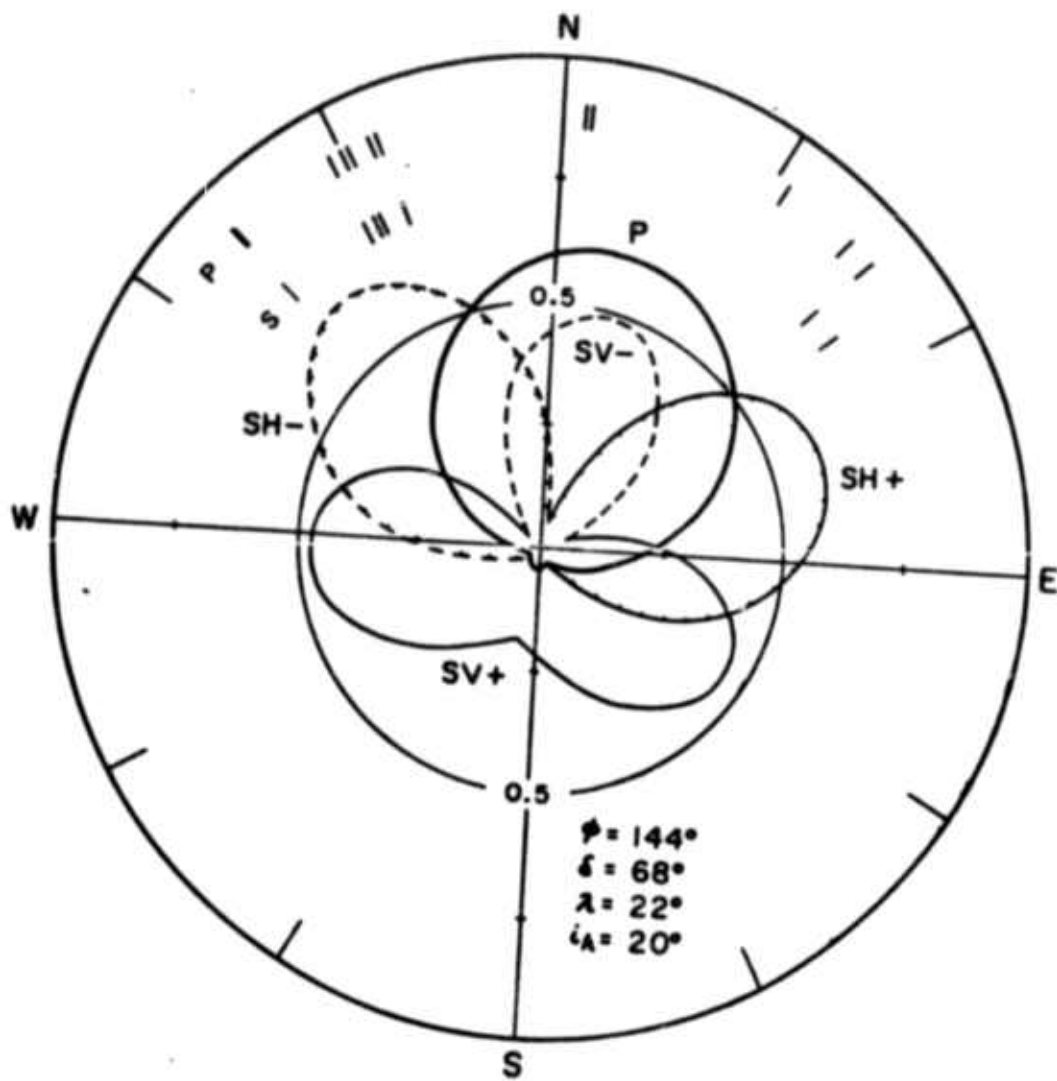
Fig. 8
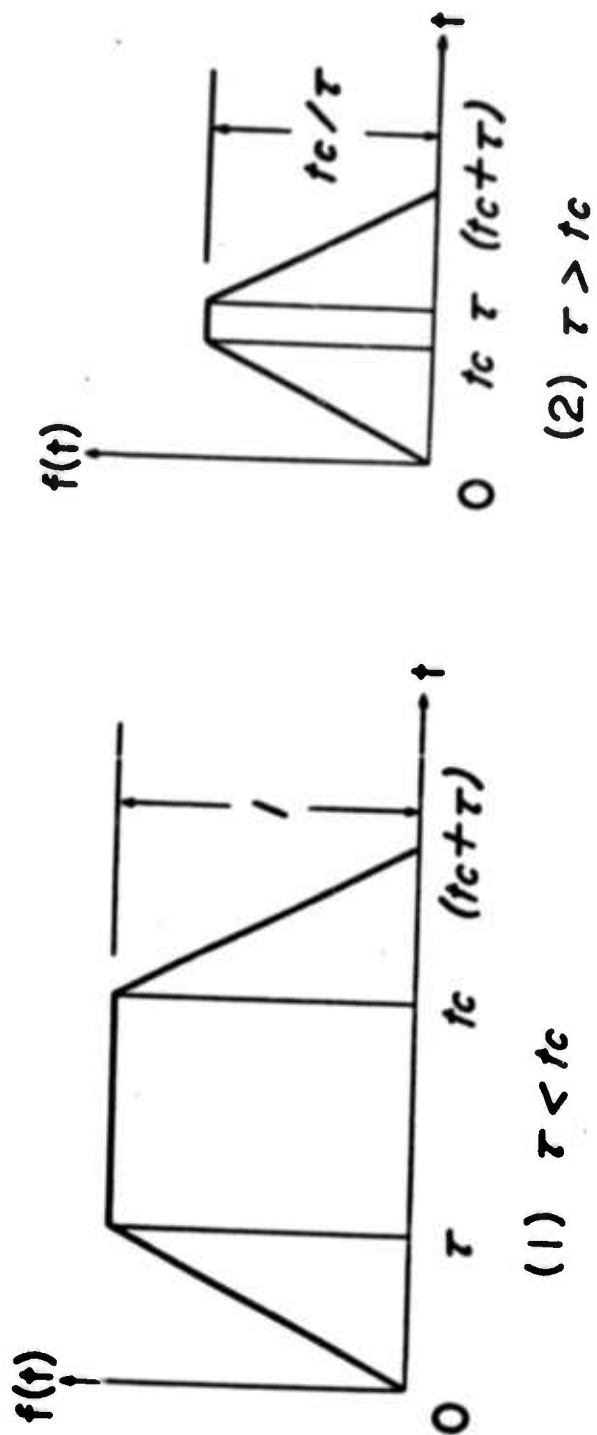
Fig. 9
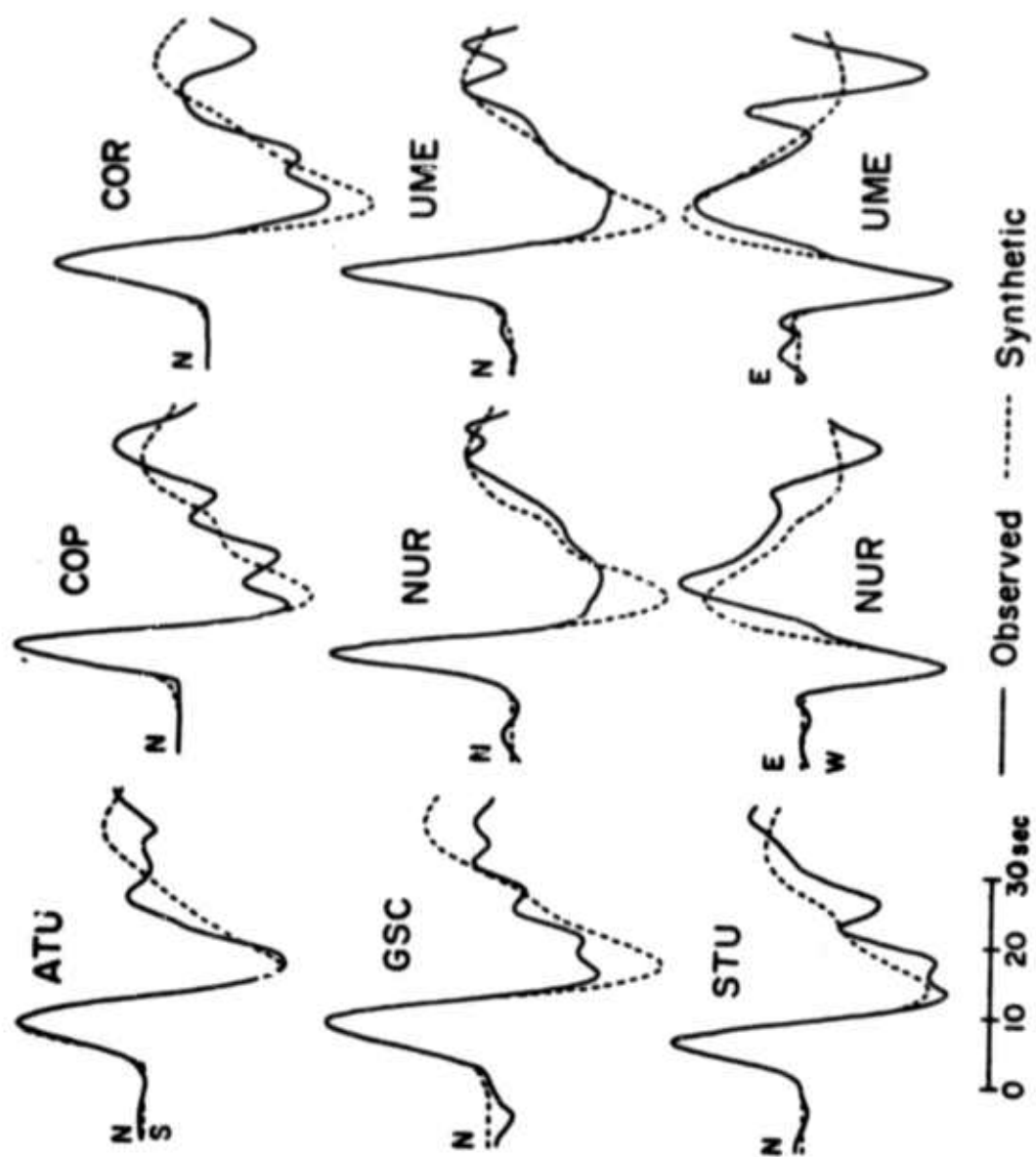
Fig. 10
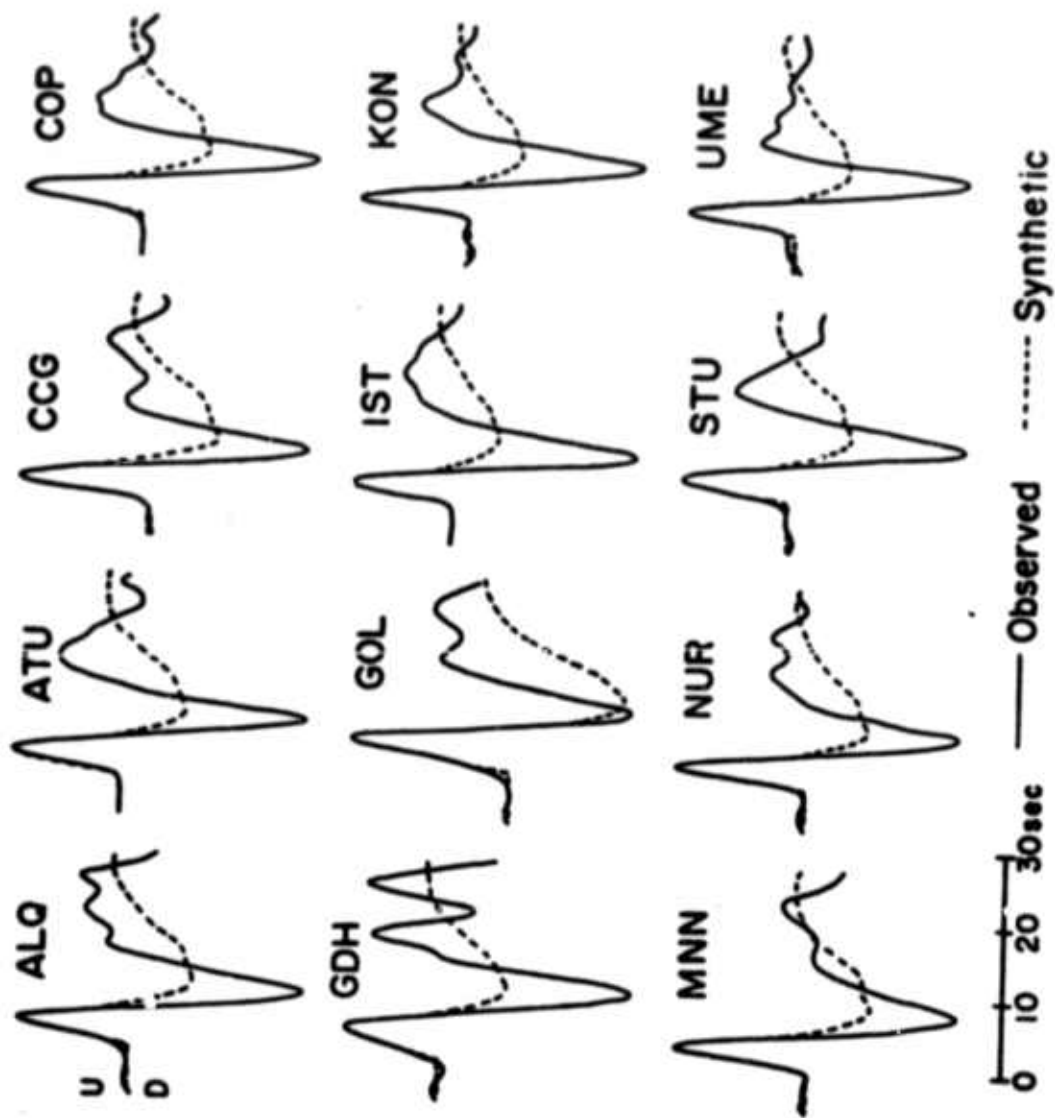
Fig. 11

3. SEISMIC WAVE PROPAGATION

3.1 <u>Elastic Wave Propagation in Homogeneous Transversely Isotropic Medium With Symmetry Axis Parallel to the Free Surface</u> by Chi-fung Wang (abstract)

Phase velocities of elastic wave propagation in a homogeneous transversely isotropic medium with symmetry axis parallel to the free surface of a half space is investigated. Approximate solutions of the problem of phase velocities of Rayleigh, horizontally propagating P and SH waves is obtained by means of perturbation method on the assumption that the deviation of the elastic coefficients from isotropy is small. In the case of horizontally propagating SV waves an exact solution is obtained. The vertical lamination model approximating fracture zones and the Olivine model showing large azimuthal variation of P and Rayleigh waves needed some modification in such a way that the a axis of Olivine crystal will be distributed diffusely. Suitable choice of weighting functions averaging the orientation of an a axis will give close agreement between both observed and predicted P and Rayleigh waves.

3.2 <u>A Precise, Continuous Measurement of Seismic Velocity</u>
<u>for Monitoring In Situ Stress</u> by Paul Reasenberg and
Keiiti Aki (abstract)

An air gun repeatedly shot in a water-filled hole every
6 or 10 s was used to measure the in situ seismic velocity
over a distance of 200 m in a granite quarry. We found a
peak-to-peak half-percent variation of velocity, which
correlates well with the variation in tidal stress. The
inferred high stress sensitivity of velocity change (0.2
bar^{-1}) may be attributed to the presence of extremely thin
cracks (aspect ratio 10^{-5}) by which the rock mass near the
surface is broken into blocks. Such cracks should close at
a depth of about 15 m. When the present results for de-
tecting the tidal effect on velocity are extrapolated for
waves penetrating to depths of a few kilometers, the velo-
city must be measured with a precision of better than one
part in 10^5.

3.3 <u>Velocity and Attenuation of Seismic Waves in Two-Phase</u>
<u>Media: I. Theoretical Formulations</u> by Guy T. Kuster
and M. Nafi Toksöz

Summary

The propagation of seismic waves in two-phase media
is treated theoretically to determine the elastic moduli
of the composite medium given the properties, concentration

and shapes of the inclusions and the matrix material. Assuming long wavelengths the problem is formulated in terms of scattering phenomena similar to the approach of Ament (1959). The displacement fields, expanded in series, for waves scattered by an "effective" composite medium and individual inclusions are equated. The coefficients of series expansions of the displacement fields provide a relationship between the elastic moduli of the effective medium and those of the matrix and inclusions. The expressions are derived both for solid and liquid inclusions in solid matrix, as well as for solid suspensions in fluid matrix. Both spherical and oblate spheroidal inclusions are considered.

Some numerical calculations are carried out to demonstrate the effects of fluid inclusions and inclusion shapes on the seismic velocities in rocks. It is found that in addition to concentration, inclusion shapes and properties are important parameters. A concentration of a fraction of one percent of thin (small aspect ratio) inclusions could effect the compressional and shear velocities by more than ten percent. For both sedimentary and igneous rock models, the calculations for "dry" (i.e. air-saturated) and water-saturated states indicate that the compressional velocities change significantly while the shear velocities change much less upon saturation with water.

LIST OF SYMBOLS

A	amplitude of incident plane P wave
A_{ijpq}	fourth order tensor
a	radius of spherical inclusion
B_n	coefficient in the series expansion of scattered P waves
c	volume concentration of inclusions
c_{ijpq}	elastic tensor, matrix
c'_{ijpq}	elastic tensor, inclusion
e_{ij}	strain field
e^0_{ij}	incident strain field
G_{ki}	Green's function, matrix
$h_n^{(1)}$	spherical Hankel function, first kind
j_n	spherical Bessel function
K	matrix bulk modulus
K'	inclusion bulk modulus
K^*	effective bulk modulus
ℓ_{ij}	direction cosine
N	number of inclusions in representative sphere
p	wave number, P wave in matrix
p'	wave number, P wave in inclusion
$P_n(\cos\theta)$	Legendre polynomial, order n
R	radius, representative sphere

s wave number, S wave in matrix

s' wave number, S wave in inclusion

T_{ijpq} 4th order tensor depending on matrix and inclusion properties

U_{ijpq} fourth order tensor

$\underline{u}$ total displacement vector

$\underline{u}^0$ incident displacement vector

$\underline{u}^s$ scattered displacement vector for s^{th} inclusion

$\underline{u}^*$ scattered displacement vector from representative sphere

$\underline{\Delta u}$ scattered displacement vector

u radial displacement

u^j radial displacement scattered from j^{th} inclusion

u^* radial displacement scattered from representative sphere

V volume of an inclusion

V_0 volume of representative sphere

V_j volume of jth inclusion in representative sphere

$\underline{v}$ displacement vector inside an inclusion

v transverse displacement

v^j transverse displacement scattered from j^{th} inclusion

v^* transverse displacement scattered from representative sphere

$\underline{x}$ point in the matrix

$\underline{x}_0$ center of representative sphere

$\underline{x}_s$ center of sth inclusion

α aspect ratio of oblate spheroid

α^* effective P wave velocity

α_s^* effective "static" P wave velocity

β^* effective S wave velocity

λ matrix Lamé's constant

λ' inclusion Lamé's constant

μ matrix shear modulus

μ' inclusion shear modulus

μ^* effective shear modulus

ρ matrix density

ρ' inclusion density

ρ^* effective density

ρ_g^* effective gravitational density

$\underline{\xi}$ point inside an inclusion

$\underline{\zeta}$ center of an inclusion

$\underline{\zeta}^0$ center of representative sphere

η viscosity

ω angular frequency

INTRODUCTION

In the earth, where rocks are generally saturated or partly saturated with fluids the seismic waves propagate through two-phase media. For theoretical treatment, a two-phase medium is defined as an aggregate of two homogeneous phases of different properties, where one phase (the matrix) is a continuum in which inclusions of the other phase are randomly embedded. If the two-phase medium is quasi-homogeneous, one could define an homogeneous medium (the effective medium) which is equivalent to the two-phase medium on a macroscopic scale. In this paper we will derive theoretical expressions for the effective properties of a two-phase medium for the propagation of elastic waves whose wavelengths are much longer than the size of an inclusion.

Theoretical treatment of the propagation of elastic waves in two-phase media (the dynamic problem) is relatively scarce. In a few studies on this subject (Ament, 1959; Mal and Knopoff, 1967), the results were restricted to the case where the matrix is solid, the inclusions are spherical and much smaller than the wavelengths and sufficiently far apart from each other so that interactions are negligible. Ament (1953) studied the case of rigid spheres in a viscous liquid matrix. Biot (1956a,b) treated the problem for porous rocks

for both high and low frequency limits. His elegant formulations require the specification of a number of parameters before the effective medium properties can be computed. Chekin (1970) worked on the problem of wave propagation in rocks with cracks, but his formulations were for zero-width cracks.

The theoretical elastic behavior of two-phase media under static loading has been studied in detail (see Hashin, 1970, for a review). The results of these studies have been applied to seismic problems under the assumption that the conditions prevailing in the propagation of long wavelength waves can be approximated by those under static loading (Eshelby, 1957; Hashin, 1962; Hashin and Shtrikman, 1963; Wu, 1966; Walsh, 1969; Solomon, 1972; Dederichs and Zeller, 1973; Korringa, 1973; Zeller and Dederichs, 1973). The static approaches, although not exact formulations for the dynamic problem have lead to most useful results. As our comparisons will show later, scattering phenomena and inertia effects, intrinsic features of the wave propagation generally omitted in static models, become of importance only in limited cases.

In this paper we follow the approach of Ament (1959) and formulate the problem in terms of scattering phenomena. We repeat his derivation for spherical inclusions embedded in a solid matrix and we treat the additional cases of a fluid matrix and of spheroidal inclusions. All our models involve the assumptions that the wavelengths are much longer

than the size of the inclusions and that multiple scattering effects are negligible.

THEORETICAL FORMULATION IN TERMS OF SCATTERING

Consider N inclusions randomly embedded within a finite region V_0 of an infinite matrix (Figure 1). Let an elastic wave be incident from infinity. We may write the displacement

$\underline{u}(\underline{x})$ observed at a point $\underline{x}$ outside V_0 as

$$\underline{u}(\underline{x}) = u^0(\underline{x}) + \sum_{s=1}^{N} \underline{u}^s(\underline{x}, \underline{x}_s) \tag{1}$$

where $\underline{u}^s(\underline{x}, \underline{x}_s)$ is the displacement observed at $\underline{x}$ due to the wave scattered by the sth inclusion located at $\underline{x}_s$ and where $\underline{u}^0(\underline{x})$ is the displacement due to the incident wave.

When examined on the scale of V_0, Figure 1 also represents a piece of a two-phase medium isolated in an infinite matrix. Assuming that the two-phase medium is homogeneous on the scale of V_0 we can define the properties of the effective medium to be the same as those of an homogeneous medium which, when confined to the volume V_0 and illuminated by the same incident wave $\underline{u}^0$ produces the same displacement field at the point $\underline{x}$ as the field generated by the N inclusions. We may write

$$\underline{u}(\underline{x}) = \underline{u}^0(\underline{x}) + u^*(\underline{x}, \underline{x}_0) \tag{2}$$

where $\underline{u}^*(\underline{x}, \underline{x}_0)$ is the scattered displacement field observed at $\underline{x}$ due to the volume V_0 having effective properties and located at x_0.

Equating (1) and (2) we obtain the fundamental equation defining the effective medium

$$u^*(\underline{x}, \underline{x}_0) = \sum_{s=1}^{N} \underline{u}^s(\underline{x}, \underline{x}_s) \tag{3}$$

If we assume that the two-phase medium is isotropic, the

effective medium will also be isotropic and we must take a sphere for the volume V_0 so that the scattered waves do not depend on the orientation of V_0 with respect to the incident field. Thus from here on we shall call the volume V_0 the representative sphere.

In order to solve (3) for the effective properties exactly, a complete statistical description of the distribution of the inclusions is required. The wave scattered by each inclusion is a function of the wave incident on this particular inclusion and this incident wave depends on the location of the other inclusions because of multiple scattering effects. The relative location of all inclusions must also be known for the calculation of the sum of all scattered waves. In real two-phase media such statistical information is not available. Usually only the relative volume fractions of the phases are known. In order to solve (3) with the limited information we have, we make two additional assumptions: (i) we assume that the observation point $\underline{x}$ is sufficiently far from the representative sphere so that we may take as a first approximation

$$\underline{x}_s \approx \underline{x}_0 \quad , \qquad s = 1, N$$

and (ii) we assume that multiple scattering effects are negligible, which allows us to take the undisturbed incident

field as the field incident on each inclusion within the representative sphere. The latter assumption restricts the validity of our results to small volume concentrations of inclusions, or in other words to the case of non-interacting inclusions. The possibility of taking interactions into account by the use of self-consistent schemes is discussed elsewhere (Kuster, 1972).

With these approximations, the problem of finding the effective properties of a two-phase medium reduces to the estimation of the scattered displacement field due to an inclusion isolated in an infinite matrix, given a mono-chromatic incident wave of long wavelength.

Even this simplified problem is amenable to mathematical treatment only when the inclusion is of a regular shape, such as a sphere or a spheroid.

Scattering by spherical inclusions

Consider an homogeneous and isotropic sphere with elastic constants λ' and μ' and density ρ' embedded in an homogeneous and isotropic infinite matrix with elastic constants λ and μ and density ρ. Let a plane P wave be incident along the x axis with displacement

$$u_x = \frac{A}{ip} e^{i(px-\omega t)} \tag{4}$$

where A is the amplitude, p the wavenumber and ω the angular frequency. The presence of the sphere generates four additional waves: the P and S waves inside the sphere and the P and S waves scattered into the matrix. We formulate the problem in spherical coordinates with the origin at the center of the sphere (Figure 1). Because of the symmetries of the problem we need not consider the azimuthal dependence. Following Yamakawa (1962) we express the radial and transverse displacements u and v corresponding to each wave in infinite series of spherical Bessel functions and Legendre polynomials. Thus the incident P wave components are:

$$u_0 = -\frac{A}{p^2} \sum_{n=0}^{\infty} (2n + 1) i^n \frac{d}{dr} j_n(pr) P_n(\cos\theta)$$

$$v_0 = -\frac{A}{p^2} \sum_{n=1}^{\infty} (2n + 1) i^n \frac{j_n(pr)}{r} \frac{d}{d\theta} P_n(\cos\theta)$$

$$(5)$$

The scattered P waves are

$$u_1 = -\frac{1}{p^2} \sum_{n=0}^{\infty} B_n \frac{d}{dr} h_n^{(1)}(pr) P_n(\cos\theta)$$

$$v_1 = -\frac{1}{p^2} \sum_{n=1}^{\infty} B_n \frac{h_n^{(1)}(pr)}{r} \frac{d}{d\theta} P_n(\cos\theta)$$

$$(6)$$

The scattered S waves are

$$u_2 = -\frac{1}{e^2} \sum_{n=1}^{\infty} C_n \, n(n+1) \, \frac{h_n^{(1)}(sr)}{r} \, P_n(\cos\theta)$$

$$v_2 = -\frac{1}{s^2} \sum_{n=1}^{\infty} \frac{C_n}{r} \frac{d}{dr} [rh_n^{(1)}(sr)] \frac{d}{d\theta} P_n(\cos\theta)$$

(7)

The P waves in the sphere are

$$u_3 = -\frac{1}{p'^2} \sum_{n=0}^{\infty} D_n \frac{d}{dr} j_n(p'r) P_n(\cos\theta)$$

$$v_3 = -\frac{1}{p'^2} \sum_{n=1}^{\infty} D_n \frac{j_n(p'r)}{r} \frac{d}{d\theta} P_n(\cos\theta)$$

(8)

The S waves in the sphere are

$$u_4 = -\frac{1}{s'^2} \sum_{n=1}^{\infty} E_n \, n(n+1) \, \frac{j_n(s'r)}{r} \, P_n(\cos\theta)$$

$$v_4 = -\frac{1}{s'^2} \sum_{n=1}^{\infty} \frac{E_n}{r} \frac{d}{dr} [rj_n(s'r)] \frac{d}{d\theta} P_n(\cos\theta)$$

(9)

The $e^{-i\omega t}$ time dependence is omitted throughout for brevity and p and s (p' and s') denote the wavenumbers of P and S waves in matrix (inclusion) material. $P_n(\cos\theta)$ is the Legendre polynomial of the nth order, $j_n(z)$ is the spherical Bessel function of the nth order and $h_n^{(1)}(z)$ is the spherical Hankel function of the first kind and the nth order. We must use $h_n^{(1)}(z)$ for waves travelling radially outward because we adopted an $e^{-i\omega t}$ time dependence. The coefficients in the

series are determined from the boundary conditions on the surface of the sphere (continuity of displacements and normal stresses at r = a). The detailed calculation of the scattered waves is given in Appendix A in the case of interest to us where the wavelengths of all waves (incident as well as scattered and transmitted) are much longer than the radius of the sphere and where the observation point is at a large distance from the sphere. With these approximations the scattered waves can be written as

$$u = -\frac{iA}{p}(pa)^3 \frac{e^{i(pr-\omega t)}}{pr}[Be_0 - Be_1 \cos\theta - \frac{Be_2}{4}(3\cos2\theta+1)]$$

$$v = -iA\frac{(sa)^3}{p}\frac{e^{i(sr-\omega t)}}{sr}[Be_1\sin\theta + \frac{3s}{4p}Be_2\sin2\theta] \tag{10}$$

where

$$Be_0 = \frac{K-K'}{3K'+4\mu}$$

$$Be_1 = \frac{\rho-\rho'}{3\rho} \tag{11}$$

$$Be_2 = \frac{20}{3}\frac{\mu(\mu'-\mu)}{6\mu'(K+2\mu)+\mu(9K+8\mu)}$$

The neglected terms are of order $(pa)^5$.

It was shown by Yamakawa (1962) that in the case of a spherical cavity the scattered waves can be obtained from (10) and (11) by letting K', μ' and ρ' vanish; and in the case of fluid-filled cavity by letting μ' vanish. However the solution for the case of a fluid matrix cannot be obtained by simply letting μ vanish. In this case, the scattered waves can be written as (see Appendix A for the detailed derivation)

$$u = -\frac{iA(pa)^3}{p}\frac{e^{i(pr-\omega t)}}{pr}[Be_0^0 - Be_1^0 \cos\theta] \tag{12}$$

where

$$Be_0^0 = \frac{K-K'}{3K'}$$

$$Be_1^0 = \frac{\rho-\rho'}{\rho+2\rho'}. \tag{13}$$

The terms neglected are of order $(pa)^5$. This result
holds whether the inclusion is solid or fluid.

The difference between the solid and fluid matrix case
resides essentially in the 2nd term (n = 1). This term
represents a single force source which expresses the change
in inertia due to the replacement of matrix material by
inclusion material. When the matrix is solid the change in
inertia arises only from the density difference between
matrix and inclusion since there is no relative motion between
the matrix and inclusion. But when the matrix is fluid
relative motion does occur (Lamb, 1932) and the inertia term
is therefore modified.

A spheroidal inclusion

We wish to find the waves scattered by a spheroidal
inclusion embedded in a solid matrix. We cannot follow the
same procedure as for a spherical inclusion since the vector
wave equation is not separable in spheroidal coordinates
(Morse and Feshbach, 1953). Rather we shall use an integral
expression derived by Mal and Knopoff (1967) for the displacement
due to the waves scattered by an inclusion of arbitrary shape
isolated in an infinite matrix. Denoting the displacement
field of the scattered waves observed at a point $\underline{x}$ in the
matrix by $\Delta\underline{u}(\underline{x})$, the displacement field of the wave at a

point $\underline{\xi}$ inside the inclusion by $\underline{v}(\underline{\xi})$, the kth component of
the Green's function due to a point force acting in the ith
direction at a point $\underline{y}$ in the infinite matrix by $G_{ki}(\underline{x},\underline{y})$
and the elastic tensor in the matrix by c_{ijpq}, we have

$$\Delta u_k(\underline{x}) = \int\limits_V \left\{ \omega^2 (\rho'-\rho) v_i(\underline{\xi}) G_{ki}(\underline{x},\underline{\xi}) \right.$$
$$\left. -(c'_{ijpq} - c_{ijpq}) \frac{\partial v_p}{\partial \xi_q} \frac{\partial G_{ki}}{\partial \xi_j}(\underline{x},\underline{\xi}) \right\} d\underline{\xi} \tag{14}$$

The summation convention is used and we omit for brevity
the assumed $e^{i\omega t}$ time dependence. The integral is taken over
the volume V of the inclusion. If the displacement and
strain inside the inclusion can be estimated in terms of the
incident field we can obtain the desired expression for the
scattered field.

The estimation of the displacement and strain inside
the inclusion is given in Appendix B under the assumption that
the matrix is solid, that the inclusion is spheroidal and that
the wavelengths are much longer than the inclusion size. For
an observation point located at a large distance from the
inclusion, the displacement field scattered by a spheroid
of arbitrary orientation can be written as

$$\Delta u_k(\underline{x},\zeta) = V \left[\omega^2 (\rho'-\rho) u_i^0(\zeta) G_{ki}(\underline{x},\zeta) \right.$$

$$- [(\lambda'-\lambda) U_{pprs}\delta_{ij}$$

$$\left. + 2(\mu'-\mu) U_{ijrs}] e_{rs}^0 \frac{\partial G_{ki}}{\partial \zeta_j} (\underline{x},\zeta) \right] \quad (15)$$

The corresponding expression for a spherical inclusion was derived by Mal and Knopoff (1967).

$$\Delta u_k(\underline{x},\zeta) = V \left[\omega^2 (\rho'-\rho) u_i^0(\zeta) G_{ki}(\underline{x},\zeta) - \right.$$

$$\left\{ [P(K'-K) - \frac{2}{3}(\mu'-\mu)Q]\delta_{ij}e_{pp}^0 \right.$$

$$\left. + 2Q(\mu'-\mu)e_{ij}^0 \right\} \frac{\partial G_{ki}}{\partial \zeta_j} (\underline{x},\zeta) \left. \vphantom{\frac{\partial G_{ki}}{\partial \zeta_j}} \right] \quad (16)$$

THE EFFECTIVE PROPERTIES OF TWO-PHASE MEDIA

In order to obtain the effective properties of two-phase media we now use equation (3) and the expressions derived above for the scattered waves.

Spherical inclusions

Consider N spherical inclusions embedded in an infinite solid matrix and confined to the representative sphere of radius R. Let a plane P wave of amplitude A be incident from infinity. At a distant observation point, with the

$$\Delta u_k(\underline{x}, \zeta) = V \left[\omega^2 (\rho' - \rho) u_i^0(\zeta) G_{ki}(\underline{x}, \zeta) \right.$$

$$- [(\lambda' - \lambda) U_{pprs} \delta_{ij} \tag{15}$$

$$\left. + 2(\mu' - \mu) U_{ijrs}] e_{rs}^0 \frac{\partial G_{ki}}{\partial \zeta_j} (\underline{x}, \zeta) \right]$$

The corresponding expression for a spherical inclusion was derived by Mal and Knopoff (1967).

$$\Delta u_k(\underline{x}, \zeta) = V \left[\omega^2 (\rho' - \rho) u_i^0(\zeta) G_{ki}(\underline{x}, \zeta) - \right.$$

$$\left\{ [P(K' - K) - \frac{2}{3}(\mu' - \mu) Q] \delta_{ij} e_{pp}^0 \right. \tag{16}$$

$$\left. + 2Q(\mu' - \mu) e_{ij}^0 \right\} \frac{\partial G_{ki}}{\partial \zeta_j} (\underline{x}, \zeta) \left. \right]$$

THE EFFECTIVE PROPERTIES OF TWO-PHASE MEDIA

In order to obtain the effective properties of two-phase media we now use equation (3) and the expressions derived above for the scattered waves.

Spherical inclusions

Consider N spherical inclusions embedded in an infinite solid matrix and confined to the representative sphere of radius R. Let a plane P wave of amplitude A be incident from infinity. At a distant observation point, with the

assumptions listed in the previous section, the waves

scattered by the representative sphere are given by an

expression of the type of equation (10)

$$u^* = -\frac{iA(pR)^3}{p}\frac{e^{i(pr-\omega t)}}{pr}[Be_0^* - Be_1^*\cos\theta - \frac{Be_2^*}{4}(3\cos 2\theta + 1)]$$

$$(17)$$

$$v^* = -\frac{iA(sR)^3}{p}\frac{e^{i(sr-\omega t)}}{sr}[Be_1^*\sin\theta + \frac{3s}{4p}Be_2^*\sin 2\theta]$$

where

$$Be_0^* = \frac{K-K^*}{3K^*+4\mu} \qquad Be_1^* = \frac{\rho-\rho^*}{3\rho} \qquad Be_2^* = \frac{20}{3}\frac{\mu(\mu^*-\mu)}{6\mu^*(K+2\mu)+\mu(9K+8\mu)}$$

Assuming that multiple scattering effects are negligible so

that the wave incident on each inclusion is the original

plane P wave we can also write the scattered waves at the

observation point as the sum of the waves scattered by each

inclusion. Thus we also have

$$\sum_{j=1}^{N} u^i = -\frac{iA}{p}\sum_{j=1}^{N}(pa_j)^3\frac{e^{i(pr-\omega t)}}{pr}[Be_0 - Be_1\cos\theta - \frac{Be_2}{4}(3\cos 2\theta + 1)]$$

$$(18)$$

$$\sum_{j=1}^{N} v^j = -\frac{iA}{p}\sum_{j=1}^{N}(sa_j)^3\frac{e^{i(sr-\omega t)}}{sr}[Be_1\sin\theta + \frac{3s}{4p}Be_2\sin 2\theta]$$

where

$$Be_0 = \frac{K-K'}{3K'+4\mu} \qquad Be_1 = \frac{\rho-\rho'}{3\rho} \qquad Be_2 = \frac{20}{3}\frac{\mu(\mu'-\mu)}{6\mu'(K+2\mu)+\mu(9K+8\mu)}$$

Because of our definition of the effective medium by equation (3), we obtain the effective properties by equating (17) and (18). Since the equality must hold independently of the angle θ the coefficients of the corresponding angular terms must be equal. Thus we obtain the composition laws for the effective elastic constants and density

$$\frac{K^*-K}{3K^*+4\mu} = c\frac{K'-K}{3K'+4\mu} \tag{19}$$

$$\rho^*-\rho = c(\rho'-\rho) \tag{20}$$

$$\frac{\mu^*-\mu}{6\mu^*(K+2\mu)+\mu(9K+8\mu)} = \frac{c(\mu'-\mu)}{6\mu'(K+2\mu)+\mu(9K+8\mu)} \tag{21}$$

where c, the volume concentration of inclusions is given by

$$c = \frac{1}{R^3} \sum_{j=1}^{N} a_j^3 \tag{22}$$

The corresponding effective P and S wave velocities are

$$\alpha^* = \left[\frac{K^*+4\mu^*/3}{\rho^*}\right]^{\frac{1}{2}} \qquad \beta^* = \left[\frac{\mu^*}{\rho^*}\right]^{\frac{1}{2}} \tag{23}$$

The effective properties derived here were obtained earlier by Ament (1959). The assumptions involved in their derivation are: (i) the matrix is solid, (ii) the inclusions are spherical, (iii) the wavelengths of all waves are much longer than the inclusion radius and (iv) multiple scattering effects can be neglected. Because of the latter assumption, the

validity of this model is limited to two-phase media where the concentration of inclusions is small. Also, the effective elastic moduli in this model reduce to those found by Mal and Knopoff (1967) if the concentration of inclusions is much smaller than unity. The Mal and Knopoff model is probably valid for lower concentrations than the model derived above.

In the case of a non-viscous fluid matrix one must use (12) as the expression of the waves scattered both by the representative sphere and by each solid spherical inclusion. Introducing (12) with the appropriate starred or primed variables in (3), identifying the coefficients of the corresponding angular terms and using (22) we obtain the following composition laws

$$\frac{K-K^*}{K^*} = c \frac{K-K'}{K'} \tag{24}$$

$$\frac{\rho-\rho^*}{\rho+2\rho^*} = c \frac{\rho-\rho'}{\rho+2\rho'} \tag{25}$$

The effective shear modulus vanishes because a two-phase medium cannot sustain any shear unless there is a solid continuum. The effective P wave velocity is given by

$$\alpha^* = \sqrt{K^*/\rho^*} \tag{26}$$

It is of interest to note that the effective P wave velocity is independent of the shear modulus of the inclusions. Thus our result is identical with that obtained by Ament (1953) for suspensions of perfectly rigid spheres in a non-viscous fluid matrix.

It must be emphasized that ρ^* is an effective inertial density since (25) is a relation between inertia terms. In the case of a fluid matrix where relative motion between the inclusion and matrix can occur, the effective inertial density is different from the effective gravitational density which is given by

$$\rho_g^* = \rho(1-c) + \rho'c \tag{27}$$

Because of this difference resulting from inertia effects, the static and dynamic velocity formulae vary. In the static problem the effective bulk modulus is given by the Reuss average which is in fact equation (24), but one would have taken ρ_g^* as the density of the medium and thus the effective "static" P wave velocity would have been

$$\alpha_g^* = \sqrt{\frac{K^*}{\rho_g^*}} \tag{28}$$

The "static" velocity calculated with equation (28) can be significantly different from the effective P wave velocity given by equation (26) when the density contrast between matrix and inclusion materials is large.

Spheroidal inclusions

We again use equation (3) to obtain the effective properties. The field scattered by the representative sphere centered at ζ^0 is given by

$$\Delta u_k^*(\underline{x},\underline{\zeta}^0) = V_0 \left\{ \omega^2(\rho^*-\rho) u_i^0(\underline{\zeta}^0) G_{ki}(\underline{x},\underline{\zeta}^0) - \right.$$

$$[P^*(K^*-K)\delta_{ij} e_{pp}^0 + 2Q^*(\mu^*-\mu)(e_{ij}^0-\delta_{ij}\frac{e_{pp}^0}{3})]$$

$$\left. \frac{\partial G_{ki}}{\partial \zeta_j^0}(\underline{x},\underline{\zeta}^0) \right\}$$

(29)

where P^* and Q^* are obtained from (B-4) by letting all primed variables become starred variables. In order to evaluate the sum of the fields scattered by all spheroids within the representative sphere, we assume that (i) multiple scattering effects are negligible so that the field incident on each spheroid is also $\underline{u}^0$, (ii) the orientation of the spheroids is uniform over all directions so that the two-phase medium is isotropic on a large scale, (iii) the distribution function of the orientation can be represented by a continuous function although there is a finite number of spheroids in the representative sphere, and (iv) all inclusions are approximately located at $\underline{\zeta}^0$. Then using (15) we may write the sum of the fields scattered by all inclusions as

$$\sum_{n=1}^{N} \Delta u_k^n(\underline{x}, \underline{\zeta}^0) = \sum_{n=1}^{N} V_n \left\{ \omega^2 (\rho' - \rho) u_i^0(\underline{\zeta}^0) G_{ki}(\underline{x}, \underline{\zeta}^0) - \right.$$

$$[(\lambda' - \lambda) \delta_{ij} A_{pprs} + 2(\mu' - \mu) A_{ijrs}]$$

$$\left. e_{rs}^0 \frac{\partial G_{ki}}{\partial \zeta_j^0}(\underline{x}, \underline{\zeta}^0) \right\}$$

$$(30)$$

where V_n is the volume of the nth inclusion, N is the number of inclusions in the representative sphere and

$$A_{ijk\ell} = \frac{1}{4\pi} \int_0^\pi \sin \theta d\theta \int_0^{2\pi} U_{ijk\ell} \, d\psi \tag{31}$$

Equating (29) and (30) and setting

$$\frac{1}{V_0} \sum_{n=1}^{N} V_n = c \tag{32}$$

we obtain

$$\omega^2 G_{ki}(\underline{x}, \underline{\zeta}) u_i^0(\underline{\zeta}) [(\rho^* - \rho) - c(\rho' - \rho)] -$$

$$\left\{ \delta_{ij} e_{pp}^0 P^* (K^* - K) + 2Q^* (\mu^* - \mu) (e_{ij}^0 - \delta_{ij} \frac{e_{pp}^0}{3}) \right.$$

$$\left. -c(\lambda' - \lambda) \delta_{ij} A_{pprs} e_{rs}^0 - 2c(\mu' - \mu) A_{ijrs} e_{rs}^0 \right\} \frac{\partial G_{ki}}{\partial \zeta_j} = 0$$

$$(33)$$

Requiring that both terms are identically zero, we have the density composition law from the first term

$$\rho^* = \rho(1-c) + \rho'c \tag{34}$$

and the composition law for the elastic constants from the second term. If the incident field is purely dilatational, that is

$$e^0_{ij} = e\,\delta_{ij} \tag{35}$$

the second term becomes

$$3eP^*(K^*-K)G_{ki,i} = ceG_{ki,j}[\delta_{ij}(\lambda'-\lambda)A_{ppnn}$$
$$+ 2(\mu'-\mu)A_{ijnn}] \tag{36}$$

From the symmetries of the tensor $T_{\alpha\beta\gamma\delta}$ (see Appendix B) and the integration in (31) we find that

$$A_{ppnn} = \frac{1}{3}\,T_{iijj}$$
$$A_{ijnn} = 0 \quad \text{if } i \neq j \tag{37}$$

Combining (36) and (37) we obtain the composition law for the bulk modulus

$$\frac{K^*-K}{3K^*+4\mu} = c\,\frac{K'-K}{3K+4\mu}\,\frac{1}{3}\,T_{iijj} \tag{38}$$

The composition law for the shear modulus is obtained in a very similar way by taking the incident field as

$$e_{ij}^0 = \begin{cases} 0 & i = j \\ e & i \neq j \end{cases} \tag{39}$$

Thus we have

$$\frac{\mu^* - \mu}{6\mu^*(K+2\mu) + \mu(9K+8\mu)} = \frac{c(\mu'-\mu)}{25\mu(3K+4\mu)} \left[T_{ijij} - \frac{1}{3} T_{iijj} \right] \tag{40}$$

The scalars T_{iijj} and T_{ijij} are functions of the shape of the spheroid. They are given in the Appendix.

The essential result here is that the effective elastic moduli depend not only on the concentration but also on the shape of the inclusions (i.e. aspect ratio). This conclusion is in agreement with experimental data on porous rocks (Nur and Simmons, 1969) and with other theoretical formulations (Eshelby, 1957; Wu, 1966; Walsh, 1969). It is important to note that our assumption of non-interaction among the spheroids is violated when the ratio c/α is larger than 1 (Solomon, 1971) since the inclusions are then overlapping, at least partially.

In the above formulation, the results were for spheroids having all the same aspect ratio. These results can be easily extended to cover the case of a discrete spectrum of aspect ratios. When the concentration for each aspect ratio, $c(\alpha_m)$ is known, the effective bulk modulus is given by

$$\frac{K^* - K}{3K^* + 4\mu} = \frac{K'-K}{3K+4\mu} \sum_{m=1}^{M} c(\alpha_m) \frac{1}{3} T_{iijj}(\alpha_m) \tag{41}$$

Of course, the non-interaction assumption must still be valid and it can be expressed as

$$\sum_{m=1}^{M} \frac{c(\alpha_m)}{\alpha_m} < 1 \tag{42}$$

We can compare our results (38) and (40) with those obtained by Walsh (1969) for a two-phase medium with non-interacting spheroidal inclusions.

$$K^*-K = \frac{c}{3} T_{iijj}(K'-K)$$

$$\mu^*-\mu = \frac{c}{5} (\mu'-\mu)(T_{ijij} - \frac{1}{3} T_{iijj}) \tag{43}$$

To compare these with our results, we rewrite (38) and (40) in a slightly different form,

$$K^*-K = \frac{c}{3} (K'-K)T_{iijj} \frac{3K^*+4\mu}{3K+4\mu}$$

$$\mu^*-\mu = \frac{c}{5} (\mu'-\mu)(T_{ijij} - \frac{T_{iijj}}{3}) \frac{6\mu^*(K+2\mu)+\mu(9K+8\mu)}{5\mu(3K+4\mu)} \tag{44}$$

It is clear that our results and those of Walsh differ somewhat. They are similar if the effective medium and the matrix are not too different. This may be the case if the concentration of inclusions and/or the elastic moduli contrast between inclusion and matrix materials is small. Now if the effective moduli derived for spheroidal inclusions are specialized to the limiting case of spheres where

$$\frac{1}{3} T_{iijj} = \frac{3K+4\mu}{3K'+4\mu}$$

<div align="right">(45)</div>

$$T_{ijij} - \frac{1}{3} T_{iijj} = \frac{25\mu(3K+4\mu)}{6\mu'(K+2\mu)+\mu(9K+8\mu)}$$

the results of Walsh reduce to those of Mal and Knopoff whereas our results (i.e. (44) become (19) and (21). Thus at least in the case of spherical inclusions, our results are probably valid over a wider range of concentration than those of Walsh (1969).

NUMERICAL RESULTS AND DISCUSSION

To demonstrate the effects of the inclusions on the effective moduli and velocities of a two-phase medium w made a series of numerical calculations. For these calculations we adopted a solid matrix and inclusions of different shapes and properties to represent both dry and water-saturated rocks. The matrix parameters were chosen to represent those of the matrix of an average sandstone or quartz rich crystalline rock: $K = 0.44$ Mb, $\mu = 0.37$ Mb, $\rho = 2.70$ g/cc. For the "saturated" case we used water inclusions with the moduli: $K' = 0.022$ Mb, $\mu' = 0$, $\rho' = 1.00$ g/cc. In the case of the "dry" state, it was assumed that the pores were filled with air at atmospheric pressure (bulk modulus $K' = 1.5$ bars).

With these input parameters, two separate types of calculations were carried out. The first set of calculations was to show the effect of each pore type. For this we specified the pore shape and calculated the moduli and velocities of the composite medium as a function of concentration of pores for both the "saturated" and "dry" states. The results are shown in Figures 2a,b.

The four aspect ratios chosen are $\alpha = 1.0$ (spherical pores) and $\alpha = 10^{-1}$, 10^{-2}, 10^{-4}, representing oblate spheroidal pores of different shapes going all the way into fine cracks. For ellipsoidal pores the concentrations were varied from $c = 0$ to $c = \alpha$, the optimum limit specified by non-interaction assumption [equation (42)]. The densities were computed using equation (27).

The four examples shown in Figures 2a,b demonstrate the effects of inclusion concentrations and shapes on the effective moduli and the velocities. In all cases the moduli (K^*, μ^*) and the velocities decrease with increasing concentration of inclusions. For a given concentration the flatter inclusions have relatively greater effect than the rounder inclusions. Even a very low concentration of thin inclusions (i.e. 0.01 percent) could decrease the velocities in the composite medium by as much as ten percent or more.

The comparison of the moduli for the water-saturated or

"dry" states reveals some important effects. At a given concentration of pores, when we go from water saturated to the air saturated ("dry") state the relative change in bulk modulus is greater than the corresponding change in shear modulus. This is true regardless of the pore shape. For flat pores, the changes in both moduli are pronounced while for spherical pores only the change in the bulk modulus is apparent.

The effects of water or gas saturation on compressional and shear velocities strongly depend on pore shapes as illustrated in Figures 2a,b. For spherical pores the velocities increase when one goes from the water saturated to "dry" state. This is because the effect of density change in the composite medium is greater than the changes of the moduli. Thus velocities increase in dry state while bulk and shear moduli are decreasing, because of the greater decrease in effective densities (equation 23). For intermediate shape pores such as those with aspect ratio of about $\alpha = 0.1$, the velocities in the "dry" and water saturated states are about the same. For very thin pores and cracks, both P and S-velocities are lower in the "dry" state than in the water-saturated case, although the decrease is much more pronounced in the case of P-waves. In these cases the density changes are negligibly small; velocities in two states

are directly controlled by the effective moduli.

In a typical rock the pores are likely to represent a spectrum of shapes. Equidimensional pores in sedimentary rocks can be approximated by spheres while grain boundary spaces can be approximated by flat cracks (low aspect ratio spheroids) as shown by electron microscope studies (Timur et al., 1972). To study the effects of saturation in rocks, a second set of calculations was carried out for models of a sedimentary rock (sandstone) and a crystalline rock with representative porosities: 14.2 percent for sedimentary and 0.4 percent for crystalline. The matrix model

and the properties of the fluids (water and air) were the same as before. A spectrum of pore shapes was used in each case. For the sedimentary model the majority of pores (12 percent concentration) were assumed to be spherical pores; the remainder had smaller aspect ratios. These are listed in Table 1. For the crystalline model the majority of the pores were taken to be thin cracks as indicated by the thin section photographs (Timur et al., 1972; Brace et al., 1972).

The calculated moduli and velocities are listed in Table 1. In all cases calculations were carried out for the standard 1 atmosphere pressure. The differences in moduli and velocities between the water saturated and "dry" states are very significant. For the sedimentary rock model the compressional velocity increases about 22 percent, relative to the "dry" state when saturated with water. The shear velocity changes about 3 percent. For the crystalline rock model, although the total porosity is only 0.4 percent, the increase of compressional velocity upon saturation is about 15 percent while the change in shear velocity is about 4 percent. Velocity changes of this nature have been observed in the laboratory for dry and saturated granites (Nur and Simmons, 1969).

These two sets of examples demonstrate the relative importance of the pore shapes and the compressibility and

and density of saturating fluids on determining the velocities in rocks. If pore shapes can be specified on the basis of laboratory measurements, then the nature of saturating fluids could be determined from P and S-wave velocities.

The attenuation of elastic waves in two-phase media can be computed using the formulations given in this paper by assuming the moduli (K, μ) are complex. This is discussed in detail in the second paper (Kuster and Toksöz, 1973b) along with experimental results.

APPENDIX A

Consider an homogeneous and isotropic sphere with elastic constants λ' and μ' and density ρ' embedded in an homogeneous and isotropic infinite matrix with elastic constants λ and μ and density ρ. Let a plane P wave be incident along the x axis with displacement

$$u_x = \frac{A}{ip} e^{i(px-\omega t)} \qquad (A-1)$$

where A is the amplitude, p the wavenumber and ω the angular
frequency. The presence of the sphere generates four additional
waves: the P and S waves inside the sphere and the P and S
waves scattered into the matrix. We formulate the problem
in spherical coordinates with the origin at the center of the
sphere (Figure 1). Because of the symmetries of the problem
we need not consider the azimuthal dependence. Following
Yamakawa (1962) we express the radial and transverse dis-
placements u and v corresponding to each wave in infinite
series of spherical Bessel functions and Legendre polynomials.
Thus the incident P wave components are:

$$u_0 = -\frac{A}{p^2} \sum_{n=0}^{\infty} (2n + 1) i^n \frac{d}{dr} j_n(pr) P_n(\cos\theta)$$

$$v_0 = -\frac{A}{p^2} \sum_{n=1}^{\infty} (2n + 1) i^n \frac{j_n(pr)}{r} \frac{d}{d\theta} P_n(\cos\theta)$$

(A-2)

The scattered P waves are

$$u_1 = -\frac{1}{p^2} \sum_{n=0}^{\infty} B_n \frac{d}{dr} h_n^{(1)}(pr) P_n(\cos\theta)$$

$$v_1 = -\frac{1}{p^2} \sum_{n=1}^{\infty} B_n \frac{h_n^{(1)}(pr)}{r} \frac{d}{d\theta} P_n(\cos\theta)$$

(A-3)

The scattered S waves are

$$u_2 = - \frac{1}{s^2} \sum_{n=1}^{\infty} C_n \, n(n+1) \, \frac{h_n^{(1)}(sr)}{r} \, P_n(\cos\theta)$$

$$v_2 = - \frac{1}{s^2} \sum_{n=1}^{\infty} \frac{C_n}{r} \frac{d}{dr} \, [rh_n^{(1)}(sr)] \, \frac{d}{d\theta} P_n(\cos\theta)$$

(A-4)

The P waves in the sphere are

$$u_3 = - \frac{1}{p'^2} \sum_{n=0}^{\infty} D_n \frac{d}{dr} \, j_n(p'r) P_n(\cos\theta)$$

$$v_3 = - \frac{1}{p'^2} \sum_{n=1}^{\infty} D_n \frac{j_n(p'r)}{r} \frac{d}{d\theta} P_n(\cos\theta)$$

(A-5)

The S waves in the sphere are

$$u_4 = - \frac{1}{s'^2} \sum_{n=1}^{\infty} E_n \, n(n+1) \, \frac{j_n(s'r)}{r} \, P_n(\cos\theta)$$

$$v_4 = - \frac{1}{s'^2} \sum_{n=1}^{\infty} \frac{E_n}{r} \frac{d}{dr} \, [rj_n(s'r)] \, \frac{d}{d\theta} P_n(\cos\theta)$$

(A-6)

The $e^{-i\omega t}$ time dependence is omitted throughout for brevity and p and s (p' and s') denote the wavenumbers of P and S waves in matrix (inclusion) material. $P_n(\cos\theta)$ is the Legendre polynomial of the nth order, $j_n(z)$ is the spherical Bessel function of the nth order and $h_n^{(1)}(z)$ is the spherical Hankel function of the first kind and the nth order. We must use $h_n^{(1)}(z)$ for waves travelling radially outward because we adopted an $e^{-i\omega t}$ time dependence. The coefficients in the

series are determined from the boundary conditions on the surface of the sphere $(r = a)$. The boundary conditions are continuity of the displacements and of the normal stresses

$$\lambda(\Delta_0 + \Delta_1) + 2\mu \frac{\partial}{\partial r}(u_0 + u_1 + u_2) = \lambda'\Delta_3 + 2\mu'\frac{\partial}{\partial r}(u_3 + u_4)$$

$$\mu T = \mu'T'$$

$$u_0 + u_1 + u_2 = u_3 + u_4 \tag{A-7}$$

$$v_0 + v_1 + v_2 = v_3 + v_4$$

where

$$T = \frac{\partial}{\partial r}(v_0 + v_1 + v_2) - \frac{1}{r}(v_0 + v_1 + v_2) + \frac{1}{r}\frac{\partial}{\partial \theta}(u_0 + u_1 + u_2)$$

$$T' = \frac{\partial}{\partial r}(v_3 + v_4) - \frac{1}{r}(v_3 + v_4) + \frac{1}{r}\frac{\partial}{\partial \theta}(u_3 + u_4)$$

$$\Delta_j = \frac{1}{r^2 \sin\theta}\left[\frac{\partial}{\partial r}(r^2 \sin\theta u_j) + \frac{\partial}{\partial \theta}(r \sin\theta v_j)\right] \quad j = 0, 1 \text{ or } 3$$

Putting (A-2) to (A-6) in (A-7) we obtain the following system of four equations with four unknowns for each $n \geq 1$

$$\beta_{n1}B_n + \gamma_{n1}C_n + \delta_{n1}D_n + \varepsilon_{n1}E_n = i^n(2n+1)\alpha_{n1}A \; ,$$

$$\beta_{n2}B_n + \gamma_{n2}C_n + \delta_{n2}D_n + \varepsilon_{n2}E_n = i^n(2n+1)\alpha_{n2}A \; ,$$

$$\beta_{n3}B_n + \gamma_{n3}C_n + \delta_{n3}D_n + \varepsilon_{n3}E_n = i^n(2n+1)\alpha_{n3}A \; ,$$

$$\beta_{n4}B_n + \gamma_{n4}C_n + \delta_{n4}D_n + \varepsilon_{n4}E_n = i^n(2n+1)\alpha_{n4}A \; ,$$

$$\tag{A-8}$$

where

$$\alpha_{n1} = -\left\{ \left[(\lambda+2\mu) - \frac{2\mu(n+1)(n+2)}{\xi^2} \right] j_n(\xi) + \frac{4\mu}{\xi} j_{n-1}(\xi) \right\},$$

$$\beta_{n1} = \left[(\lambda+2\mu) - \frac{2\mu(n+1)(n+2)}{\xi^2} \right] h_n^{(1)}(\xi) + \frac{4\mu}{\xi} h_{n-1}^{(1)}(\xi),$$

$$\gamma_{n1} = \frac{-2\mu n(n+1)}{\eta^2} \left[n h_{n-1}^{(1)}(\eta) - (n+2) h_n^{(1)}(\eta) \right],$$

$$\delta_{n1} = -\left\{ \left[(\lambda'+2\mu') - \frac{2\mu'(n+1)(n+2)}{\xi'^2} \right] j_n(\xi') + \frac{4\mu'}{\xi'} j_{n-1}(\xi') \right\},$$

$$\epsilon_{n1} = \frac{2\mu' n(n+1)}{\eta'^2} \left[\eta' j_{n-1}(\eta') - (n+2) j_n(\eta') \right],$$

$$(A-9)$$

$$\alpha_{n2} = - \frac{2\mu}{\xi^2} \left[(n+2) j_n(\xi) - \xi j_{n-1}(\xi) \right],$$

$$\beta_{n2} = \frac{2\mu}{\xi^2} \left[(n+2) h_n^{(1)}(\xi) - \xi h_{n-1}^{(1)}(\xi) \right],$$

$$\gamma_{n2} = \frac{\mu}{\eta^2} \left\{ 2\eta h_{n-1}^{(1)}(\eta) + [\eta^2 - 2n(n+2)] h_n^{(1)}(\eta) \right\},$$

$$\delta_{n2} = - \frac{2\mu'}{\xi'^2} \left[(n+2) j_n(\xi') - \xi' j_{n-1}(\xi') \right],$$

$$\epsilon_{n2} = - \frac{\mu'}{\eta'^2} \left\{ 2\eta' j_{n-1}(\eta') + [\eta'^2 - 2n(n+2)] j_n(\eta') \right\},$$

$$(A-10)$$

$$\alpha_{n3} = \frac{1}{\xi} [j_{n-1}(\xi) - \frac{n+1}{\xi} j_n(\xi)],$$

$$\beta_{n3} = - \frac{1}{\xi} [h_{n-1}^{(1)}(\xi) - \frac{n+1}{\xi} h_n^{(1)}(\xi)],$$

$$\gamma_{n3} = - \frac{n(n+1)}{\eta^2} h_n^{(1)}(\eta),$$

$$\delta_{n3} = \frac{1}{\xi'} [j_{n-1}(\xi') - \frac{n+1}{\xi'} j_n(\xi')],$$

$$\epsilon_{n3} = \frac{n(n+1)}{\eta'^2} j_n(\eta'),$$

(A-11)

and

$$\alpha_{n4} = \frac{1}{\xi^2} j_n(\xi)$$

$$\beta_{n4} = - \frac{1}{\xi^2} h_n^{(1)}(\xi)$$

$$\gamma_{n4} = - \frac{1}{\eta^2} [nh_{n-1}^{(1)}(\eta) - nh_n^{(1)}(\eta)]$$

$$\delta_{n4} = \frac{1}{\xi'^2} j_n(\xi')$$

$$\epsilon_{n4} = \frac{1}{\eta'^2} [\eta' j_{n-1}(\eta') - nj_n(\eta')]$$

(A-12)

with

$$\xi = pa \qquad \eta = sa \qquad \xi' = p'a \qquad \eta' = s'a$$

For n = 0, equation (A-8) can be written as

$$\left.\begin{array}{l} \beta_{01}B_0 + \delta_{01}D_0 = \alpha_{01}A \\[2mm] \beta_{03}B_0 + \delta_{03}D_0 = \alpha_{03}A \end{array}\right\} \tag{A-13}$$

where

$$\left.\begin{array}{l} \alpha_{01} = -[(\lambda+2\mu)j_0(\xi) - \dfrac{4\mu}{\xi}j_1(\xi)] \\[3mm] \beta_{03} = [(\lambda+2\mu)h_0^{(1)}(\xi) - \dfrac{4\mu}{\xi}h_1^{(1)}(\xi)] \\[3mm] \delta_{01} = -[(\lambda'+2\mu')j_0(\xi') - \dfrac{4\mu'}{\xi'}j_1(\xi')] \end{array}\right\} \tag{A-14}$$

and

$$\left.\begin{array}{l} \alpha_{03} = -\dfrac{1}{\xi}j_1(\xi) \\[3mm] \beta_{03} = \dfrac{1}{\xi}h_1^{(1)}(\xi) \\[3mm] \delta_{03} = -\dfrac{1}{\xi'}j_1(\xi') \end{array}\right\} \tag{A-15}$$

Cramer's rule can be used to solve systems (A-8) and (A-13) for the coefficients in the series expansions of the scattered waves. When the wavelengths of all waves are much longer than the radius of the sphere (ξ, ξ', η, η' much smaller than 1) we may use the expansions of the spherical Bessel and Hankel functions for small arguments. They are for z << 1

$$j_n(z) = \frac{2^n n!}{(2n+1)!} z^n [1 - \frac{z^2}{2(2n+3)}]$$

$$h_0^{(1)}(z) = -\frac{1}{z}(1+iz) \tag{A-16}$$

$$h_n^{(1)}(z) = -\frac{i(2n)!}{2^n n! z^{n+1}} [1 + \frac{z^2}{2(2n-1)}] \qquad n \geq 1$$

Using the expansions in (A-9) to (A-12), (A-14) and (A-15) keeping only the dominant term in solving systems (A-8) and (A-13) we obtain

$$B_0 = Ai\xi^3 \frac{K-K'}{3K'+4\mu} \tag{A-17}$$

$$B_1 = \frac{A\xi^3}{3} \frac{(\rho-\rho')}{\rho} \tag{A-18}$$

$$B_2 = \frac{20iA\xi^3}{3} \frac{\mu(\mu'-\mu)}{6\mu'(K+2\mu) + \mu(9K+8\mu)} \tag{A-19}$$

$$B_n = -i^{n+1} AF_n \xi^{2n-1} \frac{\mu(\mu'-\mu)}{\left[\begin{array}{c} 2(n+1)(n-1)K\mu'+(2n^2+1)K\mu \\ +\frac{2}{3}(n-1)(7n+4)\mu\mu'+\frac{2}{3}(n+1)(n+2)\mu^2 \end{array}\right]}$$

$$n \geq 3$$

$$\tag{A-20}$$

$$C_n = \left(\frac{s}{p}\right)^{n+3} \frac{B_n}{n} \qquad n \geq 1 \tag{A-21}$$

where

$$F_n = 2n(n-1)(2n+1)(2n-1) \left[\frac{2^n n!}{(2n)!}\right]^2$$

$$K = \lambda + \frac{2}{3}\mu \qquad K' = \lambda' + \frac{2}{3}\mu'$$

For an observation point at a large distance from the sphere ($pr \gg 1$, $sr \gg 1$) we may use the asymptotic expansion of the Hankel function

$$h_n^{(1)}(z) = (-i)^{n+1} \frac{e^{iz}}{z} \qquad z \gg 1 \qquad\qquad (A-22)$$

and we may thus write the scattered P waves as

$$u_1 = -\frac{1}{p^2} \frac{e^{ipr}}{r} \sum_{n=0}^{\infty} (-i)^n B_n P_n(\cos\theta)$$

$$\qquad\qquad\qquad\qquad\qquad (A-23)$$

$$v_1 = -\frac{1}{p^2} \frac{e^{ipr}}{pr^2} \sum_{n=1}^{\infty} (-i)^{n+1} B_n \frac{d}{d\theta} P_n(\cos\theta)$$

and the scattered S waves as

$$u_2 = -\frac{1}{s^2} \frac{e^{isr}}{sr^2} \sum_{n=1}^{\infty} n(n+1)(-i)^{n+1} C_n P_n(\cos\theta)$$

$$\qquad\qquad\qquad\qquad\qquad (A-24)$$

$$v_2 = -\frac{1}{s^2} \frac{e^{isr}}{r} \sum_{n=1}^{\infty} (-i)^n C_n \frac{d}{d\theta} P_n(\cos\theta)$$

Since $pr \gg 1$ and $sr \gg 1$, v_1 can be neglected with respect to u_1, and u_2 can be neglected with respect to v_2. Furthermore in the long wavelength case all coefficients for $n \geq 3$ are of higher order than the leading coefficients. Thus, keeping only the dominant terms, we can write the scattered waves as

$$u = - \frac{iA}{p} (pa)^3 \frac{e^{i(pr-\omega t)}}{pr} [Be_0 - Be_1 \cos\theta - \frac{Be_2}{4}(3\cos2\theta+1)]$$

$$v = -iA\frac{(sa)^3}{p} \frac{e^{i(sr-\omega t)}}{sr} [Be_1 \sin\theta + \frac{3s}{4p} Be_2 \sin2\theta] \qquad (A-25)$$

where

$$Be_0 = \frac{K-K'}{3K'+4\mu}$$

$$Be_1 = \frac{\rho-\rho'}{3\rho} \qquad (A-26)$$

$$Be_2 = \frac{20}{3} \frac{\mu(\mu'-\mu)}{6\mu'(K+2\mu)+\mu(9K+8\mu)}$$

The neglected terms are of order $(pa)^5$.

When the matrix is a non-viscous fluid, there are no scattered S waves and the continuity of the transverse displacement at the boundary is not required. Thus the coefficients in the expansion of the scattered P waves are the solutions of the following systems.

for n = 0

$$\beta_{01}^0 B_0 + \delta_{01} D_0 = \alpha_{01}^0 A$$

$$\beta_{03} B_0 + \delta_{03} D_0 = \alpha_{03}^0 A$$

(A-27)

for n ≥ 1

$$\beta_{n1}^0 B_n + \delta_{n1} D_n + \epsilon_{n1} E_n = (2n+1) i^n \alpha_{n1}^0 A$$

$$\beta_{n2}^0 B_n + \delta_{n2} D_n + \epsilon_{n2} E_n = (2n+1) i^n \alpha_{n2}^0 A$$

(A-28)

$$\beta_{n3}^0 B_n + \delta_{n3} D_n + \epsilon_{n3} E_n = (2n+1) i^n \alpha_{n3}^0 A$$

The coefficients δ_{nm} and ϵ_{nm} are the same as in (A-9) to (A-11) whereas β_{nm}^0 and α_{nm}^0 are obtained from β_{nm} and α_{nm} in (A-9) to (A-11) by letting μ vanish. The calculation is now similar to that of the preceding section. In the long wavelength approximation (ζ, ζ' and η' much smaller than 1) and for an observation point at a large distance from the sphere (pr >> 1), the scattered waves can be written as

$$u = - \frac{iA(pa)^3}{p} \frac{e^{i(pr-\omega t)}}{pr} [Be_0^0 - Be_1^0 \cos\theta]$$

(A-29)

where

$$Be_0^0 = \frac{K-K'}{3K'}$$

$$Be_1^0 = \frac{\rho-\rho'}{\rho+2\rho'}$$

(A-30)

The terms neglected are of order $(pa)^5$.

APPENDIX B

To find the waves scattered by a spheroidal inclusion embedded in a solid matrix, we shall use an integral expression derived by Ma. and Knopoff (1967) for the displacement due to the waves scattered by an inclusion of arbitrary shape isolated in an infinite matrix. Denoting the displacement field of the scattered waves observed at a point $\underline{x}$ in the matrix by $\Delta u(x)$, the displacement field of the wave at a

point $\underline{\xi}$ inside the inclusion by $\underline{v}(\underline{\xi})$, the kth component of the Green's function due to a point force acting in the ith direction at a point $\underline{y}$ in the infinite matrix by $G_{ki}(\underline{x},\underline{y})$ and the elastic tensor in the matrix by c_{ijpq}, we have

$$\Delta u_k(\underline{x}) = \int_V \left\{ \omega^2(\rho'-\rho)v_i(\underline{\xi})G_{ki}(\underline{x},\underline{\xi}) \right.$$
$$\left. -(c'_{ijpq} - c_{ijpq})\frac{\partial v_p}{\partial \xi_q}\frac{\partial G_{ki}}{\partial \xi_j}(\underline{x},\underline{\xi}) \right\} d\underline{\xi} \qquad \text{(B-1)}$$

The summation convention is used and we omit for brevity the assumed $e^{i\omega t}$ time dependence. The integral is taken over the volume V of the inclusion. If the displacement and strain inside the inclusion can be estimated in terms of the incident field we can obtain the desired expression for the scattered field.

When the matrix is solid and when the wavelengths are much longer than the inclusion size, the lowest order approximation (known as the Born Approximation) to the displacement inside is the displacement one would observe if the inclusion were absent (Mal and Knopoff, 1967). In other words, we may write

$$\underline{v}(\underline{\xi}) = \underline{u}^0(\underline{\zeta}) \qquad \text{(B-2)}$$

where $\underline{\zeta}$ is the center of the inclusion. No assumption about the shape of the inclusion is required so that we can use (B-2) for a spheroidal inclusion.

Mal and Knopoff (1967) showed that for arbitrary contrast between the elastic properties, the lowest order approximation to the strain inside a __spherical__ inclusion in terms of the incident strain is given by

$$e_{k\ell}(\underline{\zeta}) = \frac{1}{3}(P-Q)e_{ii}^{0}(\underline{\zeta})\delta_{k\ell} + Qe_{k\ell}^{0}(\underline{\zeta})$$ (B-3)

where $\delta_{k\ell}$ is a Kronecker delta and

$$P = \frac{3K+4\mu}{3K'+4\mu}$$

(B-4)

$$Q = \frac{5\mu(3K+4\mu)}{6\mu'(K+2\mu)+\mu(9K+8\mu)}$$

The important feature of this result is that it is the same as that obtained by Eshelby (1957) for the static strain inside a sphere when a uniform strain is applied at infinity. Thus for a spherical inclusion and for waves of long wavelengths, the lowest order approximation is given by the solution of the corresponding static problem. We __assume__ this identity also holds for a spheroidal inclusion. The expression derived by Eshelby (1957) for the strain inside a spheroid of arbitrary orientation with respect to the fixed coordinate system of the matrix is

$$e_{ij} = U_{ijk\ell}e_{k\ell}^{0}$$ (B-5)

where

$$U_{ijk\ell} = \ell_{\alpha i}\, \ell_{\beta j}\, \ell_{\gamma k}\, \ell_{\delta \ell}\, T_{\alpha\beta\gamma\delta}$$

The ℓ_{mn} are direction cosines and $T_{\alpha\beta\gamma\delta}$ is a fourth order tensor which is described later in this Appendix.

Introducing (B-2) and (B-5) in (B-1) and using

$$c_{ijpq} = \lambda\delta_{ij}\,\delta_{pq} + \mu(\delta_{ip}\delta_{jq} + \delta_{iq}\delta_{jp}) \qquad (B-6)$$

we obtain

$$\Delta u_k(\underline{x},\zeta) = \omega^2(\rho'-\rho)u_i^0(\zeta)\int_V G_{ki}(\underline{x},\xi)\,d\xi \;-$$

$$[(\lambda'-\lambda)U_{pprs}\delta_{ij} + 2(\mu'-\mu)U_{ijrs}]e_{rs}^0\int_V \frac{\partial G_{ki}}{\partial \xi_j}(\underline{x},\underline{\xi})\,d\xi \qquad (B-7)$$

The integrals of the Green's function over the volume of the spheroid can be evaluated easily when the point of observation is at a large distance from the spheroid. With this condition we have

$$\int_V G_{ki}(\underline{x},\underline{\xi})\,d\xi \approx V G_{ki}(\underline{x},\zeta) \qquad (B-8)$$

Finally by using (B-8) and the symmetry of the Green's function we can write the displacement field scattered by a spheroid of arbitrary orientation as

$$\Delta u_k(\underline{x}, \zeta) = V \left[\omega^2 (\rho' - \rho) u_i^0(\zeta) G_{ki}(\underline{x}, \zeta) \right.$$

$$- [(\lambda' - \lambda) U_{pprs} \xi_{ij} \qquad \qquad (B-9)$$

$$\left. + 2(\mu' - \mu) U_{ijrs}] e_{rs}^0 \frac{\partial G_{ki}}{\partial \zeta_j} (\underline{x}, \zeta) \right]$$

$T_{\alpha\beta\gamma\delta}$ is a fourth order tensor whose symmetries are for an oblate spheroid with aspect ratio α

$$T_{1111} = T_{2222} \qquad T_{1133} = T_{2233}$$

$$T_{1122} = T_{2211} \qquad T_{3322} = T_{3311}$$

$$T_{1212} = T_{1221} = T_{2121} = T_{2112} \qquad\qquad (B-10)$$

$$T_{1313} = T_{1331} = T_{3113} = T_{3131}$$

$$T_{2323} = T_{2332} = T_{3223} = T_{3232}$$

We also have the relation

$$T_{1111} - T_{1122} - 2T_{1212} = 0 \qquad\qquad (B-11)$$

The scalars T_{iijj} and T_{ijij} which are used in the text are given by

$$T_{iijj} = \frac{3F_1}{F_2}$$

$$\text{(B-12)}$$

$$T_{ijij} - \frac{1}{3} T_{iijj} = \frac{2}{F_3} + \frac{1}{F_4} + \frac{F_4F_5 + F_6F_7 - F_8F_9}{F_2F_4}$$

where

$$F_1 = 1 + A\left[\frac{3}{2}(g+\phi) - R(\frac{3}{2}g + \frac{5}{2}\phi - \frac{4}{3})\right]$$

$$F_2 = 1 + A\left[1 + \frac{3}{2}(g+\phi) - \frac{R}{2}(3g+5\phi)\right] + B(3-4R)$$
$$+ \frac{A}{2}(A+3B)(3-4R)\left[g + \phi - R(g-\phi+2\phi^2)\right]$$

$$F_3 = 1 + \frac{A}{2}\left[R(2-\phi) + \frac{(1+\alpha^2)}{\alpha^2} g(R-1)\right]$$

$$F_4 = 1 + \frac{A}{4}\left[3\phi + g - R(g-\phi)\right]$$

$$F_5 = A\left[R(g+\phi-\frac{4}{3}) - g\right] + B\phi(3-4R)$$

$$F_6 = 1 + A\left[1 + g - R(g+\phi)\right] + B(1-\phi)(3-4R)$$

$$F_7 = 2 + \frac{A}{4}\left[9\phi + 3g - R(5\phi+3g)\right] + B\phi(3-4R)$$

$$F_8 = A\left[1 - 2R + \frac{g}{2}(R-1) + \frac{\phi}{2}(5R-3)\right] + B(1-\phi)(3-4R)$$

$$F_9 = A\left[g(R-1) - R\phi\right] + B\phi(3-4R)$$

$$A = \frac{\mu'}{\mu} - 1$$

$$B = \frac{1}{3}\left(\frac{K'}{K} - \frac{\mu'}{\mu}\right)$$

$$R = \frac{3\mu}{3K+4\mu}$$

$$\phi = \frac{\alpha}{(1-\alpha^2)^{3/2}} \left[\cos^{-1}\alpha - \alpha(1-\alpha^2)^{1/2}\right]$$

$$g = \frac{\alpha^2}{1-\alpha^2} (3\phi - 2)$$

ACKNOWLEDGEMENTS

REFERENCES

Ament, W.S., 1953, Sound propagation in gross mixtures:
J. Acoust. Soc. Am., 25, 638-641.

Ament, W.S., 1959, Wave propagation in suspensions: U.S.
Naval Res. Lab., Report 5307.

Biot, M.A., 1956a, Theory of propagation of elastic waves
in a fluid saturated porous solid: I. Low frequency
range: J. Ac. Soc. Am., v. 28, p. 168-178.

Biot, M.A., 1956b, Theory of propagation of elastic waves
in a fluid saturated porous solid: II. Higher frequency
range: J. Ac. Soc. Am., v. 28, p. 179-181.

Birch, F., 1966, Compressibility; elastic constants, in
Handbook of Physical Constants, S.P. Clark, ed.,
Geol. Soc. Am., Mem. 97, p. 97-173.

Brace, W.B., 1972, Cracks and pores: a closer look:
Science, v. 178, p. 162-164.

Chekin, B.S., 1970, Effective parameters of an elastic
medium with randomly distributed fractures: Izv.,
Earth Physics, 619-623 (English transl.).

Dederichs, P.H. and Zeller, R., 1973, Variational treatment
of the elastic constants of disordered materials:
Zeitschrift für Physik, 259, 103-116.

Eshelby, J.D., 1957, The determination of the elastic field
of an ellipsoidal inclusion, and related problems:
Proc. Roy. Soc. London, Ser. A, v. 241, p. 376-396.

Eshelby, J.D., 1961, Elastic inclusions and inhomogeneities, in Progress in Solid Mechanics, I.N. Sneddon and R. Hill, eds., v. 2, ch. 3, p. 89-140.

Hashin, Z., 1962, The elastic moduli of heterogeneous materials: J. Appl. Mech., v. 29E, p. 143-150.

Hashin, Z., 1964, Theory of mechanical behavior of heterogeneous media: Appl. Mech. Reviews, v. 17, p. 1-9.

Hashin, Z., 1970, Theory of composite materials: Proc. 5th Symposium on Naval Structural Mechanics, May 8-10, 1967, Pergamon Press.

Hashin, Z., and Shtrikman, S., 1963, A variational approach to the theory of the elastic behavior of multiphase materials: J. Mech. Phys. Solids, v. 11, p. 127.

Korringa, J., 1973, Theory of elastic constants of heterogeneous media: J. Math. Phys., 14, 509-513.

Kuster, G.T., 1972, Seismic wave propagation in two-phase media and its application to the earth's interior: Ph.D. Thesis, Mass. Inst. of Tech., Cambridge.

Kuster, G.T., and Toksöz, M.N., 1973, Velocity and attenuation of seismic waves in two-phase media: II. Experimental results: Geophysics, (submitted).

Lamb, H., 1932, Hydrodynamics: New York, Dover Publications.

Mal, A.K., and Knopoff, L., 1967, Elastic wave velocities in two-component systems: J. Inst. Maths. Applics., v. 3, p. 376-387.

Morse, P.M., and Feshbach, H., 1953, Methods of theoretical physics: New York, McGraw-Hill Book Co.

Nur, A., and Simmons, G., 1969, The effect of viscosity of a fluid phase on velocity in low porosity rocks: Earth Plan. Sci. Letters, v. 7, p. 99.

Solomon, S.C., 1971, Seismic wave attenuation and the state of the upper mantle: Ph.D. Thesis, Mass. Inst. of Tech., Cambridge.

Solomon, S.C., 1972, Seismic wave attenuation and partial melting in the upper mantle of North America: J. Geophys. Res., v. 77, p. 1483-1502.

Takeuchi, S. and Simmons, G., 1973, Elasticity of water-saturated rocks as a function of temperature and pressure: J. Geophys. Res., 78, 3310-3319.

Timur, A., Hempkins, W.B., and Weinbrandt, R.M., 1971, Scanning electron microscope study of pore systems in rocks: J. Geophys. Res., v. 76, p. 4932-4948.

Walsh, J.B., 1965, The effect of cracks on the compressibility of rock: J. Geophys. Res., v. 70, p. 381-389.

Walsh, J.B., 1969, New analysis of attenuation in partially melted rock: J. Geophys. Res., v. 74, p. 4333-4337.

Wu, T.T., 1966, The effect of inclusion shape on the elastic moduli of a two-phase material: Int. J. Solids and Structures, v. 2, p. 1-8.

Yamakawa, N., 1962, Scattering and attenuation of elastic
waves: Geophysical Magazine (Tokyo), v. 31, p. 63-103.

Zeller, R. and Dederichs, P.:., 1973, Elastic constants of
polycrystals: Physica Status Solidi (b), 55, 831-842.

TABLE 1

Theoretical elastic moduli and seismic velocities for examples of a sedimentary and a crystalline rock model in "dry" and "water-saturated" state. (In "dry" state the rock is saturated with air.)

PORE STRUCTURE USED FOR CALCULATIONS

Sedimentary model		Crystalline model	
Concentration (%)	Aspect ratio	Concentration (%)	Aspect ratio
12	1 (sphere)	0.01	1
2	10^{-1}	0.15	10^{-1}
0.2	10^{-2}	0.20	10^{-2}
0.2×10^{-1}	10^{-3}	0.05	10^{-3}
0.1×10^{-2}	10^{-4}	0.10×10^{-3}	10^{-5}

CALCULATED MODULI AND VELOCITIES

	K(Mb)	μ(Mb)	ρ(g/cc)	V_p(km/sec)	V_s(km/sec)
Matrix Properties	0.440	0.370	2.70	5.88	3.70
Sedimentary Model					
Water-saturated	0.276	0.186	2.44	4.62	2.75
"Dry" (air-saturated)	0.107	0.163	2.30	3.76	2.67
Crystalline Model					
Water saturated	0.420	0.303	2.693	5.53	3.35
"Dry" (air-saturated)	0.260	0.280	2.690	4.85	3.23

FIGURE CAPTIONS

Fig. 1   Schematic diagram illustrating the scattering of
           a plane wave ($\underline{u}^\circ$) by a representative sphere V_0
           (dashed circle) of the effective medium. Individual
           inclusions are outlined by solid lines. The scattered
           fields are evaluated at point $\underline{x}$.

Fig. 2a,b Elastic moduli (K, μ) and the compressional (P) and
           shear (S) velocities in a composite medium with water
           and air filled pores as a function of volume con-
           centration of inclusions. The four sets of
           diagrams demonstrate the effects of the inclusion
           shapes specified by the aspect ratio. $\alpha = 1.0$
           corresponds to spherical inclusions; $\alpha = 10^{-4}$
           represents very flat oblate spheroidal inclusions
           modeling fine cracks or grain boundaries. The
           solid curves are the water-saturated and the
           dashed curves are the air-saturated ("dry")
           cases. Note the multiplier in the concentration
           scale. The matrix moduli and velocities can be read
           at $c = 0$. Matrix density $\rho = 2.70$ g/cc. The
           inclusion moduli are: water - K' = 22 kb,
           $\mu' = 0$, and $\rho' = 1.00$ g/cc; and air - K' = 1.5 bars,
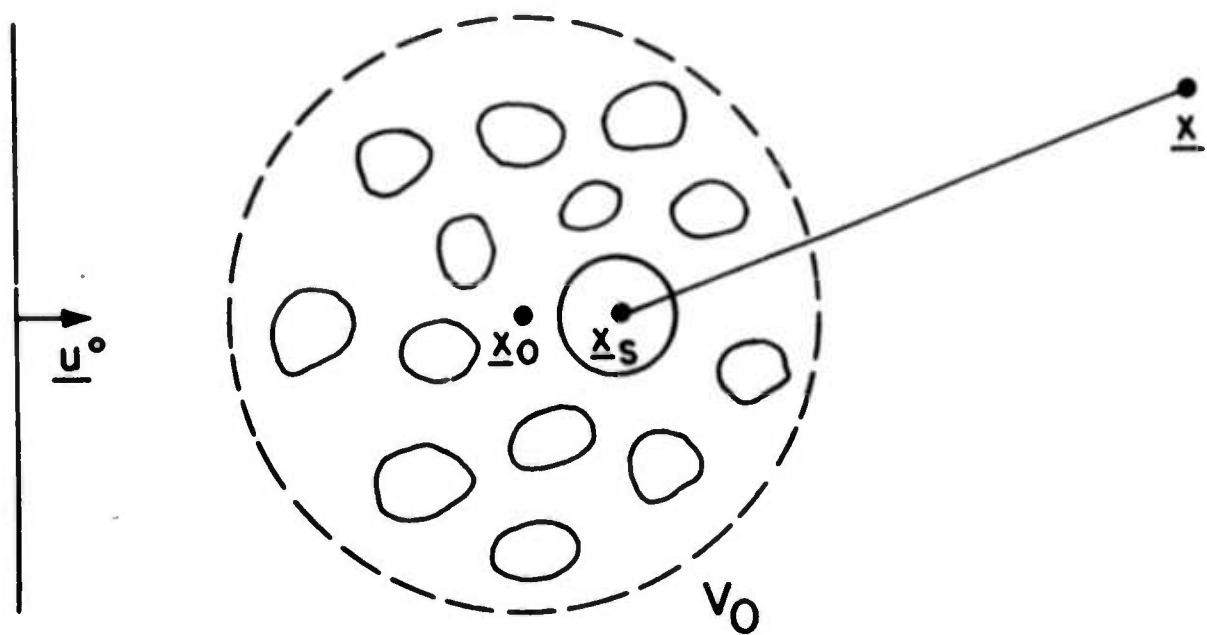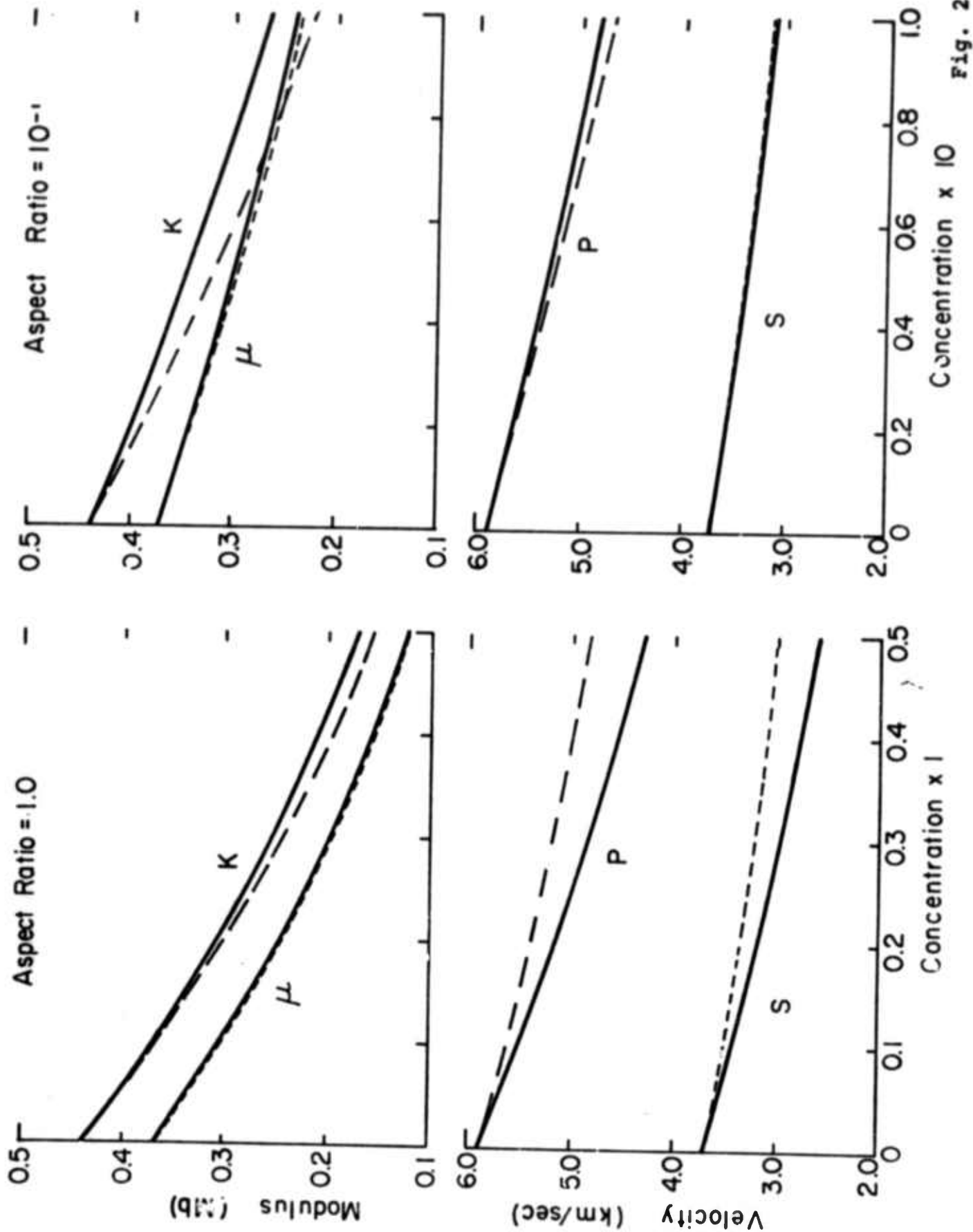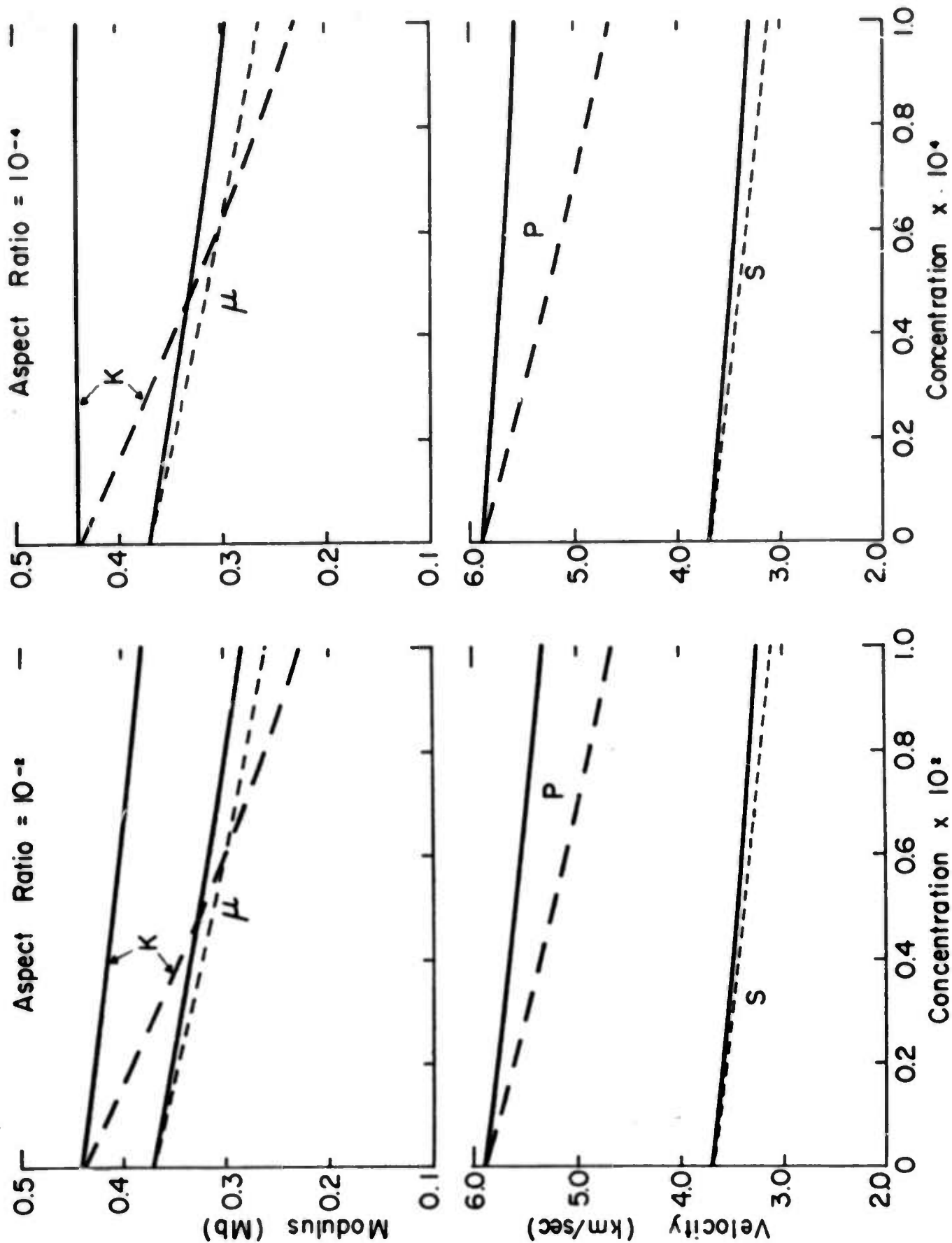 $\mu' = 0$ and $\rho' = 0.00$.

Fig. 1

Fig. 2a

Fig. 2b

4. EARTH STRUCTURE

4.1 Structure and Tectonics of the Arctic Region by Edward Dewey Chapman (abstract)

A Rayleigh wave study of the Arctic Ocean has given information on the effect of propagation of these waves across the Arctic. These waves propagate with three distinct velocity functions across the three regions of the continental shelf, mid-ocean ridge, and deep ocean basin. The basin is interpreted to have a sediment layer of 2 kilometers and a crustal basement of 15 kilometers overlaying an oceanic mantle. The Nansen Cordillera is interpreted to be a typical spreading center on the basis of these surface wave observations.

The border between the North America Plate and the Eurasia Plate in plate tectonic theory is delineated by examination of historical seismicity and regional geology. The border goes from the Lena river delta, through the Moma basin in Siberia to the city of Magadan. From there it continues down the center of Sakhalin and Hokkaido islands to a triple junction in the Japan arc. A pole of rotation between these plates is located at approximately 67°N, 155°E. This pole location explains the current seismicity of Siberia and Sakhalin island.

4.2 Prospecting for Dead Slabs by Sean C. Solomon and Rhett G. Butler (abstract)

At subduction zones that have only recently ceased to be active, the lithospheric slab may retain a seismic velocity greater than that of the surrounding mantle even after the slab becomes seismically dead. To seek the subduction zone thought to have been recently active along the western margin of North America, we examined the variation with propagation direction of P-wave travel time residuals from sources at various distances and azimuths to seismograph stations in Washington and California. The uncertainty in source location and origin time was removed by referring the travel-time delay to a nearby station overlying presumably more uniform mantle. An eastward-dipping band of anomalously early arrivals at several stations on the western flank of the Sierra Nevada and California Cascades may imply that a dead slab is present beneath northern California, though a definitive conclusion is premature at present because of a paucity of seismic sources in eastern North America. The position of the dead slab speculatively suggested by the travel-time data is roughly consistent with that predicted by others on the basis of heat flow and geochemistry in the Sierra Nevada, and the southward decrease in the magnitude of the travel-time advance associated with such a slab is in agreement with the history of subduction of the Farallon plate as reconstructed from ocean floor magnetic anomalies and continental tectonic activity.

4.3 Seismic Constraints on Ocean-Ridge Mantle Structure: Anomalous Fault-Plane Solutions From First Motions

by Sean C. Solomon and Bruce R. Julian

Summary

Fault-plane solutions from P-wave first motion studies of earthquakes on the crests of actively spreading mid-ocean ridges often appear to have non-orthogonal nodal planes. This anomaly, together with independent data from surface waves and shear waves from such events, is most simply explained as an effect of propagation of the P waves through the laterally heterogeneous mantle beneath the ridge. P-wave velocity models for the ocean-ridge mantle are derived from temperature models, the phase diagram for wet peridotite, and the expected dependence of velocity on temperature and phase. Models that successfully account for the nodal plane non-orthogonality are characterized by pronounced lateral temperature gradients and extensive partial melting at temperatures in excess of the anhydrous peridotite solidus, in agreement with models for the petrogenesis of tholeiitic basalts and with evidence for a region of very low Q beneath ridge crests. The depth to the top of the partially molten region is not well constrained, but the half-width of the zone of extensive melting in the north Atlantic must be several tens of kilometers. A prediction of these calculations is a variation of the apparent non-orthogonality of nodal planes with spreading rate for ridge-crest earthquakes; the limited data are

consistent with this variation. The most promising tests
of proposed velocity models include long seismic refraction
profiles and studies of S-wave polarization. Body-wave
travel-time residuals observed teleseismically from ocean-
ridge earthquakes are predicted to be nearly independent
of distance and azimuth and thus measurable only for events
with independently determined origin times.

1. Introduction

There is a great deal of current interest in the structure of the upper mantle beneath mid-ocean ridges. Of special importance are inferences that can be made about mantle composition and temperature from observations of phase boundaries and lateral gradients of physical properties. The temperature field is in turn coupled to the flow pattern in the mantle, in particular to the radial extent of the zone of upwelling and to the vertical velocity of flow beneath the ridge axis. In this paper we show that a reasonable interpretation of several peculiar features of ridge-crest earthquakes allows some new constraints to be placed on the seismic velocity and temperature fields in the upper mantle beneath spreading centers.

Normal-faulting earthquakes on the crests of mid-ocean ridges show an unusual characteristic which has been noted only in passing in the literature: Well-constrained fault-plane solutions derived from P-wave first motions indicate an apparent non-orthogonality of the nodal planes when standard projections are used to map observations back to the focal hemisphere. We suggest in this paper that this anomaly may be ascribed to body-wave path effects near the source, specifically to changes in propagation direction and ray parameter of P waves caused by travelling through a laterally heterogeneous velocity field in the upper mantle beneath the ridge axis. By means

of three-dimensional ray tracing for two-dimensional velocity
models of the ocean-ridge mantle, we calculate the corrections
to standard techniques necessary to map accurately body-wave
observations onto the focal sphere. Applying these correc-
tions to data from ridge crest earthquakes, we show that the
P-wave first motions can then be fit by two orthogonal nodal
planes,as expected for a double-couple source.

There are several independent sorts of information that
can be brought to bear on the modeling of seismic velocity
for the ocean-ridge mantle. Among these are the temperature
fields derived from models for mantle flow beneath a spreading
center, velocity-temperature relationships for materials
likely to constitute the upper mantle, and recent evidence
for a shallow zone of very low Q localized beneath the ridge
axis. Though a unique two-dimensional velocity model cannot yet
be selected, a combined application of these constraints indi-
cates that pronounced lateral velocity gradients, due to
temperature gradients and to regions of partial melting, are
required.

2. Focal Mechanisms of Ridge-Crest Earthquakes

The source mechanisms of earthquakes on the axes of
actively spreading mid-ocean ridges have been studied exten-
sively by Sykes (1967, 1970a) and his co-workers, using
primarily the first motions of P waves. Most such mechanisms
can be clearly classified as normal faulting, with the

inferred axis of least compressive pre-stress nearly
horizontal and roughly perpendicular to the strike of the
ridge.

All of these earthquakes for which both of the nodal
planes are well known have the anomalous characteristic
that the nodal planes fit to first-motion data projected with
a standard earth model onto the lower focal hemisphere are
not orthogonal. Rather the downward dilatational quadrant
subtends a solid angle of less than π steradians; the angle
between the best fitting nodal planes is commonly 60° to 70°.
At least six such mechanisms (see Fig. 1 and Table 1) have
been noted (Sykes 1967, 1970a; Thatcher & Brune 1971; Conant
1972), although for two of these solutions one of the nodal
planes was determined principally by its required proximity
to stations recording small first arrivals, surely a risky
procedure when dealing with waves which must propagate beneath
an actively spreading ridge.

The non-orthogonality of the nodal planes is most likely
an artifact of the projection used to map the earth's surface
back to the focal sphere. Specifically the standard tables
of ray parameter, or angle of incidence, versus epicentral
distance are inadequate when the source region is laterally
heterogeneous. If the projection of first-motion data in-
cludes the effect of propagation through a plausible velocity
model for the ocean-ridge mantle, the non-orthogonality of
the nodal planes can be made to disappear.

A particularly clear example of the apparent non-orthogonality of nodal planes determined from first-motion data for a ridge-crest earthquake is shown in Fig. 2. This earthquake, which occurred on 20 September 1969 on the Reykjanes ridge, is obviously a normal-faulting event. The angle between the nodal planes in the dilatational 'quadrant' is only about 60°, however. Two orthogonal fault planes could not be drawn on the figure without violating a large number of the data.

The first-motion data in Figure 2 were projected onto the lower focal hemisphere using the ray parameter-distance tables of Herrin (1968), though the pattern would be altered only negligibly if some other common earth model (e.g. Jeffreys-Bullen) were used. Of some effect, though, is the P-wave velocity assumed at the source. We adopted a value of 8.0 km/sec in plotting this figure. This value is reasonable for a hypocenter located in a more or less average upper mantle. Assuming a lower P velocity appropriate to ocean ridge upper mantle or to crustal rocks would shrink the dilatational first-motion field even further. Because we did not use such a lower source-region velocity, our estimate of the nodal-plane non-orthogonality is probably a conservative one. A higher P-wave velocity at the source would increase the angle between the nodal planes in Fig. 2, but the velocity would have to exceed 11 km/sec for the planes to appear orthogonal.

We cannot conclusively rule out the possibility that the non-orthogonality is real, e.g. that the earthquake source

is best represented by a double couple and a superposed
explosive component. An explosive component with P-wave
amplitude equal to .3 to .5 times the maximum P-wave ampli-
tude from the double couple would yield the observed angle
of 60° to 70° between the best fitting nodal planes. The
nodal surface. would not be planes for such a composite
source, of course, but the distinction is important only
for propagation directions in the general vicinity of the null
axis on the focal sphere. Data are rarely available for such
paths from a normal-faulting event. In particular, a source
consisting of a double couple and a superposed explosive com-
ponent with amplitude about half the maximum double-couple
ampliutde is entirely consistent with the first-motion data
in Figure 2.

There are other methods available for testing whether the
nodal plane non-orthogonality is a source effect. Neither
S waves nor Love waves generated by the earthquake should re-
flect the presence of an explosive component. S-wave polari-
zation data for at least one ridge-crest earthquake (2 June
1965) are not consistent with the double-couple source that
would be obtained by removing an explosive component of
sufficient magnitude to account for the nodal plane non-
orthogonality. Further, the seismic moments obtained for
a ridge-crest earthquake using Love waves would be expected
to be systematically lower than those obtained from Rayleigh
waves, though the difference (about a factor of 1.5) may not

be discernible. To date, double-couple source mechanisms
have been adequate to explain the radiation patterns of
both Love and Rayleigh waves from ridge events (Weidner &
Aki 1973; Forsyth 1973). In fact, the source mechanisms
that best fit the phase spectra of Rayleigh waves from two
ridge-crest earthquakes (Weidner & Aki 1973) are similar
to the non-orthogonal solutions from P-wave first motions
(Sykes 1967, 1970a) except that the nodal planes have a
more shallow dip and are orthogonal. Another possible test
might be made by examining the P-wave amplitude radiation
pattern: the maximum amplitude of the compressional lobe
would be 3 times that of the dilatational lobe for the sug-
gested composite source, though the critical comparison for
a normal-faulting event would likely be between cross-strike
paths to near stations and paths through the earth's core,
a most difficult comparison. The use of amplitudes to distin-
guish among general multipolar representations for earthquake
sources has been discussed by Randall (1972). For the reasons
mentioned above and because of the clear evidence for faulting
in the rugged, blocky topography of the mid-Atlantic ridge
(Heezen et al. 1958) we prefer a simple dislocation model for
the earthquake mechanism and we attribute the observed non-
orthogonality of nodal planes to a path effect. We admit, though,
that alternative explanations involving the source cannot yet
be completely excluded.

3. Velocity Models for the Ridge

The standard projections used to map P-wave observations onto the focal sphere are based on the assumption of spherical symmetry. This assumption is probably a serious oversimplification for active ridges (and subduction zones) where rays may be strongly bent by large horizontal gradients of the seismic velocity.

We therefore seek a two-dimensional model for compressional-wave velocity in the ocean-ridge mantle that can account for the anomalous non-orthogonality of nodal planes for ridge-crest earthquakes. This is in no sense a formal inversion; we recognize the profound nonuniqueness of the problem. Nonetheless, we can identify several features likely to be of importance for a successful model: (i) pronounced lateral temperature gradients and (ii) non-horizontal phase boundaries, particularly those associated with melting. Our approach is to construct models, insofar as possible, from first principles. We select possible temperature models for the ocean-ridge mantle from the literature, and combine these with plausible phase diagrams for mantle material and measured or estimated values for the dependence of seismic velocity on temperature and on phase (cf. Forsyth & Press 1971).

For the temperature field beneath the ridge we have used the spreading slab models of Sleep (1974) and the fluid dynamical models of Andrews (1972), though there are a number of quite similar models in the literature. Both types of models have some flexibility. For spreading slab models, we

adopted values for slab thickness, temperature at the slab base, and thermal diffusivity of 100 km, 1200°C, and 6.6×10^{-3} cm^2/sec, respectively, after Sleep (1974). The only remaining free parameter is then the spreading rate. Andrews (1972) computed a convection model for a spreading half-rate appropriate to the north Atlantic (1.2 cm/yr), though following his suggestion (D.J. Andrews, personal communication, 1972) we consider his temperature field arbitrary to within multiplication by a constant factor not too different from unity. (This is because the temperature field scales approximately as the thermal conductivity assumed for the oceanic lithosphere).

Phase boundaries in the ocean-ridge mantle we estimate by combining a chosen temperature field with Wyllie's (1971) phase diagram for peridotite in the presence of traces of water (see Fig. 3). Particularly important for the discussion below is the distinction (Ringwood 1969; Wyllie 1971) between two regimes of partial melting: (i) incipient melting, where temperatures lie between the wet solidus and dry solidus for mantle material and where only a small, temperature-insensitive volume fraction of melt is present (with the melt fraction governed primarily by water content); and (ii) normal melting, at temperatures in excess of the anhydrous solidus, where the melt fraction is large and temperature dependent.

A velocity model may be constructed from the temperature-phase field by adopting values for the temperature dependence

of velocity within single-phase regions and for the change
in velocity across phase boundaries. Adequate laboratory
measurements are available for the former quantity; we
generally used a value appropriate to magnesium-rich olivine,
$dV_p/dT = -4 \times 10^{-4}$ km/sec/C° (Kumazawa & Anderson 1969).
For the latter, a few pertinent measurements (Spetzler &
Anderson 1968) and the observation that melting boundaries
are associated with large changes in the shear modulus and
much smaller changes in the bulk modulus and in the density
allow rough estimates to be made.

Aside from the requirement that the seismic velocity
field beneath the ridge explain the several mentioned anoma-
lous characteristics of focal mechanisms of ridge-crest
earthquakes, an additional strong constraint on the tempera-
ture-phase field and thus on the velocity structure near
the ridge is provided by recent observations of shear-wave
attenuation in the mantle below the mid-Atlantic ridge
(Solomon 1973). The variation of attenuation with propaga-
tion direction from the focus of an earthquake on the Gibbs
fracture zone and from the ridge-crest event of 2 June 1965
indicated the presence of a highly attenuating (Q ~ 10 or
less) zone beneath the axis of the ridge. The zone, between
50 and 100 km in width and no deeper than 50 to 150 km, may
be readily identified as a region of extensive melting at
temperatures in excess of the anhydrous solidus of mantle
material (Solomon 1973).

In Figure 4 are shown the temperature field and associated phase boundaries which we used for constructing one such velocity model for the mid-Atlantic ridge. The lateral and vertical extent of the region in which temperatures are greater than Wyllie's (1971) dry peridotite solidus (40 km half-width, 5 to 35 km depth) are in adequate agreement with the dimensions of the region of very low Q inferred by Solomon (1973). The velocity model computed from this temperature field is also shown.

This velocity model was determined by use of a physically reasonable but admittedly arbitrary conversion from temperature and phase to compressional wave velocity (Fig. 3). The P_n velocity was taken to be 8.15 km/sec, the mean upper mantle velocity in the Pacific and Indian Oceans (Shor & Raitt 1969). At the wet solidus, a sharp velocity drop (Spetzler and Anderson 1968) of .25 km/sec was assumed. Clearly this velocity drop will depend on precisely how much melt (i.e. how much water) is present and how the melt is distributed (Walsh 1969). The quantity of melt likely at temperatures between the wet and dry solidus is on the order of 1 percent by volume (Wyllie 1971). The identification of the normal oceanic asthenosphere as a similar region of incipient melting (Kushiro et al. 1968; Lambert & Wyllie 1968; Ringwood 1969; Solomon 1972, 1973) thus provides the best guide for the P-wave velocity at such temperatures, perhaps 7.7 to 7.9 km/sec. Following Wyllie (1971), we take the melt concentration to be approximately independent of temperature between the wet and dry solidus.

The melt fraction is a rapidly increasing function of temperature above the dry solidus. We assumed a smooth drop in velocity with increasing temperature in this melting range. This smooth decrease reflects both our guess of the increase in melt content with temperature, based on a compromise between estimates of Green (1971) and Wyllie (1971), and our need to avoid large discontinuities in velocity in the ray-tracing computations. The original temperature models we used, too, did not take account of the heat of fusion, so that the melt fraction appropriate to the thermal model of Fig. 4 should vary smoothly beneath the ridge even if melt content increases sharply with temperature at the dry solidus (Wyllie 1971). At high melt concentrations, the S-wave velocty should be a function only of the bulk modulus and density of the solid and liquid phases. (The definition of 'high melt concentration' is arbitrary; we let the drop in velocity above the dry solidus follow a cosine curve, with a half cycle spread over 150°C, in constructing the model in Fig. 4.) We generally assumed that neither bulk modulus nor density changes significantly upon melting in the mantle, so that the P-wave velocity should not drop much below 6 km/sec even in a region of extensive melting. This value may be somewhat high. Laboratory measurements at zero pressure of compressional wave velocity in molten volcanic rocks yield values of 2 to 3 km/sec (Murase & Suzuki 1966; Murase & McBirney 1973), though the implied

4 to 1 ratio of compressibility of liquid to that of solid
cannot persist to very high pressure. At pressures in
excess of 5 to 10 kbar, the velocity of the molten rocks is pro-
bably substantially greater than 3 km/sec.

The P-wave velocity model in Fig 4 is oversimpli-
fied. No crust is included, nor are solid-solid phase
changes (breakdown of plagioclase to garnet) at subsolidus
temperatures. Neither of these omissions are serious,
however. At most they introduce horizontal or nearly hori-
zontal discontinuities in velocity which will not affect
the calculations below or the conclusion that pronounced
lateral velocity gradients are required in the ocean-ridge
mantle.

4. Ray Tracing Calculations

To investigate the effect on seismic wave propagation
of such two-dimensional velocity models as that of Fig. 4,
we resort to geometric ray theory. While ray theory may
have questionable validity for the long periods that dominate
the body-wave spectra from ridge-crest earthquakes, it is
probably adequate for the higher frequencies which control
P-wave first motions. The computational scheme by which rays
are traced in three dimensions through models such as in
Fig. 4 has been fully documented by Julian (1970) and has
been applied to laterally heterogeneous models of subduction
zones by Toksöz, Minear and Julian (1971) and by Davies and
Julian (1972).

Ray paths from a surface source on the ridge axis of
the velocity model of Fig. 4 are shown in Fig. 5. All of
these rays show a pronounced downward curvature. Rays
leaving the source with take-off angles (measured from
vertical) less than 15° are bent nearly to the vertical or
beyond. Rays leaving the source at take-off angles of 40°
to 50° are all bent downward by some 16°. In effect, the
pocket of low-velocity material associated with extensive
melting acts as a cylindrical lens, focusing most downward
traveling waves toward the vertical.

In general, both the horizontal phase velocity and
azimuth of a ray are affected by propagation through the
laterally heteroegeneous velocity structure. A convenient
graphical description of these effects is shown in Fig. 6.
This figure may be regarded as a correction to the standard
projections used to map teleseismic P-wave observations
back to the focal sphere. The tail of each arrow in Fig. 6
indicates the take-off angle (or, alternatively, the ray
parameter) and azimuth of a ray leaving the source. The head
of the arrow is the location on the focal sphere of the same
ray that we would have naively predicted had we measured
the ray parameter and azimuth of that ray after propagation
through the velocity model. The propagation direction
represented by the head of the arrow governs the epicentral
distance at which the ray will arrive at the earth's surface
and the apparent velocity that a seismic array would

measure. It is the propagation direction represented by the tail of the arrow that is appropriate, however, for plotting first motions on the focal sphere.

The overall effect of the ridge-mantle structure on body-wave propagation directions is, according to Fig. 6, quite pronounced. All rays are bent downward and toward the ridge axis, with the amount of bending very sensitive to take-off angle and azimuth. The model predicts that some waves will cross beneath the ridge axis, producing a region of multiple arrivals (triplication); this phenomenon is particularly evident for rays leaving the source at azimuths nearly along the ridge and at high incidence angles.

The P-wave first motions from the ridge-crest earthquakes of 20 September 1969, with the position of each point on the focal sphere corrected according to Fig. 6, are shown in Fig. 2. With the corrections, all points are moved outward from the ridge axis and two orthogonal nodal planes can be fit to the data with no difficulty. (The corrections of Fig. 6, although generally appropriate to much of the north Atlantic, are not strictly applicable to the obliquely spreading Reykjanes ridge. A slightly slower spreading rate would not affect the corrections appreciably, however; see Fig. 9 below.)

It should be noted that even if the velocity model of Fig. 4 were a correct representation of the mantle beneath the mid-Atlantic ridge, Fig. 6 is appropriate only for a particular epicenter and focal depth. There is some evidence

that ridge crest earthquakes may be shallower than a few km
in depth (Weidner & Aki 1973). The present uncertainty in
epicentral coordinates of ridge crest earthquakes, however,
is about 10 to 20 km, and normal faulting earthquakes further
than 50 km from the ridge crest have been observed (Sykes 1970b).
We therefore investigated the effect on ray paths of moving
the surface source off the ridge crest (Fig. 7). For sources
within several tens of kilometers of the ridge axis, the effect
on propagation directions of the velocity structure beneath the
ridge remains pronounced, though strongly dependent on the
source-axis offset. Both triplications and modest shadow zones
are evident in the ray tracings of Fig. 7 for sources located
5, 10 and 20 km from the ridge axis. For sources more distant
from the axis (e.g. 100 km), the effect on the velocity
structure is very modest.

5. Discussion of Velocity Models

The velocity structure of Fig. 4 is just one velocity
model, based on a reasonable temperature distribution, that
can provide an explanation for the apparent non-orthogonality
of nodal planes for ridge crest earthquakes. The critical
question is which aspects of the model are necessary for such
an explanation to hold and which aspects may be varied.

We investigated a large number of similarly constructed
velocity models, with different temperature models and differ-
ent rules for converting from temperature and phase to seismic
velocity. The universal characteristic of all models that success-
fully explained the non-orthogonality of Fig. 2 was a pro-
nounced lateral velocity gradient; changes in velocity of

that ridge crest earthquakes may be shallower than a few km
in depth (Weidner & Aki 1973). The present uncertainty in
epicentral coordinates of ridge crest earthquakes, however,
is about 10 to 20 km, and normal faulting earthquakes further
than 50 km from the ridge crest have been observed (Sykes 1970b).
We therefore investigated the effect on ray paths of moving
the surface source off the ridge crest (Fig. 7). For sources
within several tens of kilometers of the ridge axis, the effect
on propagation directions of the velocity structure beneath the
ridge remains pronounced, though strongly dependent on the
source-axis offset. Both triplications and modest shadow zones
are evident in the ray tracings of Fig. 7 for sources located
5, 10 and 20 km from the ridge axis. For sources more distant
from the axis (e.g. 100 km), the effect on the velocity
structure is very modest.

5. Discussion of Velocity Models

The velocity structure of Fig. 4 is just one velocity
model, based on a reasonable temperature distribution, that
can provide an explanation for the apparent non-orthogonality
of nodal planes for ridge crest earthquakes. The critical
question is which aspects of the model are necessary for such
an explanation to hold and which aspects may be varied.

We investigated a large number of similarly constructed
velocity models, with different temperature models and differ-
ent rules for converting from temperature and phase to seismic
velocity. The universal characteristic of all models that success-
fully explained the non-orthogonality of Fig. 2 was a pro-
nounced lateral velocity gradient; changes in velocity of

1 km/sec over horizontal distances of 15 to 25 km were gener-
ally required at some fairly shallow depth in the velocity
model. A lateral change of such a magnitude cannot arise from
temperature variations in material that is everywhere solid
and mineralogically homogeneous. Similarly, such a variation
almost certainly cannot be due to a solid-solid phase change
in the lithosphere, both because the velocity discontinuities
at phase changes likely at such depths are too small and be-
cause the pressure derivative of the transition temperature
for such reactions are generally too large. Rather such a
horizontal velocity gradient must be associated with melting
beneath the ridge, melting of such an extent to produce P-wave
velocities near 7 km/sec or less in mantle material.

There is some arbitrariness, however, in the parameters that
specify the shape of the molten region, particularly the depth
to the top of the region of extensive melting and the depth in-
terval over which such extensive melting is prevalent.
As an example, in Fig. 8 are shown the ray paths
from a surface source in a P-wave velocity model for the ocean-
ridge mantle based on the temperature calculations of Andrews
(1972). Specifically the temperature distribution is Andrews'
model for the north Atlantic, scaled by a factor of 0.94 (see
above and Solomon 1973). Temperatures in the upper 20 km be-
neath the ridge are cooler in this model than in that of Fig. 4,
but temperatures at 100 km depth are about 100°C hotter. The
simple phase diagram of Fig. 3 then predicts extensive melting
in a region 15 to 50 km deep extending to a distance of roughly

60 km from the ridge axis. A velocity model was generated from the temperature-phase field in the manner of the model of Fig. 4, except that the decrease in P-wave velocity with temperature above the anhydrous solidus was taken to occur over a narrower temperature interval (60°C).

Such a velocity model also yields the requisite downward bending of rays (Fig. 8). The dependence on take-off angle is somewhat different than in Fig. 5,however.Rays leaving the source at take-off angles less than 15° are bent only slightly. The maximum effect is for rays with take-off angles in the range 40° to 60°; these rays are bent downward by some 15° to 20°. If the appropriate corrections to focal sphere positions based on this model were applied to the first motions of Fig. 2, a source mechanism with orthogonal nodal planes could be readily fit to the data.

Thus the ray tracing calculations provide no firm constraint on the depth to the top of the region of extensive melting. Temperatures exceed the anhydrous solidus at depths greater than 5 km in the model of Fig. 4; they exceed the anhydrous solidus at depths greater than 15 km in the model on which Fig. 8 was based; and both models are acceptable from the standpoint of explaining the anomalous non-orthogonality of nodal planes for ridge-crest earthquakes. At present, other types of observations offer the best hope for discriminating among seismic models. For instance, magnetotelluric data suggest that the anhydrous solidus of peridotite is 20 km deep beneath Iceland (Hermance & Grillot 1970). Also, the basaltic rocks of the ocean floor are thought to be the product of extensive partial melting and rapid separation of liquid from solid

at 15 to 25 km depth beneath mid-ocean ridges (Kay, Hubbard & Gast 1970). We should note in this context that the low seismic velocities in our models cannot per se distinguish extensive in situ partial melting from an aggregation of melt that has separated from deeper regions of lesser melt content. Geochemical evidence that ocean-floor basalts are the products of extensive (10 to 30 percent by volume) partial melting (Kay et al. 1970) and Sleep's (1974) arguments on the inefficiency of magma segregation at low melt concentrations convince us, however, that our temperature-phase-velocity models are not unreasonable. Some upwards segregation of melt immediately beneath the ridge axis (Atwater & Mudie 1973) may deplete the melt fraction at some distance from the axis over what would be estimated from temperature and the phase diagram of undifferentiated mantle material.

The model calculations do provide some constraint on the lateral extent of melting. In the north Atlantic, at least, the region of high melt content (temperatures above the anhydrous solidus) cannot be confined to a narrow dike (cf. Kay et al. 1970), nor does it likely extend to several hundred kilometers from the ridge axis (cf. Oxburgh & Turcotte 1968). For lithosphere spreading rates comparable to that in the north Atlantic, at any given depth in the range 15 to 40 km the phase boundary identified with the anhydrous peridotite solidus extends from the ridge axis a distance of roughly one to two times the depth. The maximum half-width of the region of extensive melting is some 40 to 60 km. That region of extensive melting is relatively broad, in contrast

to the narrow zone of active intrusion on the ridge axis
(Atwater & Mudie 1973), argues that a significant quantity
of basaltic material is added to the cooling oceanic litho-
sphere below the crust (Press 1969; Forsyth & Press, 1971).

To summarize, velocity models for the ocean-ridge mantle
that explain the unusual first-motion patterns of normal-
faulting earthquakes on the ridge crest all involve substan-
tial horizontal velocity gradients which can only be
explained by partial melting at shallow depths beneath
spreading centers. An obvious corollary is that the details
of the conventional fault-plane solution of any earthquake
on the mid-ocean ridge system are suspect. The nature of
faulting (e.g. normal or strike-slip) will not be in doubt
(Sykes 1967) but such important particulars as slip vectors
or inferred principal axes of pre-earthquake stress may well
be. This will be especially true of sources with non-vertical
fault planes (e.g. most normal faults), but may also be true
to a lesser extent for strike-slip earthquakes located on
transform faults near the intersection with a ridge crest.

6. Further Possible Tests

There are a number of means by which the general features
of the velocity models presented above can be tested and
through which the range of possible models can be reduced.

A logical extrapolation of the above discussion is to
include S-wave polarization data. As a result of propagation

through a laterally heterogeneous velocity model, both the
propagation direction and the polarization angle will change.
If S-wave polarization data are corrected for such changes,
they should then be consistent with the fault-plane solution
deduced from corrected P-wave first motions. The S-wave
velocity structure can be calculated in a manner analogous
to that used above, and should serve as a check on the assump-
tions employed in constructing the P-velocity model, particu-
larly the behavior of bulk modulus and rigidity at temperatures
in excess of the solidus. A potential difficulty, however,
is that the S-wave polarization angles from ridge-crest earth-
quakes must be measured on long-period waves, for which geo-
metric ray theory may be inadequate.

    The models discussed above have been tailored specifically
to ridges in the north Atlantic. A legitimate question is
whether the procedures used to derive these models have general
applicability to spreading centers throughout the world. We
therefore examined a number of models similar in every detail
to that in Fig. 4 except that the spreading rate was
varied.   Ray paths from surface sources on the axes of
ridges spreading at a number of rates are shown in Fig. 9.

    The thermal model calculated according to Sleep (1974)
for a spreading half-rate of 0.5 cm/yr is somewhat cooler
beneath the ridge than faster spreading models. Temper-
atures in excess of the dry solidus are reached only within
a narrow dike immediately beneath the ridge axis. The lateral
gradients in P-wave velocity associated with this temperature-

phase distribution are thus more modest than those in Fig. 4
but are still significant. Some downward bending of rays
is evident for this model in Fig. 9. Rays with initial take-
off angles of 30° to 50° are bent down 6° to 7°, so that a
pure dip-slip normal fault with each nodal plane in reality
dipping at 45° to the horizontal would appear to have nodal
planes non-orthogonal by about 13°. This is in approximate
accord with observed non-orthogonality of nodal planes for
ridge-crest earthquakes in the Arctic (Table 1) and is not
inconsistent with less restrictive first motion data from earth-
quakes on other ridges with comparable spreading rates (e.g.
the Red Sea, McKenzie, Davies & Molnar 1970).

For ridges with spreading half-rates between perhaps 0.5 and
about 2.0 cm/yr, the apparent non-orthogonality of nodal planes
predicted for surface normal-faulting earthquakes on the ridge
axis increases with spreading rate. Thus for the model in
Fig. 9 with a half-rate of 1.0 cm/yr, the downward bending of
rays is quite similar but somewhat less than that shown in Fig. 5.
If the first six earthquakes in Table 1 are arranged in order of
increasing spreading rate, then the reported angle between
nodal planes decreases about as regularly as one might expect
considering the simplifications in the models, the uncertainty
in the determination of each nodal plane, and the uncertainty
in hypocentral coordinates of each earthquake.

The most pronounced distortion of ray paths occurs for spread-
ing half-rates near 2.0 cm/yr (Fig. 9). Rays with initial
take-off angles of 30° to 50° are bent towards the downward

vertical by 21° to 23°. If this model is correct, therefore, fault-plane solutions of normal faulting earthquakes on ridges with half rates of 2 cm/yr should show nodal planes at an apparent angle of roughly 45°. No such phenomenon has been observed, but neither do the currently scanty first-motion data from earthquakes on such ridges rule out such extreme effects. The angle between nodal planes listed in Table 1 for the event in the Gulf of California studied by Thatcher & Brune (1971) is something of an upper bound; a lower bound on this angle would be considerably smaller than 45°. Portions of the Carlsberg ridge are spreading at a half rate near 2.0 cm/yr. P-wave first motions from ridge-crest earthquakes in that region, though interpreted (Banghar & Sykes 1969) in terms of orthogonal nodal planes, either provide no constraint on one or both planes or are better fit by planes non-orthogonal by several tens of degrees (see especially their Fig. 4).

At high spreading rates (5 cm/yr half-rate or more), the zone of extensive melting is very broad, so the implied horizontal gradients in P-wave velocity beneath the ridge are small except at the shallow and nearly horizontal lithosphere-asthenosphere boundary. For such velocity models, the effect on ray paths is less severe than at lower spreading rates, and the downward bending increases monotonically with initial take-off angle. Rays with starting take-off angles in the range 20° to 50° are bent downward by 5° to 13° in the model with 5 cm/yr spreading half-rate (Fig. 9). These changes are

reduced by a factor of three in a model (not shown) with 10 cm/yr spreading half-rate. To our knowledge, there are no normal-faulting earthquakes on such rapidly spreading ridges large enough to determine a fault-plane solution from first motions.

The more traditional seismological tools for deciphering velocity structure may also serve as additional tests or constraints on models such as Fig. 4. Long refraction lines, out to distances great enough so that waves bottoming below the asthenosphere are first arrivals, would provide the most straightforward test. Potential problems are the very low Q in the asthenosphere beneath the ridge axis and the likelihood, if Fig 6 can be a guide, of a confusing assortment of laterally refracted arrivals. Francis (1969) has constructed such a long refraction profile along the mid-Atlantic ridge using earthquake sources and pairs of seismograph stations on Iceland. His apparent velocity data showed a good deal of scatter; apparent velocities of P waves as low as 6 km/sec at 7° epicentral distance were recorded. Nonetheless the models that fit his smoothed data bear some resemblance to the velocity-depth distribution beneath the ridge axis in Fig. 4. A long marine refraction profile using artificial sources and probably using bottom seismometers in addition to hydrophones would be the most fruitful way to test the details of the ocean-ridge mantle velocity structure.

Inversion of 'pure-path' surface-wave velocities also holds promise for resolving some of the details of lateral variation

of seismic-wave velocity within the lithosphere and astheno-
sphere (Weidner 1974; Forsyth 1973). The increase of litho-
sphere thickness, identified as the depth to the wet solidus,
with age in Fig. 4 is in approximate agreement with Weidner's
(1974) results but is less than in Forsyth's (1973) models. The
differences in Rayleigh-wave velocities and inferred models
between these studies may be real or may be a result of severe
lateral refraction effects in the Atlantic Ocean data (Forsyth
1973). The growth of the lithosphere with time in Fig. 4 could
be brought into better agreement with Forsyth's (1973) models
by reducing the estimated water content of the peridotite mantle
and thus raising the wet solidus (Kushiro et al. 1968). Because
the surface-wave velocities are more sensitive to shear velocity
than to compressional velocity and because surface
waves average laterally over distances comparable to their wave-
length, the details of models such as Fig. 4, especially the
region of extensive melting and very low velocities beneath the
ridge crest, are not well suited to study by surface-wave
analysis.

A simple measure of an anomalous velocity structure such
as in Fig. 4 is the travel-time delay of seismic waves which have
propagated through such a region. If one knew the origin
time and hypocenter of a ridge-crest event, then measurement
of the delay (with respect to standard tables) as a function
of propagation direction would be straightforward. Thatcher
& Brune (1971) have estimated in this manner the travel-time
delay of P-waves from events on the spreading center in the

Gulf of California to be about 2 sec. Conversely, the average delay at a station on the ridge crest could be compared to that at a station overlying older sea floor if records from a number of teleseismic sources were available. The P-wave delay at Iceland, for instance, is over 1 sec greater than at stations in stable continental areas of Greenland, Scandinavia, and Scotland (Tryggvason 1964; Long & Mitchell 1970).

As a guide to possible future studies of delay times at ridge crests, we calculated the P-wave delays for a ridge-crest source atop the velocity model of Fig. 4 relative to the travel-times for a source at the edge of our velocity model (roughly 20 m.y. old sea-floor). These delays are shown plotted on a focal-sphere projection (Davies & McKenzie 1969) in Fig. 10. The mean residual averaged over the focal sphere is about +0.6 sec. This delay would be slightly greater if the comparison were made with lithosphere older than 20 m.y. The variation of residual with propagation direction is slight, except for paths at large take-off angles nearly along the ridge axis. In this situation, there is an ambiguity between the travel time anomaly and the unknown origin time of an earthquake. Thus, teleseismic travel times could be used to constrain the velocity structure of the ocean-ridge mantle only if the hypocenter and origin time of a ridge-crest event were known from independent information; and even then the only constraint would probably be a travel-time offset largely insensitive to propagation direction.

In conclusion, there are a number of additional techniques which, with various likelihoods of success, offer the potential for testing the velocity models proposed to explain the apparent non-orthogonality of nodal planes for ridge-crest earthquakes. The most promising are long refraction profiles, examination of S-wave polarization data from similar earthquakes, and possibly the measurement of travel-time delays of P and S waves from sources on or near ridge-crests.

Acknowledgements

S.C. Solomon:

    Department of Earth and Planetary Sciences
    Massachusetts Institute of Technology
    Cambridge, Massachusetts   02139

B.R. Julian:

    Lincoln Laboratory
    Massachusetts Institute of Technology
    Cambridge, Massachusetts   02139

References

Andrews, D.J., 1972. Numerical simulation of sea-floor spreading, J. geophys. Res., 77, 6470.

Atwater, T. & Mudie, J.D., 1973. Detailed near-bottom geophysical study of the Gorda rise, J. geophys. Res., 78, 8665.

Banghar, A.R. & Sykes, L.R., 1969. Focal mechanisms of earthquakes in the Indian Ocean and adjacent regions, J. geophys. Res., 74, 632.

Chase, C.G., 1972. The N plate problem of plate tectonics, Geophys. J. R. astr. Soc., 29, 117.

Conant, D.A., 1972. Six new focal mechanism solutions for the Arctic and a center of rotation for plate movements, M.A. Thesis, Columbia Univ., New York, 18 pp.

Davies, D. & Julian, B.R., 1972. A study of short period P-wave signals from Longshot, Geophys. J. R. astr. Soc., 29, 185.

Davies, D. & McKenzie, D.P., 1969. Seismic travel-time residuals and plates, Geophys. J. R. astr. Soc., 18, 51.

Francis, T.J.G., 1969. Upper mantle structure along the axis of the mid-Atlantic ridge near Iceland, Geophys. J. R. astr. Soc., 17, 507.

Forsyth, D.W., 1973. Anistropy and the structural evolution of the oceanic upper mantle, Ph.D. thesis, Massachusetts Institute of Technology, Cambridge, 254 pp.

Forsyth, D.W. & Press, F., 1971. Geophysical tests of petrological models of the spreading lithosphere, J. geophys. Res., 76, 7963.

Green, D.H., 1971. Compositions of basaltic magmas as indicators of conditions of origin: Application to oceanic volcanism, Phil. Trans. Roy. Soc. Lond., Ser. A, 268, 707.

Heezen, B.C., Tharp, M. & Ewing, M., 1959. The floors of the oceans, 1, The North Atlantic, Geol. Soc. Amer. Spec. Paper 65, 122 pp.

Hermance, J.F. & Grillot, L.R., 1970. Correlation of magnetotelluric, seismic, and temperature data from southwest Iceland, J. geophys. Res., 75, 6582.

Herrin, E., 1968. Seismological tables for P, Bull. seism. Soc. Am., 58, 1197.

Julian, B.R., 1970. Ray tracing in arbitrarily heterogeneous media, M.I.T. Lincoln Lab. Tech. Note 1970-45.

Kay, R., Hubbard, N.J. & Gast, P.W., 1970. Chemical characteristics and origin of oceanic ridge volcanic rocks, J. geophys. Res., 75, 1585.

Kushiro, I., Syono, Y. & Akimoto, S., 1968. Melting of a peridotite nodule at high pressures and high water pressures, J. geophys. Res., 73, 6023.

Lambert, I.B. & Wyllie, P.J., 1968. Stability of hornblende and a model for the low velocity zone, Nature, 219, 1240.

Long, R.E. & Mitchell, M.G., 1970. Teleseismic P-wave
    delay time in Iceland, Geophys. J. R. astr. Soc., 20,
    41.

McKenzie, D.P., Davies D. & Molnar, P., 1970. Plate tecton-
    ics of the Rea Sea and East Africa, Nature, 226, 243.

Murase, T. & McBirney, A.R., 1973. Properties of some common
    igneous rocks and their melts at high temperatures,
    Geol. Soc. Am. Bull., 84, 3563.

Murase, T. & Suzuki, T., 1966. Ultrasonic velocity of longitu-
    dinal waves in molten rocks, J. Fac. Sci. Hokkaido Univ.,
    Ser. 7, 2, 273.

Oxburgh, E.R. & Turcotte, D.L., 1968. Mid-ocean ridges and
    geotherm distribution during mantle convection, J. geophys.
    Res., 73, 2643.

Press, F., 1969. The suboceanic mantle, Science, 165, 174.

Randall, M.J., 1972. Multipolar analysis of the mechanisms
    of deep-focus earthquakes, in Methods in Computational
    Physics, 12, ed. by B.A. Bolt, Academic Press, p. 267.

Ringwood, A.E., 1969. Composition and evolution of the upper
    mantle, in The Earth's Crust and Upper Mantle, ed. by
    P.J. Hart, Amer. Geophys. Un. Mon. 13, p. 1.

Shor, G.G., Jr. & Raitt, R.W., 1969. Explosion seismic refrac-
    tion studies of the crust and upper mantle in the Pacific
    and Indian Oceans, in The Earth's Crust and Upper Mantle,
    ed. by P.J. Hart, Amer. Geophys. Un. Mon. 13, p. 225.

Sleep, N.H., 1974. Segregation of magma from a mostly crystal-
    line mush, Geol. Soc. Am. Bull., in press.

Solomon, S.C., 1972. Seismic-wave attenuation and partial melting in the upper mantle of North America, *J. geophys. Res.*, *77*, 1483.

Solomon, S.C., 1973. Shear-wave attenuation and melting beneath the mid-Atlantic ridge, *J. geophys. Res.*, *78*, 6044.

Sykes, L.R., 1967. Mechanism of earthquakes and nature of faulting on the mid-oceanic ridges, *J. geophys. Res.*, *72*, 2131.

Sykes, L.R., 1970a. Focal mechanism solutions for earthquakes along the world rift system, *Bull. seism. Soc. Am.*, *60*, 1749.

Sykes, L.R., 1970b. Earthquake swarms and sea-floor spreading, *J. geophys. Res.*, *75*, 6598.

Thatcher, W. & Brune, J.N., 1971. Seismic study of an oceanic ridge earthquake swarm in the Gulf of Calif., *Geophys. J. R. astr. Soc*, *22*, 473.

Toksöz, M.N., Minear, J.W. & Julian, B.R., 1971. Temperature field and geophysical effects of a downgoing slab, *J. geophys. Res.*, *76*, 1113.

Tryggvason, E., 1964. Arrival times of P waves and upper mantle structure, *Bull. seism. Soc. Am.*, *54*, 727.

Walsh, J.B., 1969. A new analysis of attenuation in partially melted rock, *J. geophys. Res.*, *74*, 4333.

Weidner, D.J., 1974. Rayleigh wave phase velocities in the Atlantic Ocean, *Geophys. J. R. astr. Soc.*, *36*, 105.

Weidner, D.J. & Aki, K., 1973. Focal depth and mechanism
of mid-ocean ridge earthquakes, J. geophys. Res., 78,
1818.

Wyllie, P.J., 1971. Role of water in magma generation and
initiation of diapiric uprise in the mantle, J. geophys.
Res., 76, 1328.

Table 1. Ridge-crest earthquakes with reported

non-orthogonal nodal planes

	Date	Origin Time G.M.T.	Lat	Long	Spreading half-rate[a] cm/yr	Angle between nodal planes	Reference
1.	7 April 1969	20:26:30.5	76.55°N	130.86°E	0.7	78	Conant (1972)
2.	25 August 1964	13:47:19.3	78.15°N	126.65°E	0.7	73	Sykes (1967)
3.	31 May 1971	03:46:52.2	72.2 °N	1.2 °E	1.1	64	Conant (1972)
4.	20 September 1969	05:08:57.8	58.35°N	32.08°W	1.3	60	Figure 2
5.	16 November 1965	15:24:44.0	31.00°N	41.53°W	1.1	73[b]	Sykes (1967)
6.	2 June 1965	23:40:23.1	15.93°N	46.69°W	1.5	67[b]	Sykes (1967)
7.	20 March 1969	08:17:45.1	31.32°N	114.18°W	2.6	66	Thatcher and Brune (1971)

Source of epicenter data: International Seismological Centre and National Oceanic and

Atmospheric Administration

[a]Calculated from relative plate velocities of Chase (1972).

[b]One plane constrained primarily by proximity of low-amplitude first arrivals.

Figure Captions

Fig. 1 Location of ridge-crest earthquakes for which P-wave
first motions indicate non-orthogonal nodal planes.
Events are numbered as in Table 1. Plate boundaries are
shown by heavy lines. Azimuthal equidistant projection
about the north pole.

Fig. 2 Left: Conventional fault-plane solution from P-wave
first motions for the earthquake of September 20, 1969
(equal area projection). Open circles are dilatations,
closed circles are compressions, and circles with superposed
crosses indicate probable proximity to a nodal plane.
Smaller symbols represent somewhat less reliable readings
than larger ones. All data were read from long-period
records of the WWSSN or the Canadian network. The strike
ϕ and dip δ of the implied nodal planes are also given.
The angle between the nodal planes is 60°.

Right: Same first-motion data corrected for propagation
through the ocean-ridge mantle (Fig. 4) according to Fig. 6.
The new fault-plane solution has orthogonal nodal planes.

Fig. 3 Melting relations for peridotite in the presence of
0.1% water, from Wyllie (1971). The solidus at low pres-
sures (shallow depths) is controlled by the breakdown of
hornblende.

Inset: Adopted dependence of compressional wave velocity
V_p on temperature and phase. The particular curve shown
corresponds to 20 km depth but the sharp drop at the wet

solidus (T_1) and the smooth decrease above the anhydrous solidus (T_2) are maintained at all depths.

Fig. 4 Top: Isotherms and regions of melting in the spreading oceanic lithosphere. The temperature distribution is calculated according to Sleep (1974) for a spreading half-rate of 1.2 cm/yr. The regions of incipient and extensive melting are determined from this temperature distribution and the phase diagram of Fig. 3.

Bottom: Contours of constant compressional-wave velocity. The conversion from temperature and phase to velocity follows Fig. 3 and the arguments in the text.

Fig. 5 Ray paths from a surface earthquake on the axis of the ridge model of Fig. 4. All rays remain in a vertical plane perpendicular to the ridge axis. Distances along the earth's surface are marked in km; no vertical exaggeration. Rays are spaced by 5° in initial take-off angle, from 0° to ±70°.

Fig. 6 Theoretical distortion of apparent locations of P waves on the focal sphere caused by propagation through the upper mantle model of Fig. 4 from a surface focus on the axis of a north-south ridge. Each arrow connects the location of the ray at the focus (tail of arrow) with the location corresponding to the ray direction at a depth of 80 km (head of arrow - indicated by asterisk). The lower focal hemisphere is shown in equal area projection and rays are spaced by 10° in azimuth and take-off angle

(from 20° to 30°) at the focus. Only rays in the
right half of the focal sphere are included for clarity.

Fig. 7 Ray paths from surface earthquakes at various distances
(5, 10, 20, 100 km) from the axis of the ridge model of
Fig. 4. Other particulars as in Fig. 5.

Fig. 8 Ray paths from a surface earthquake on the axis of an
alternative ridge model based on the temperature model of
Andrews (1972); see text. Other particulars as in Fig. 5.

Fig. 9 Dependence of distortion of ray paths on spreading
rate. All ray paths are from surface events on ridge
axes. Velocity models are calculated analogously to that
in Fig. 4 except for the different spreading rates. Other
particulars as in Fig. 5.

Fig. 10 Left: P-wave travel-time residuals predicted for a
surface source on the ridge axis of the model of Fig. 4.
Plusses are positive residuals; circles are negative
residuals. The diameter of a symbol is linearly propor-
tional to the magnitude of the residual; the symbols at
lower center are ±1.0 sec. Points are plotted on the
focal sphere (equal area projection) according to the
azimuth and ray parameter of the wave at the bottom of
the laterally heterogeneous ridge model. Only rays
leaving the source in the right half of the lower focal
sphere are plotted for clarity.

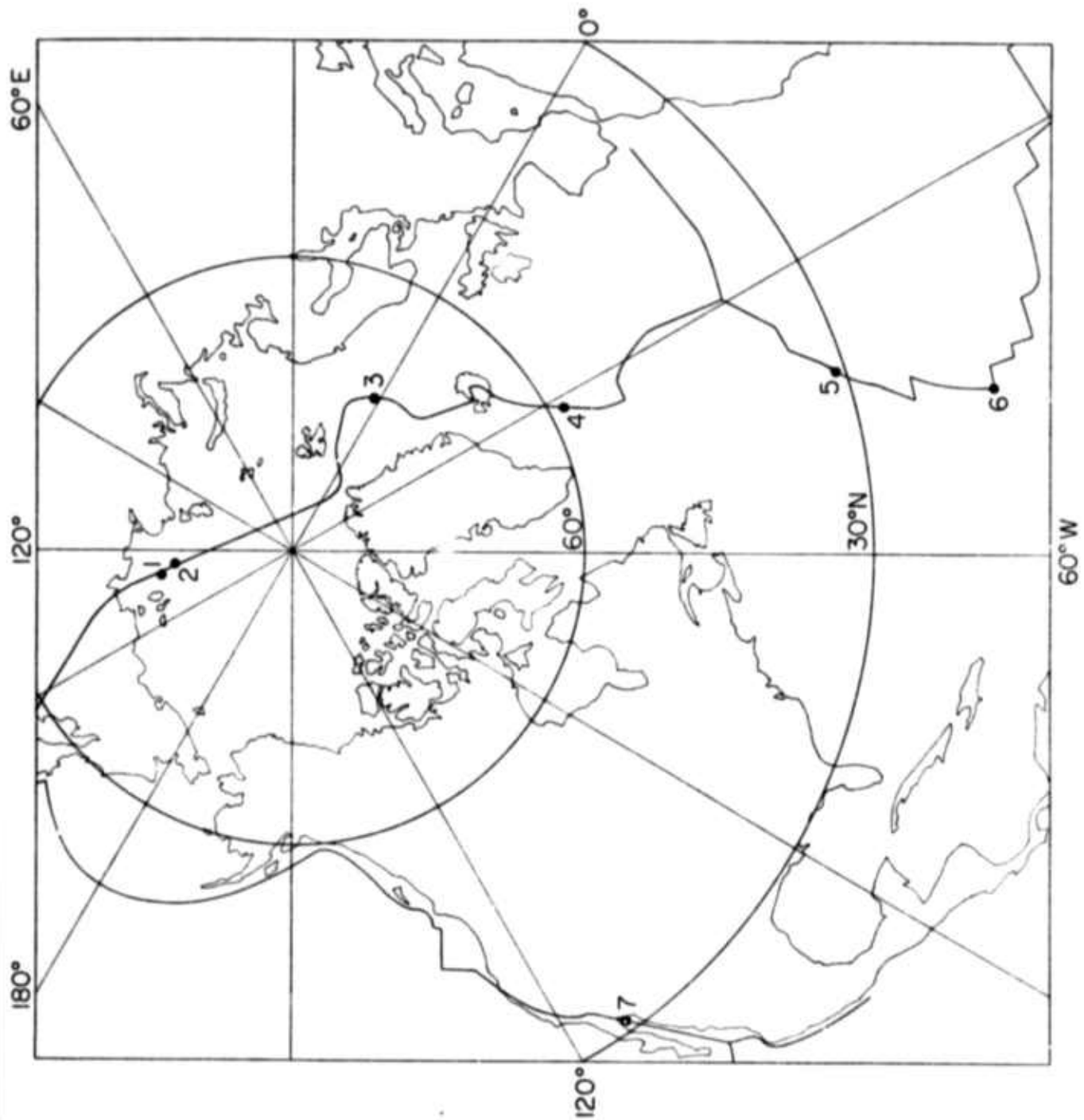Right: Same data after subtracting 0.6 sec from each
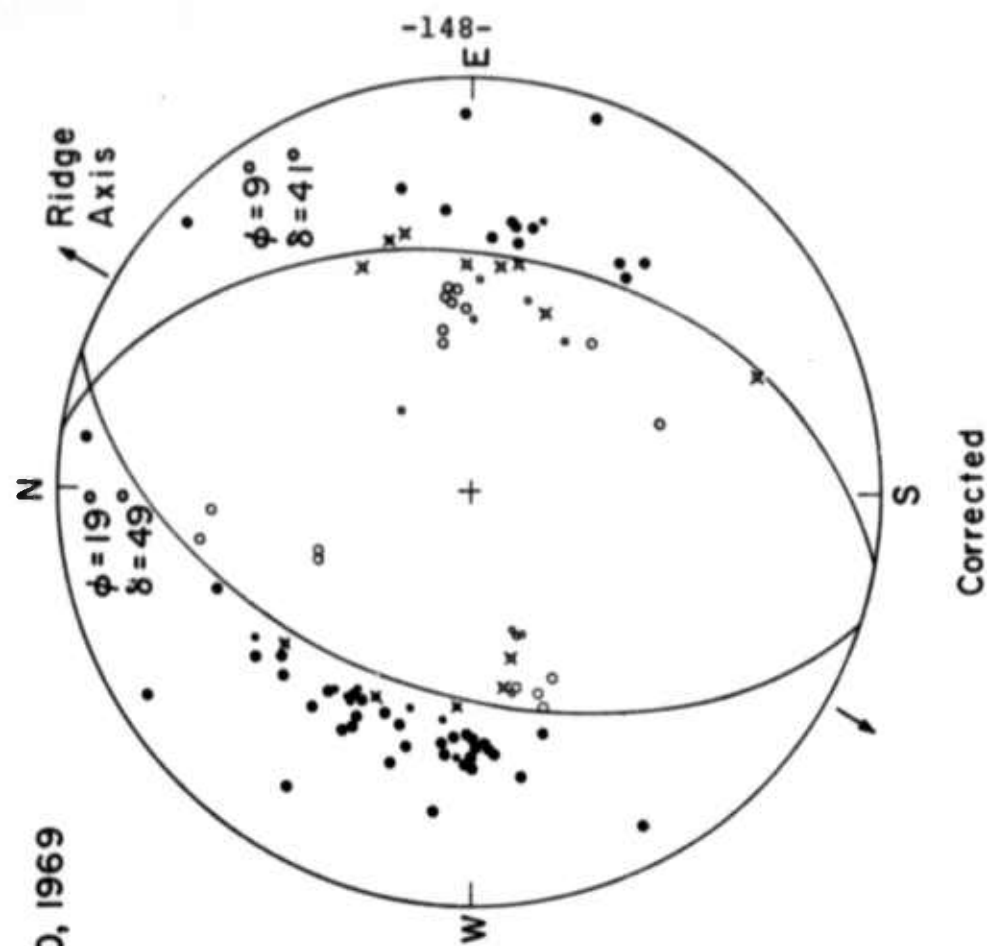residual.

Fig. 1

September 20, 1969

φ = 9°
δ = 41°

φ = 19°
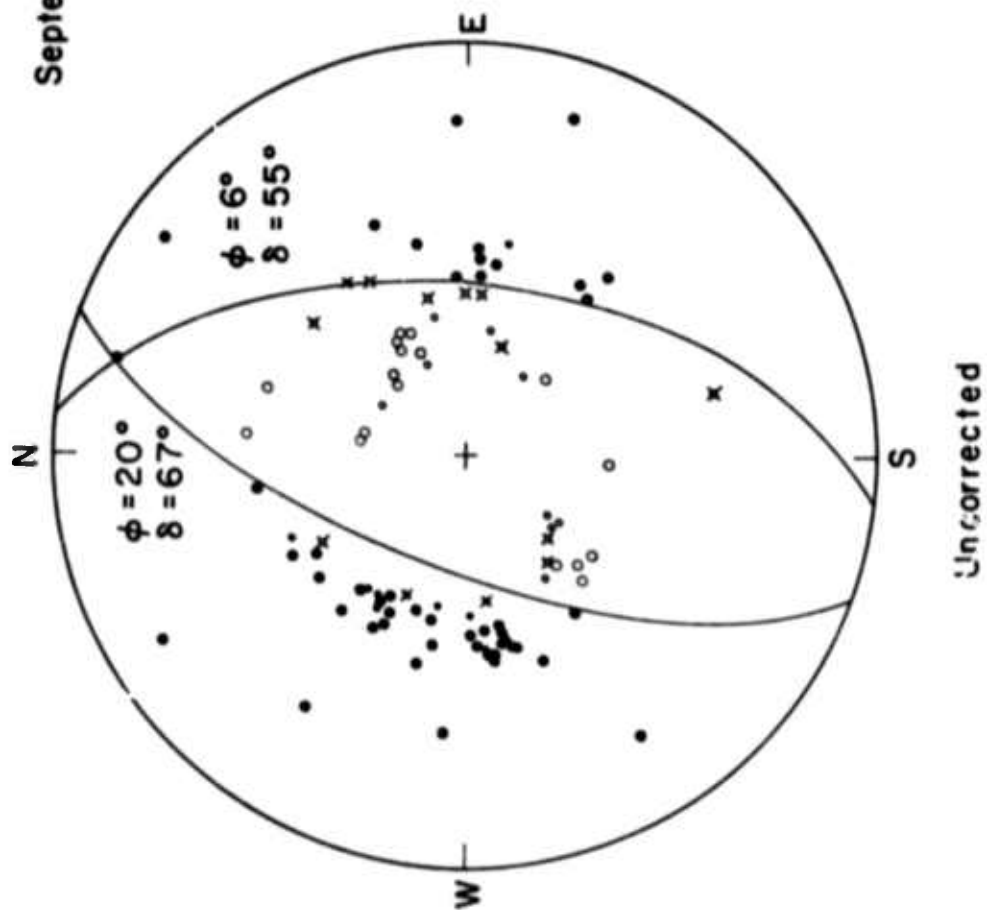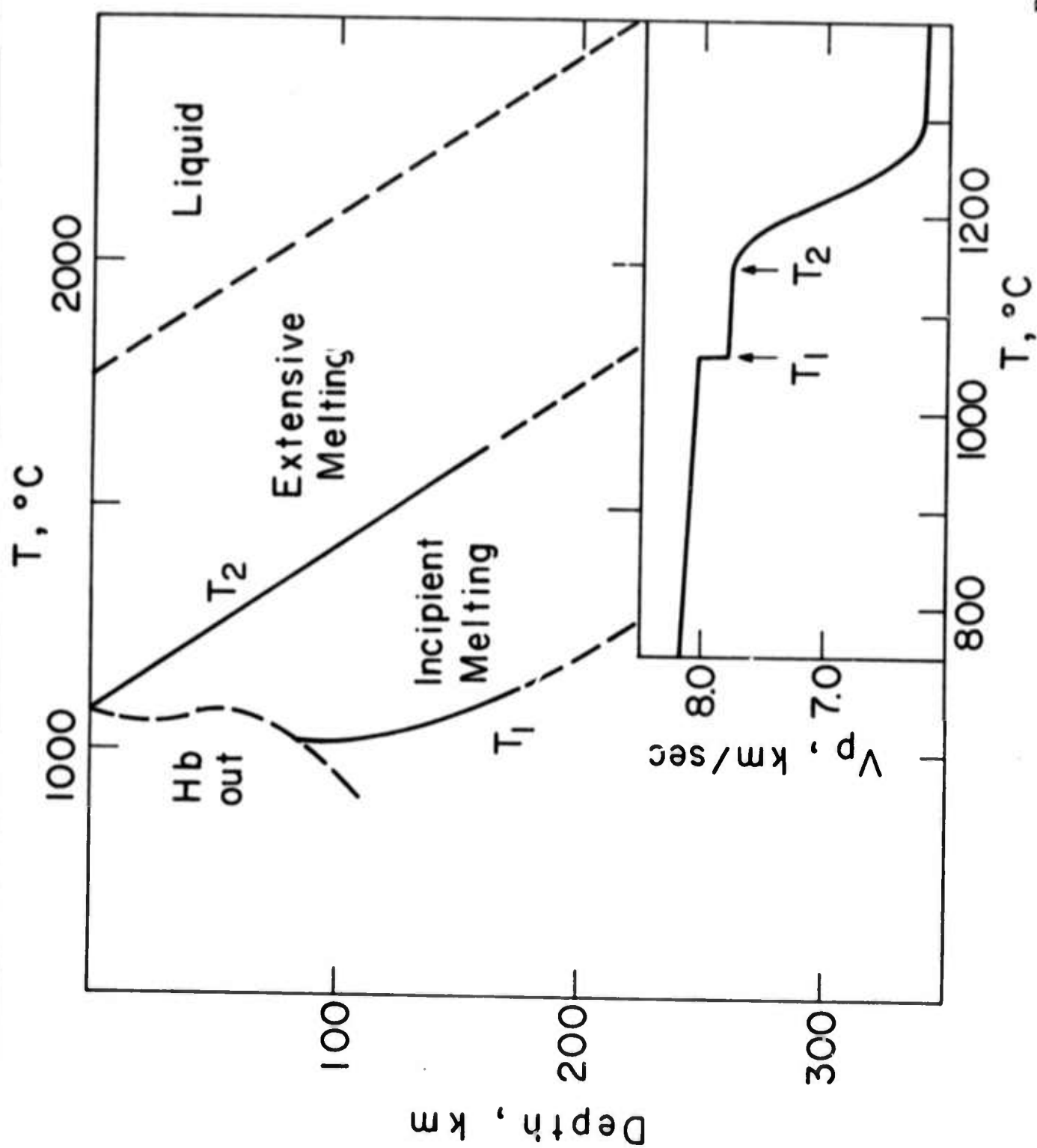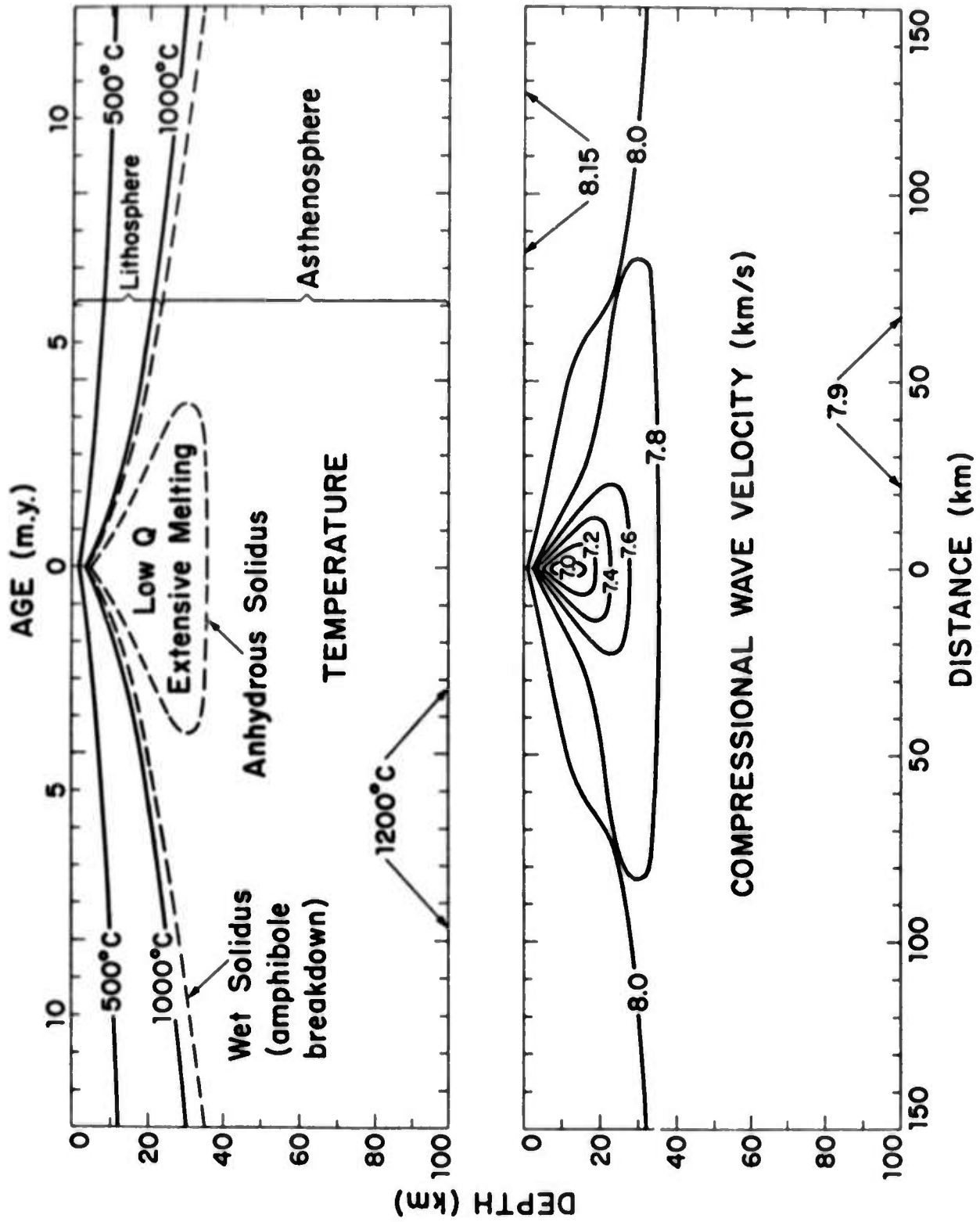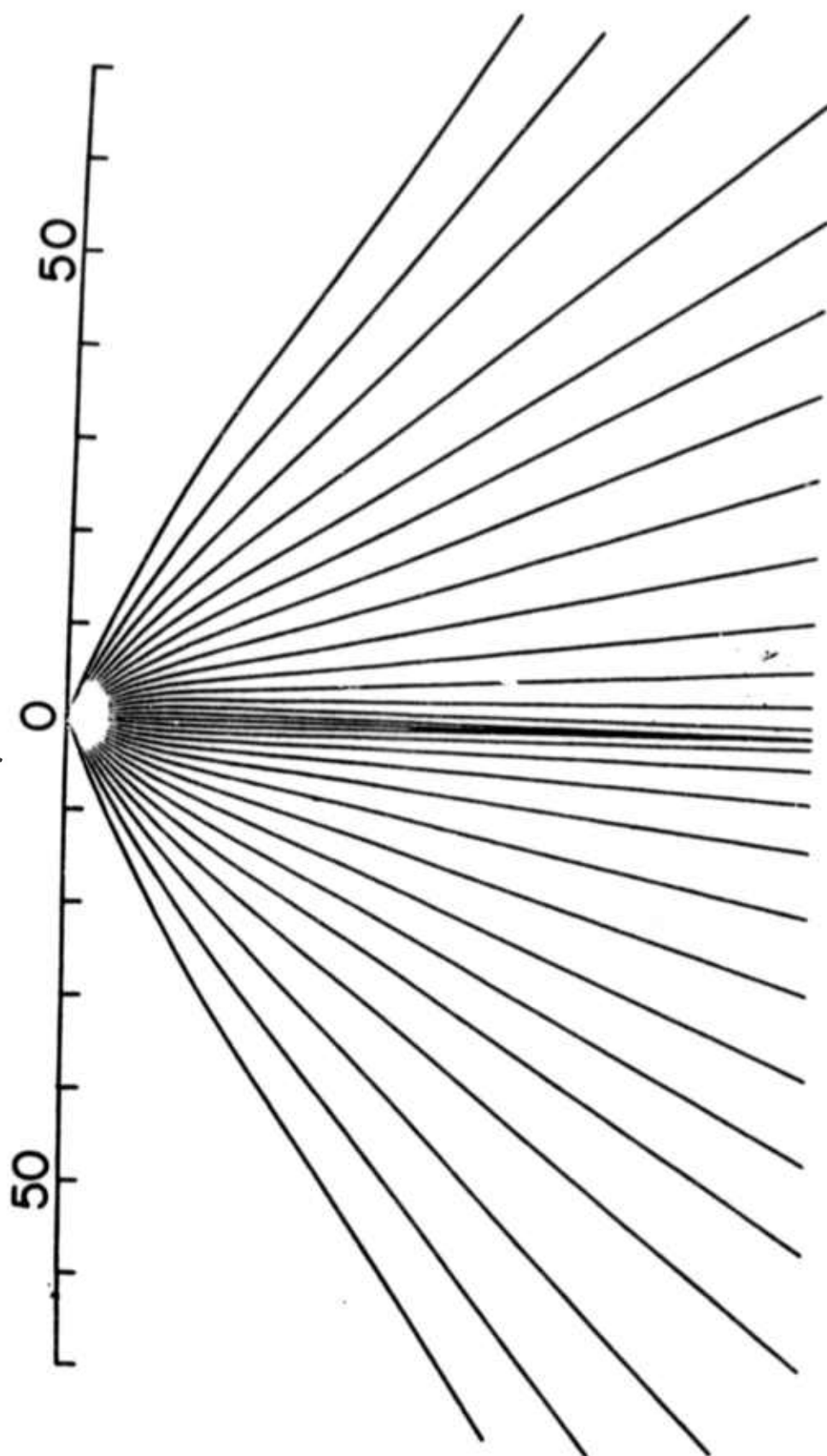δ = 49°

Ridge
Axis

Corrected
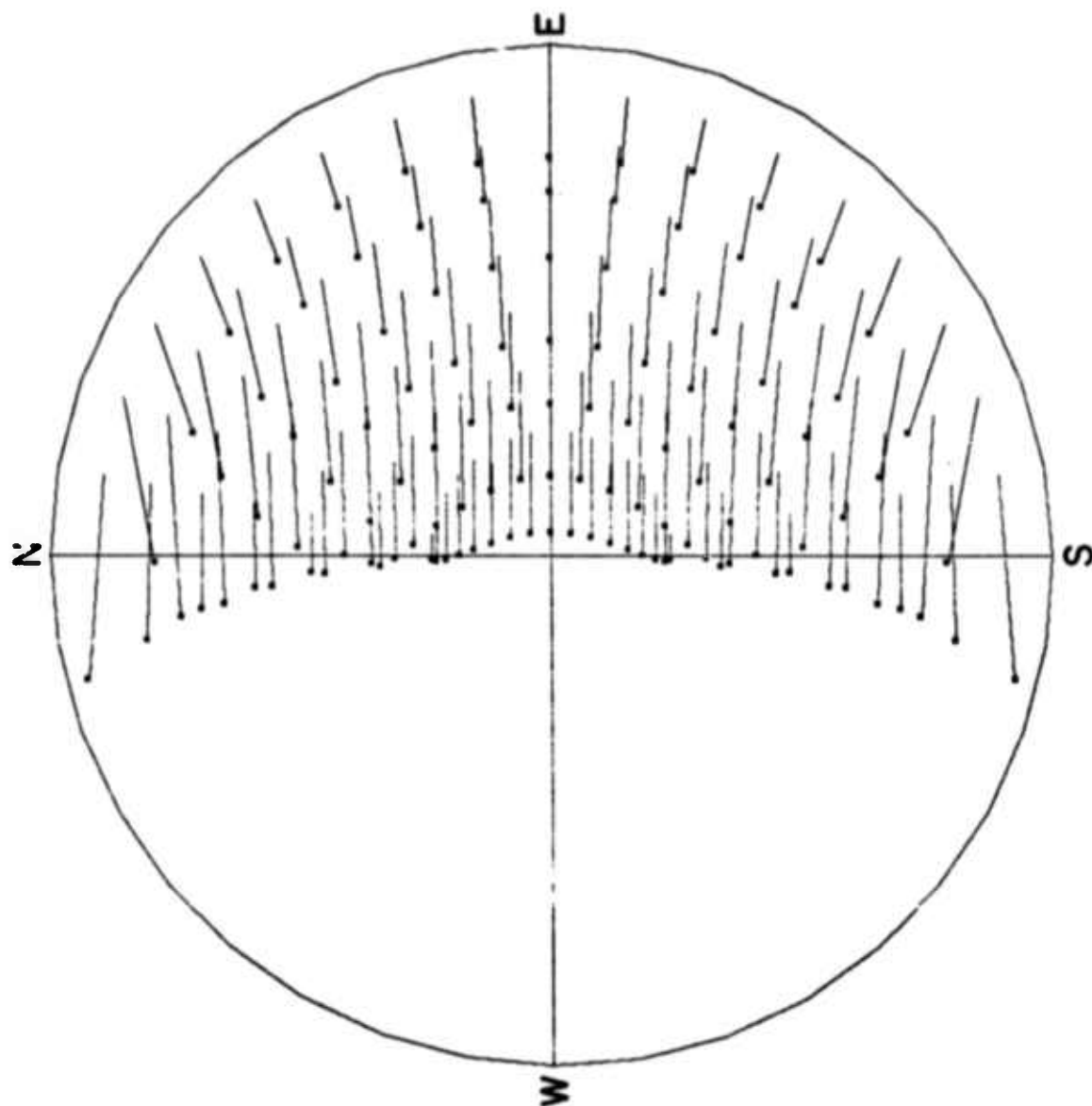
φ = 6°
δ = 55°

φ = 20°
δ = 67°

Uncorrected

Fig. 2

Fig. 3

Fig. 4

Fig. 5

Fig. 6

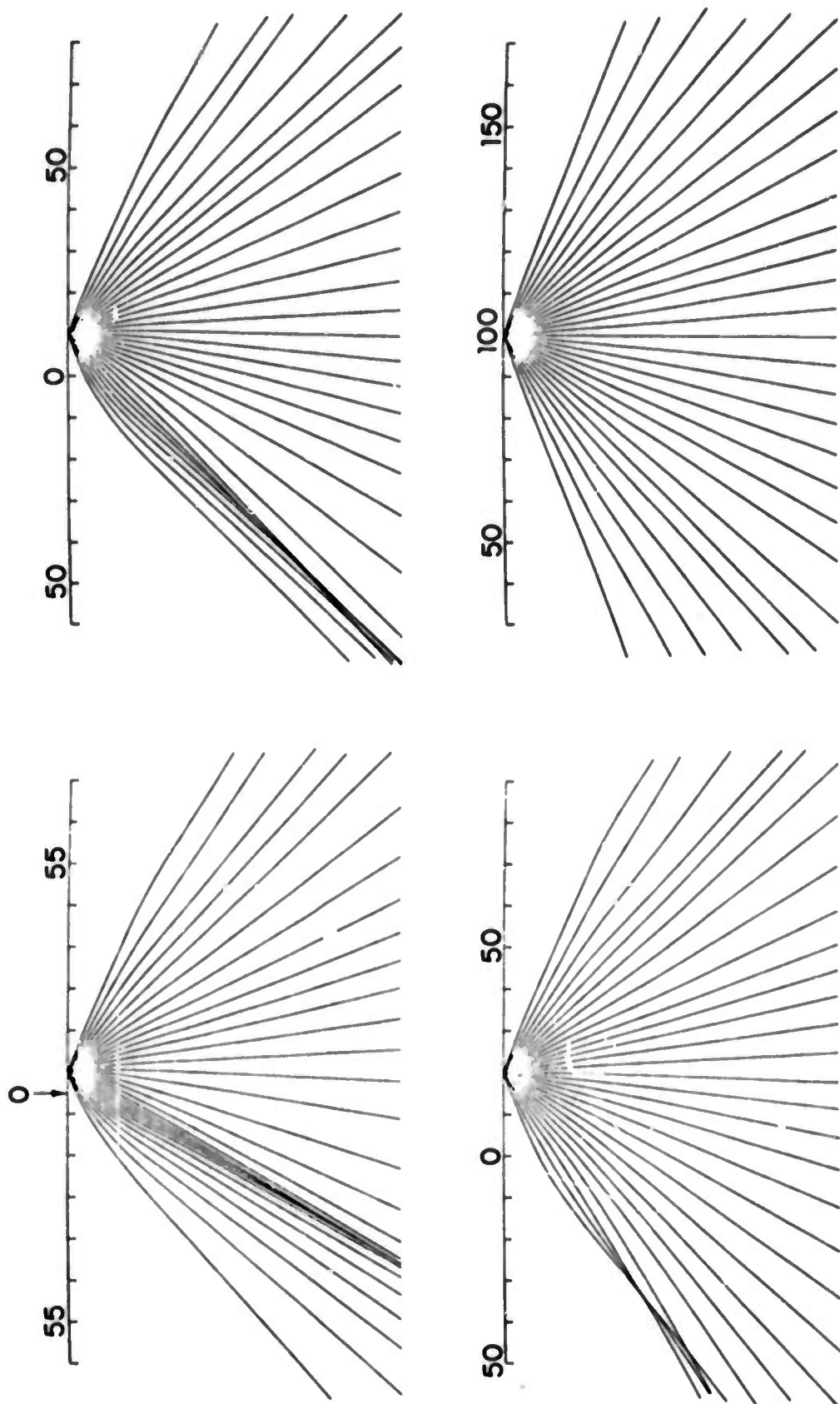Fig. 7

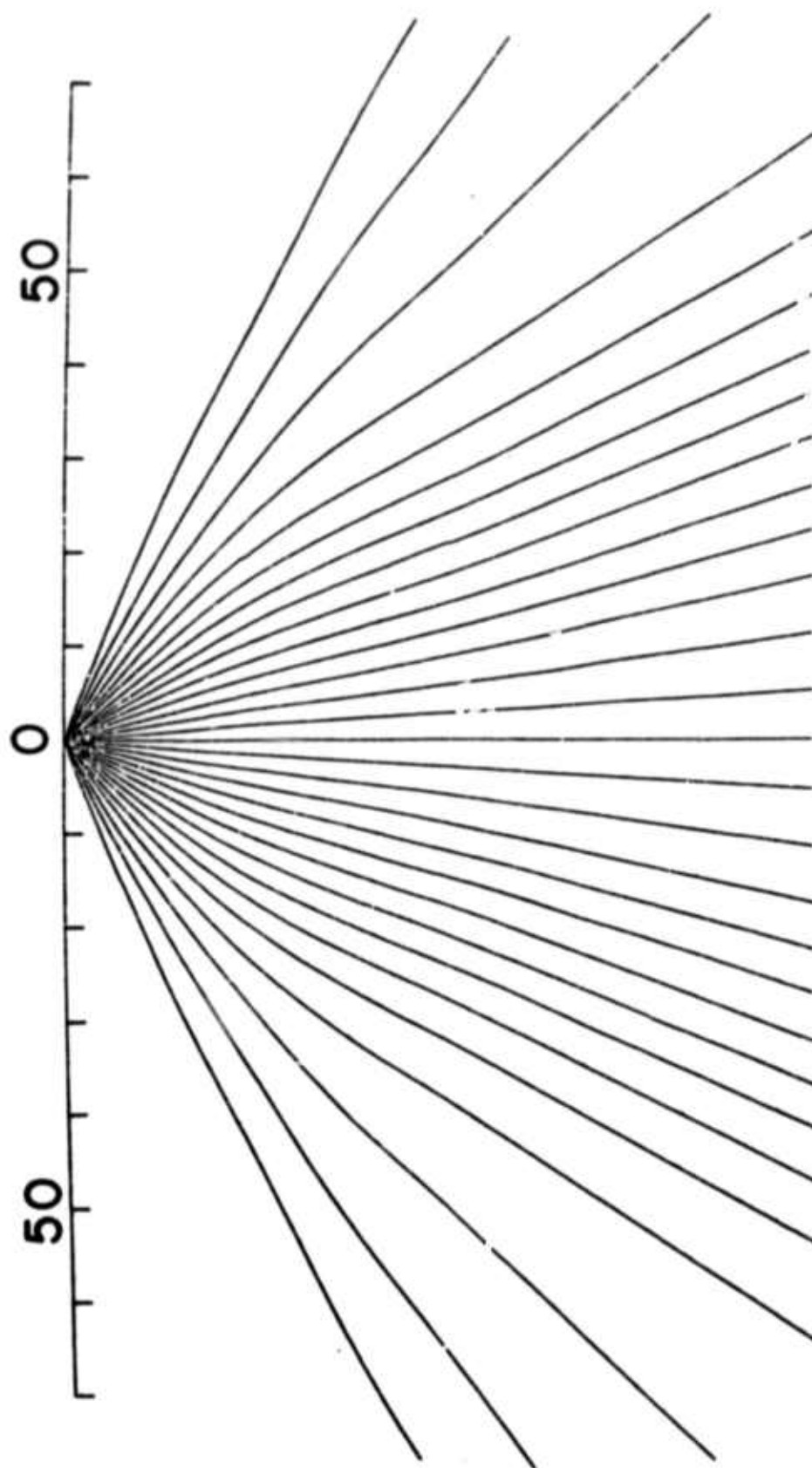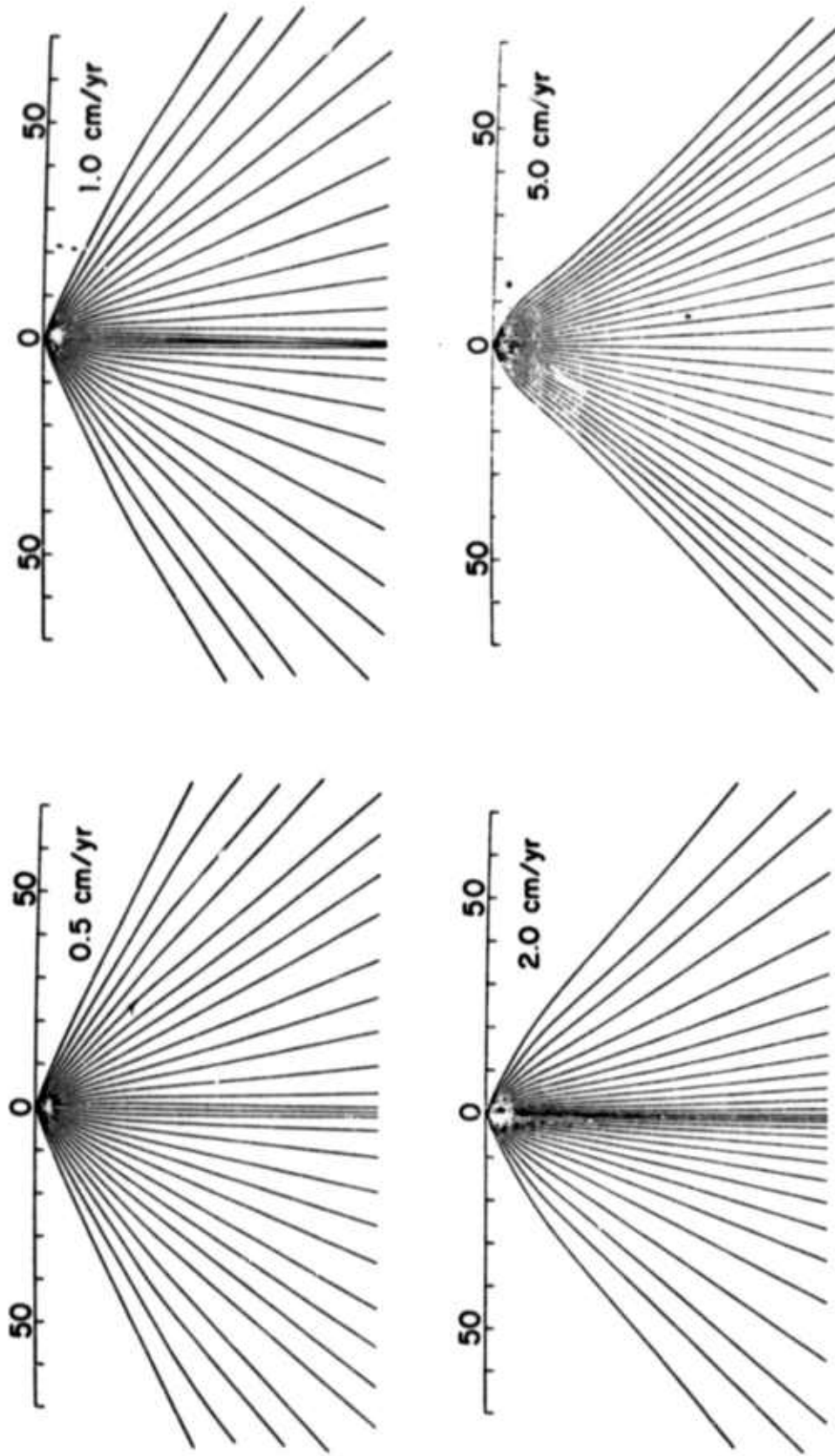Fig. 8

Fig. 9

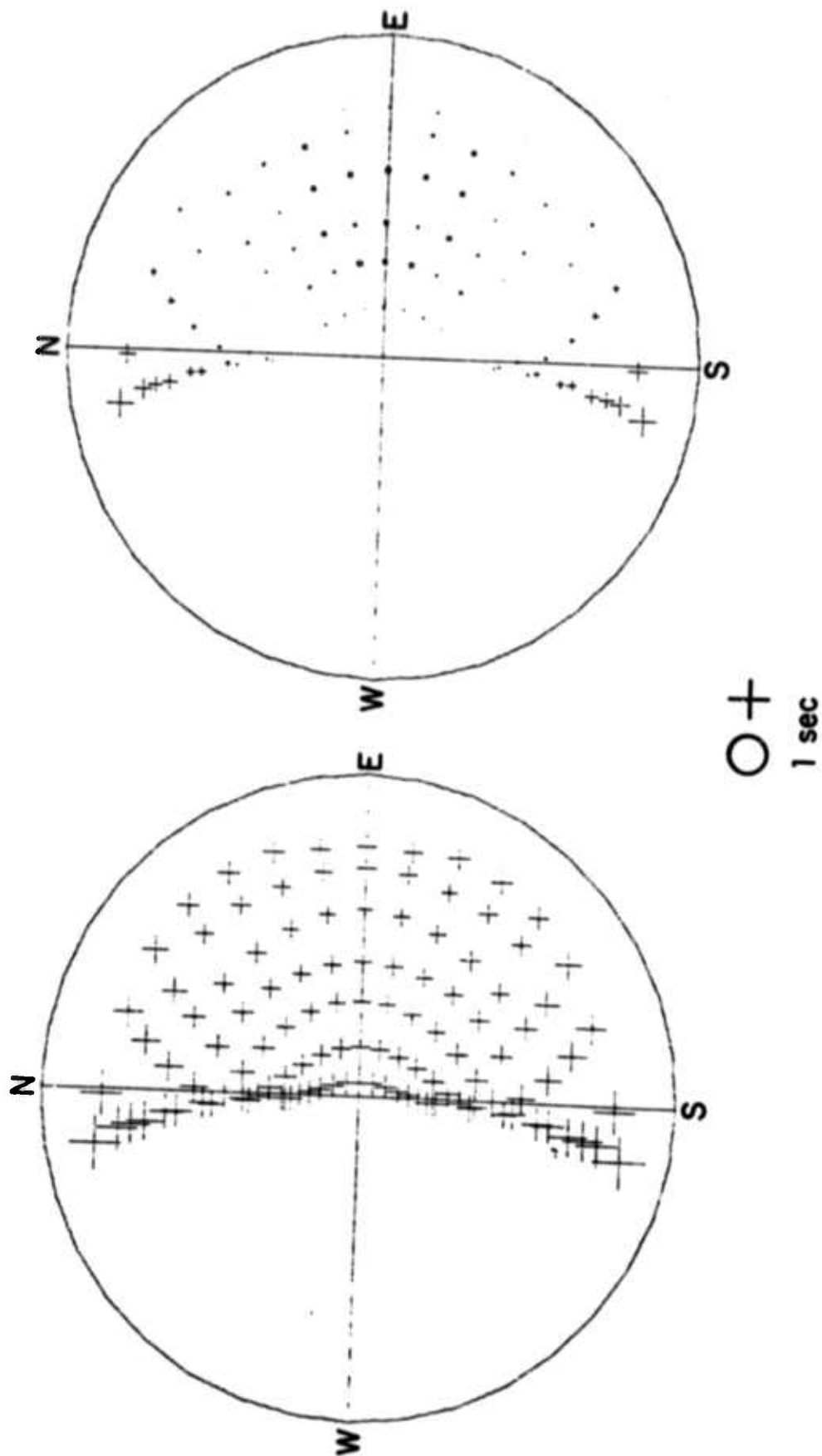Fig. 10

5. ARRAYS AND DATA PROCESSING

5.1 <u>Automatic Phase Identification With One and Two Large Aperture Seismic Arrays</u> by S. Shlien and M.N. Toksöz (abstract)

Schemes to automatically identify later phases using LASA and using LASA together with NORSAR were designed and tested. With a single array, phase identification was accomplished by searching for a P or PKP phase that could be associated with a particular later phase such as PP, PcP, etc. On the basis of the time interval between the signals, their slowness, and relative amplitudes the best phase interpretation was chosen by means of the Neyman-Pearson likelihood ratio test. With two arrays, detections from one array were checked against detections from the other array for signals originating from the same event.

Testing the schemes on the LASA and NORSAR Detection Logs 9 later phases per day were detected and 11 events per day were found common to the LASA and NORSAR detection logs. Confusion of later phases was very minor. The most serious problem was the identification of fictitious phases and events that occurred due to various coincidences.

5.2 An Event Recording System for Monitoring Small Earthquakes by Bruce P. Ambuter and Sean C. Solomon

Summary

To monitor small earthquakes on the ocean bottom or in remote areas on land, a seismic recording system should operate at low power for extended periods of time, should reproduce three components of ground motion with a large dynamic range, and should preferably be small and inexpensive. We describe such a system based on an event detector, which continuously surveys the background noise, sets a threshold, and triggers an inexpensive digital tape recorder when a seismic signal exceeds that threshold. Event recording offers the advantages over conventional continuous recording of more efficient use of storage capacity and easier later interpretation. A key element of the system is a continuously updated semiconductor buffer memory, which assures that first arrivals are included. Average power consumption is about a watt. The system design is easily adaptable to monitoring other types of rare events of unpredictable occurrence.

INTRODUCTION

The operation of a seismometer system in a remote or nearly inaccessible area has always posed logistical, mechanical and financial problems. Field instruments or temporary stations must operate efficiently at low power, particularly when continuous monitoring over long time intervals is desired. At the same time, such standard seismological tools as spectral analysis require that the data recording system have a broad or flexible frequency response and a wide dynamic range. Motivated primarily by a desire to monitor small earthquakes on the ocean bottom or at temporary land stations with a movable array of three-component seismometers, we developed a seismic recording package that meets these diverse requirements. The heart of the system, described in this paper, is an event recording scheme based on a continuously updated semiconductor memory.

There are two distinctly different methods for recording seismic data. The first is continuous storing of seismometer output. The second is event recording, i.e., editing data and storing only after a threshold has been exceeded. The first system is more simple to design. The second requires less storage capacity and makes later reading and interpreting of the data less time-consuming.

Conventional seismometer systems with adequate dynamic range for spectral analysis generally use continuous recording, either in the FM (frequency-modulation) or direct analog mode.

Each mode has both advantages and drawbacks. Direct analog recording is the easiest system to implement, requiring a minimum of components. Its main disadvantages are susceptibility to tape dropouts and non-linear low frequency response. With FM recording, there is a more uniform frequency response. However, there is a trade-off between tape speed and high frequency response that can unduly limit recording time. In addition, the recording speed stability is a critical parameter. In either system, the dynamic range is limited to about 40 db and the tape recorder is commonly large and expensive. None of these disadvantages are fatal, we should note, and many can be circumvented by careful design work (Dibble, 1964; Sacks, 1966; Muirhead and Simpson, 1972; Green, 1973). Continuous recording can also be performed with a digital recorder, though the size and cost of such a unit must necessarily be large for most recording times of interest.

An event recorder which continuously surveys the ambient noise at a recording site, sets a threshold, and triggers the recorder when a seismic signal exceeds the threshold, requires far less storage space and thus permits recording at fast tape speeds on a small, low-cost, low-power recorder. A difficulty with such a system, however, is that the trigger is more likely to be set off by the S wave or by another later arrival than by the often smaller P wave. Thus the valuable first cycles of wave motion would be lost.

The solution is to build a "memory" into the system, so that the recorder can store ata taken before the threshold detector was triggered. One such simple memory device is a small, endless tape loop with "write" and "read" heads separated by a distance along the tape corresponding to the largest probable S-P time. A second storage recorder is also required. Such a device has been used with some success to monitor micro-earthquakes (Omote et al., 1955; Aki et al., 1969; Hunt, 1969). A difficulty with such a system in the past has been the severe increase in tape noise after the thousand or more cycles necessary for operation times of up to a month. An alternative memory device using a single tape recorder and a rewind algorithm has recently been described by Choudhury and Houri (1973). Handicaps of their system are the regular periods when no signal can be recorded and a relatively short life for the recorder.

We describe in this paper a seismometer system that incorporates an automatic editor based on a semiconductor buffer memory instead of a tape loop. The principles of the editor were briefly outlined previously (Ambuter and Solomon, 1972). The semiconductor memory has the advantage of no moving parts to degrade with repeated use. The recorded seismic signal is in digital form, suitable for eventual spectral analysis. The instrument package we describe, because of our interest in small earthquakes, was designed with a specific set of requirements: (1) good response between 2 and 30 Hz frequency; (2) dynamic range of at least 40 db; (3) remote operation for

periods of a month or more; (4) low power; (5) low cost;
(6) small size and weight. Nonetheless, the general charac-
teristics of our system should be applicable to a wide
range of seismic recording problems.

EVENT DETECTOR

In Figure 1 is shown a detailed block diagram of the
event detector circuitry used in our system. Signals are
fed through a low-pass filter with a 30 Hz cut-off (Figure 2)
and are input to a short-term averager (STA) and, through a
digitally controlled switch, to a long-term averager (LTA).
The long- and short-term averagers both rectify and integrate
the input signal. The LTA has a time constant of 5 minutes,
which is much longer than the largest period of the seismic
signals we wish to record. The LTA output is therefore re-
presentative of the average background level or noise. The
STA has a time constant of 1 second and responds quickly to
changes in signal level. The output of the LTA and a portion
of the STA are continuously monitored by an event comparator.
The portion of the STA that is fed to the event comparator
determines the event threshold. Put simply, an event is de-
tected when the STA exceeds the threshold level.

Since we are dealing with an event recording system
with a finite storage capacity, one of the prime considera-
tions of the system is to maximize the ratio of real events

to spurious ones. Obviously a trade-off exists between the threshold setting and the number of events detected. Since both the seismic signals of interest and the noise may have substantial energy in the frequency band 2 to 30 Hz, restricting the event detection circuitry to look at a portion of this band would probably not result in improving the ratio of detected real events to spurious events. Preliminary tests have shown that for our system a threshold of 8 to 10 db minimizes the number of spurious events while allowing all real events with signal to noise adequate for analysis to be recorded.

In operation, the input to the LTA is digitally controlled through a switch and associated logic. Under no-event conditions, the switch is in position 1 (Figure 1) and the LTA reflects the average level of the incoming signals. When an event is detected, the switch is moved to position 2 and the output of the LTA is frozen. The reason for this is that if the LTA were allowed to respond to signal levels during an event in which the signal amplitude is significantly greater than the average background level, then the LTA would charge up and cause premature termination of the event. The LTA switch remains in position 2 until the STA falls below the threshold level. The system will continue to record until the STA level has been below the threshold level for a thirty second time period. This enables us to see the trailing edge of an event.

During an event the LTA output is fed into a feedback amplifier having a gain such that the slope of the LTA output level is slightly positive. This has minimal effect for events of short duration, say up to a minute. But for events which are longer than typically expected from small earth-quake sources, the LTA will charge up and eventually effect termination of recording. This minimizes the possibility of exhausting the event-recording storage capacity with data of no scientific interest. The LTA time constant was chosen to be longer than the longest signal period of interest, yet short enough to respond to noise build-up, thereby minimizing spurious triggering.

ANALOG CIRCUITRY

The analog circuitry (low-noise amplifiers, low-pass filters, variable-gain amplifiers, sample-and-hold amplifier, variable-gain logic control, and event detector) conditions the incoming seismic information through amplification and filtering and determines if an event has been observed. The digital circuitry (A-D converter, semi-conductor memory, timing, and control and format unit) samples the data from the output of the analog circuitry through the A-D converter and loads these data into the semi-conductor memory under the direction of the control and format unit. The event detector line is used to turn on a storage recorder and load the output of the buffer memory.

Seismic signals from the three-component seismometer (see Figure 2) are first amplified using a low-noise integrated-circuit amplifier, and are then passed through a 4-pole low-pass active filter network having a high-frequency cutoff of 30 Hz. The output from the low-pass filters is applied to the sample-and-hold circuitry, and then to the multiplier, which combines the three channels into one composite signal. One component of data output from the low-pass filter, generally the vertical component, goes to the event-detection circuitry previously described, and also to the variable-gain-amplifier control logic.

The variable-gain amflifier consists of an LTA and an associated decoder block. This LTA has a time constant of five minutes and responds to the average background or noise level. The LTA output is applied to the decoder block, which in turn sets the gain of the variable-gain amplifier. Thus the gain of the system is governed by the background noise level. This feature enables the seismic system to be placed in environments where the noise level is unknown or subject to variation and still realize maximum signal dynamic range. During an event the variable-gain LTA level is frozen and the system gain is recorded.

DIGITAL CONTROL CIRCUITRY

The operation of the remainder of the system, governed by the logic control and format unit, may be explained as follows:

1) The A-D converter upon command samples the analog input and generates an equivalent digital code. The system being described used an 8 bit A-D converter. In operation, the background noise is set at approximately one half of the least-significant-bit by the automatic gain control, allowing a signal dynamic range of 42 db.

2) The control and format unit then commands the A-D converter to load its 8-bit output words into the semi-conductor memory. The memory is made up of 1000-bit shift registers. The input data are shifted along until at some later time they appear at the output of the shift registers. The capacity of the memory is 2000 8-bit words for each data channel, a total that can easily be increased by adding more shift registers. To illustrate the time delay, if the sample rate were 200 samples/sec, then the digital output would be delayed 10 seconds.

During periods when the event detector is off, the buffer memory words just drop off the end of the shift register. When an event is detected, the storage recorder is turned on, and the output from the buffer memory is recorded.

3) The sequence of events that occurs when a seismic signal is detected is under the direction of the control and format unit. When an event is detected, the inputs to both long-term averagers are immediately inhibited. This is because the long-term average is meant to reflect the average background

noise, and therefore should not be allowed to respond to
event signal levels. Simultaneously, the tape recorder
motor is turned on and, after a delay during which the tape
motor comes up to speed, the buffer memory output is re-
corded. During the event, the system gain and the total
elapsed time, expressed in terms of seconds, minutes, hours,
and days, are recorded on the control track. Recording
continues until the threshold detector has returned to its
presignal "off" state for a period of 30 seconds.

TIMING AND STORAGE RECORDER

The timing signals necessary to run this system are
derived from a 5 MHz oscillator. The oscillator output is
fed into the time divider chain. Three sample speeds are
available: 125 Hz, 160 Hz, and 200 Hz.

The storage recorder is a Sony 800B four-speed, portable
tape recorder, modified by removing all the audio circuitry
and installing a five track digital head. The reel size is
five inches, allowing 2400 feet of recording tape. For a
200 Hz sample rate and a tape speed of 1 7/8 inches per
second, a recording time of four hours is possible. Propor-
tionately longer recording times may be obtained by using
slower sampling rates.

Three of the recorder's tracks are used for storing data
from the three input channels. The fourth track is used for

recording of system gain and associated timing marks. The
fifth track is for sync pulses. These sync pulses are used
to inform the tape playback unit that there are data on the
other four tracks and also to identify the relative bit posi-
tions of the words as they are read from the storage recorder.
By using a separate sync track, the system is relatively in-
sensitive to tape speed variations, either in the original
recording or in the playback mode. This is a big advantage
over FM or direct recording modes, as both of these approaches
are acutely sensitive to tape speed stability and impose
tight requirements on the storage recorder.

The data as recorded are not in a format compatible
with large computers. The tape must first be played back
through a processor unit which reconverts the tape head signals
into digital form. Data and control channels are then applied
to the accumulator of a small computer (PDP-7), which is pro-
grammed to read the information in the accumulator when the
sync channel produces a logic high. The decoded data may then
be readily formatted and written on an IBM-compatible tape.
Output from the same processor unit may also be fed into a
unit, containing D-A converters, which drives a multi-channel
chart recorder.

SYSTEM CHARACTERISTICS

A photograph of the system described above, suitable
for monitoring small earthquakes on land, is shown in Figure
3. Included in the figure are the circuit boards, storage

recorder, and geophones that constitute the functional part
of the system. All instrumentation aside from sensors and
batteries can fit into a suitcase of dimensions 9" x 10" x 12"
for land use into a 9 1/2" diameter I.D. cylinder for ocean-
bottom experiments. The weight of the system, again excluding
sensors and batteries, is about twenty pounds.

System power requirements are dependent on the stability
of the timing oscillator. When using relative arrival times
of P and S waves at array stations to locate small earthquakes,
a relative time accuracy of at least .01 sec is often desirable.
For land stations in areas where WWV radio can be received, a
timing stability of 1 part in 10^7 per day is sufficient. The
power drain for a system such as we describe with this timing
stability averages about three-quarters of a watt. For 1-month
recording times at stations remote from an external timing
reference, such as on the ocean bottom, an oven-controlled
oscillator with timing stability of 1 part in 10^9 per day is
necessary. The system power drain is then about 1 1/2 watts.

The voltages required, 12 volts and ±5 volts, may be
supplied by many types of batteries. We have found both lead-
acid batteries and magnesium batteries to be useful. Lead-
acid batteries are rechargeable, but are comparatively bulky.
Magnesium batteries are more expensive, but are much lighter.
Thirty days of system operation require about $120 worth of
either type of batteries.

The total component cost of the system shown in Figure 3, including geophones (4.5 Hz frequency), is approximately $2000 with the oven-controlled oscillator, and is $200 less with the less demanding timing requirements. About two man-weeks of construction time are necessary to assemble the complete system.

SYSTEM TESTS

The event-recording circuitry was tested using data from the Agassiz seismic observatory at Harvard, Massachusetts. The system sampling rate was 160 samples/sec, the buffer memory delay was 12.5 seconds, and the maximum signal frequency was 20 Hz. The signal from a short-period vertical seismometer was processed and output to a two-channel helicorder. The first channel of the helicorder had as its input the continuous output of the system's buffer memory. Input to the second helicorder channel was derived from the buffer memory output gated with the output of the event detector logic (which turns the storage recorder on and off). In such an operation, the first helicorder trace is a continuous representation of the incoming short-period data. The second trace is a straight line unless the signal threshold is exceeded, in which case the two helicorder traces are identical.

The threshold level was initially set at 3 db and gradually increased to a maximum value of 14 db. The number of

event triggerings per unit time depended strongly on the threshold level. At a detection threshold of 6 db, we recorded about 60 to 80 "events" per day, though the great majority were clearly noise rather than small earthquakes or explosions. At a detection threshold of 12 db, we recorded real seismic events only, less than 1 per day, though a few small signals from possible sources of interest were missed. An optimum threshold level for this site lies probably between 8 and 10 db. At this setting, the number of spurious triggers was minimized without missing any clearly identifiable events. At a different site, for instance one less noisy, the optimum threshold setting might be different.

Portions of helicorder recordings shown in Figure 4 illustrate typical detected events. The operation of the buffer memory delay is clearly illustrated in the figure; both noise prior to each event and the unambiguous first arrivals have been recorded. The system continued to record until the STA stayed below the threshold level for a period of 30 seconds.

CONCLUSIONS

We have described a seismic recording system that is ideal for monitoring small earthquakes in remote areas. The system is small, consumes little power, and is low in cost. This is in large part due to the latest advances in

integrated-circuit technology. For example, the 2000-word 8-bit memories in this system cost less than $100 and occupy an area of about 2 square inches on a circuit board. The dynamic range is large and may be readily extended by using a 10- or 12-bit A-D converter.

The system is insensitive to tape-speed variations, which are critical to other recording techniques. In playback mode, all that is required is to distinguish between a logic high and a logic low. Therefore the specifications of the storage recorder are not particularly stringent and a small, inexpensive reorder may be used.

This system may be readily modified to meet different applications. Sampling rate may be varied by a factor of up to 10 simply by changing one wire. Additional data channels may be added at a cost of $150 per channel. In applications where long-period data are of interest, the operation time could easily be extended to a year. It should be noted that the sensor need not be a geophone; thus the above system could be applied to other fields with minimal functional changes.

By design this system is self-editing, so that data analysis does not need to be preceded by a tedious search of voluminous tapes for useful data. The signals are recorded in digital form, suitable for eventual spectral analysis on a digital computer.

The details of the system described were designed for the specific aim of monitoring small earthquakes on the ocean-bottom or in remote land areas of relatively low seismicity.

Nonetheless, the requirements met by such a system are shared to some extent by such diverse experiments as seismic recording by unmanned planetary landers (Anderson et al., 1972), unmanned seismic observatories of a long-term or permanent nature, and even routine data processing in real-time of a conventional seismometer network. Instruments of similar design should see widespread implementation by seismologists in the next few years.

ACKNOWLEDGEMENTS

REFERENCES

Aki, K., M. Hori, and H. Matumoto (1969). Microaftershocks observed at a temporary array station on the Kenai Peninsula from May 19 to June 7, 1964, Coast and Geodetic Survey Publication 10-3, 131-156.

Ambuter, B.P., and S.C. Solomon (1972). An automatic seismic editing system (abstract), EOS Trans. Amer. Geophys. Un., 53, 1051.

Anderson, D.L., R.L. Kovach, G. Latham, F. Press, M.N. Toksöz, and G. Sutton (1972). Seismic investigations: The Viking Mars Lander, Icarus 16, 205-216.

Choudhury, M.A., and A. Houri (1973). A low-cost observatory tape recorder, Bull. Seism. Soc. Am. 63, 877-884.

Dibble, R.R. (1964). A portable slow motion magnetic tape recorder for geophysical purposes, N.Z.J. Geol. Geophys. 7, 445-465.

Green, R. (1973). A portable multi-channel seismic recorder and a data processing system, Bull. Seism. Soc. Am., 63, 423-431.

Hunt, D.P. (1969). A selected events recorder for seismic applications, Mackay School of Mines Technical Report, University of Nevada, Reno, 141 pp.

Muirhead, K.J., and D.W. Simpson (1972). A three-quarter
    watt seismic station, Bull. Seism. Soc. Am. 62,
    985-990.

Omote, S., S. Miyamura, and Y. Yamazaki (1955). Triggered
    magnetic tape recorder for routine seismic observation,
    Bull. Earthquake Res. Inst., Univ. Tokyo 33, 397-409

Sacks, I.S. (1966). A broad-band large dynamic range seismo-
    graph, in The Earth Beneath the Continents, ed. by
    J.S. Steinhart and T.J. Smith., Amer. Geophys. Un. Mon.
    10, 543-553.

FIGURE CAPTIONS

Figure 1. Block diagram of event detector circuitry.

Figure 2. Block diagram of complete seismic recording system.

Figure 3. Photograph of system suitable for remote operation
on land, disassembled for clarity.

Figure 4. Examples of signals which triggered event-detection
circuitry. Source are probably quarry blasts. Times
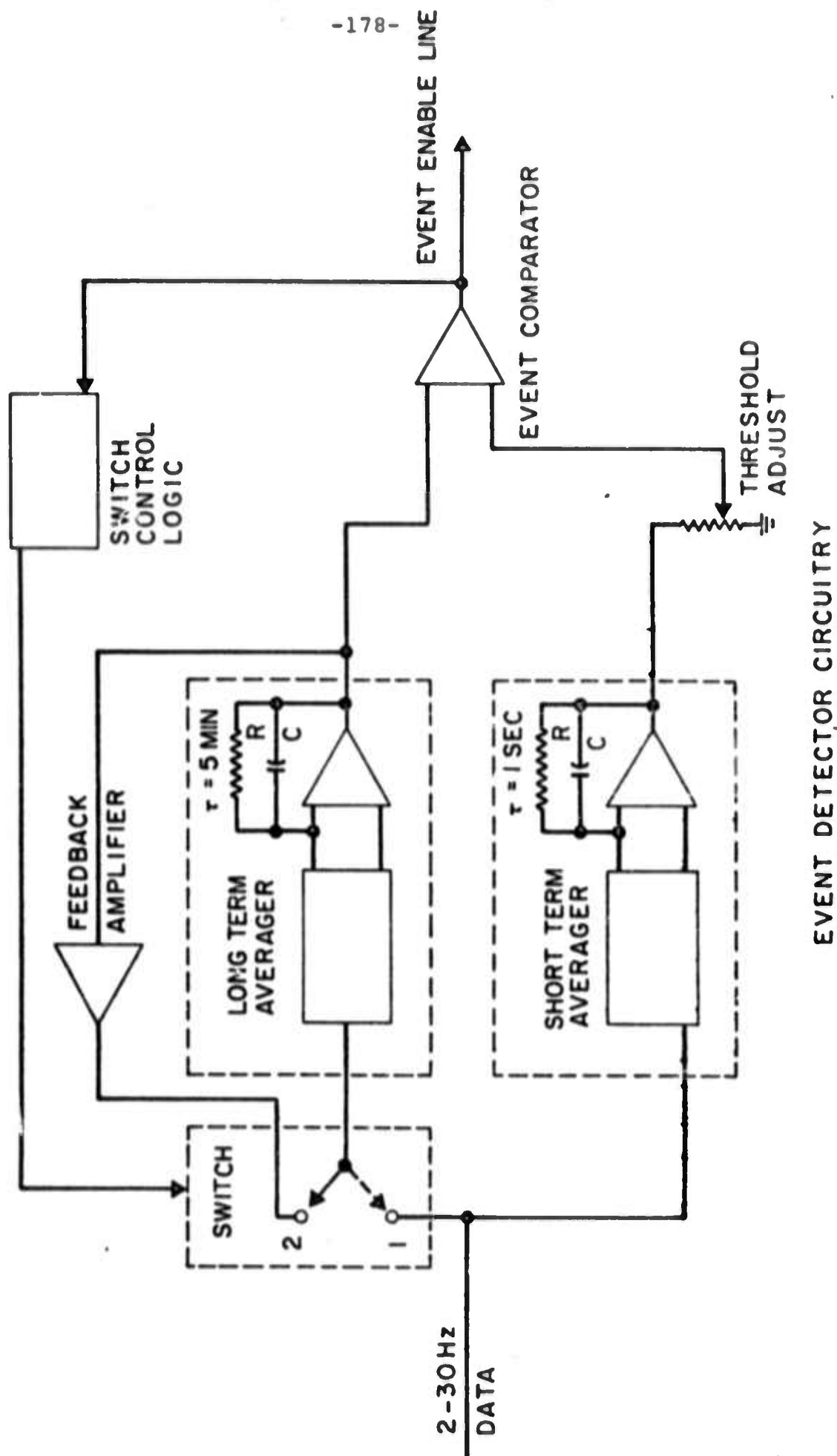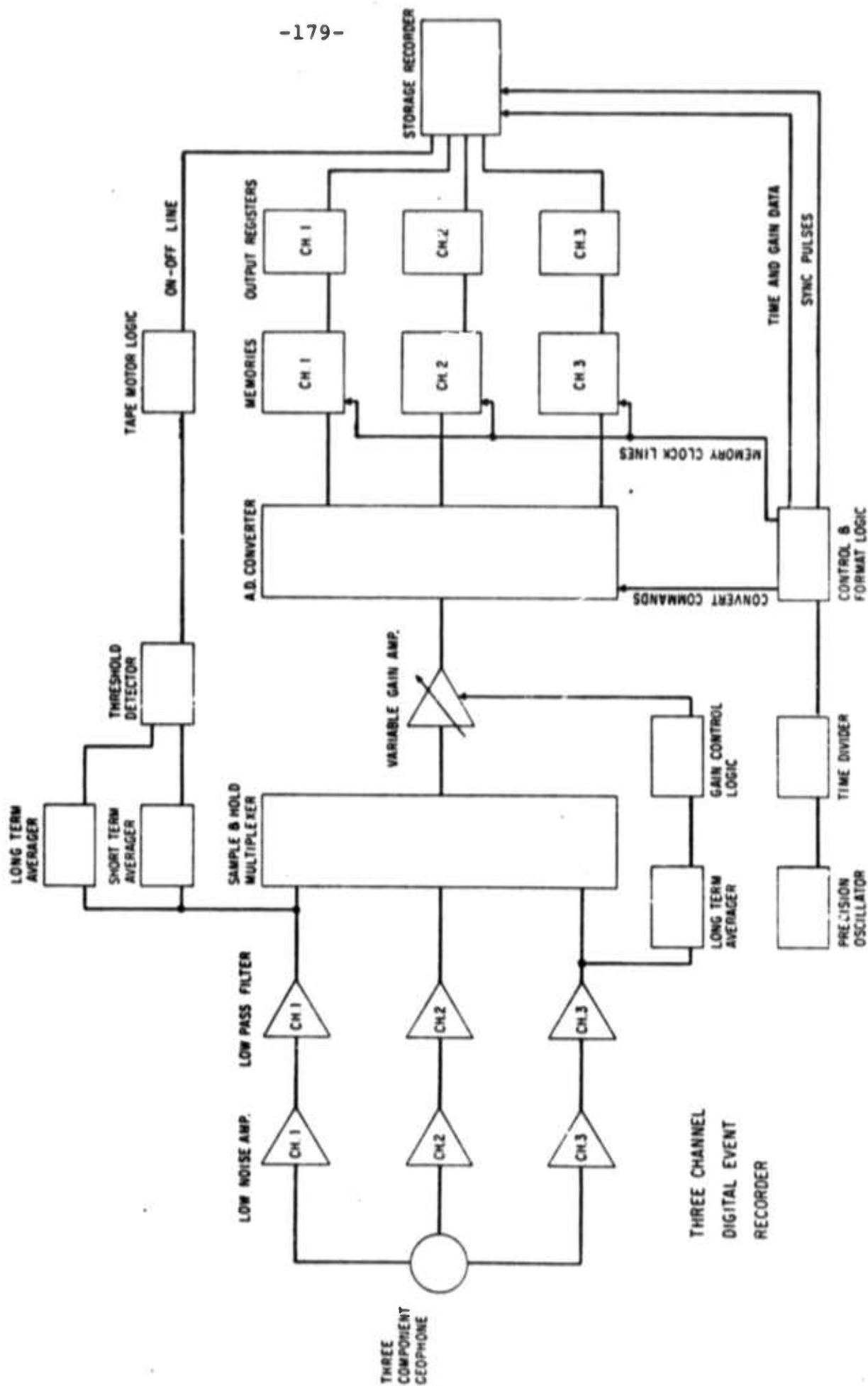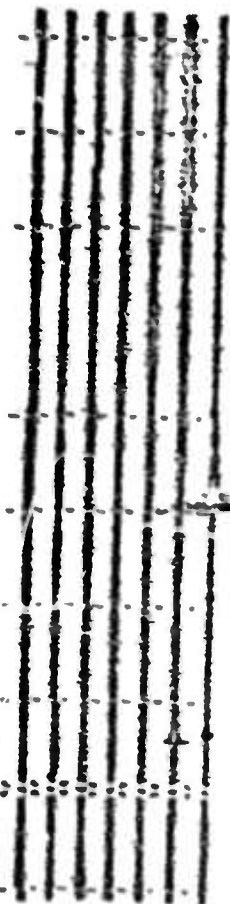are in G.M.T. Tic marks are generally spaced at 1 minute
intervals.

EVENT DETECTOR CIRCUITRY
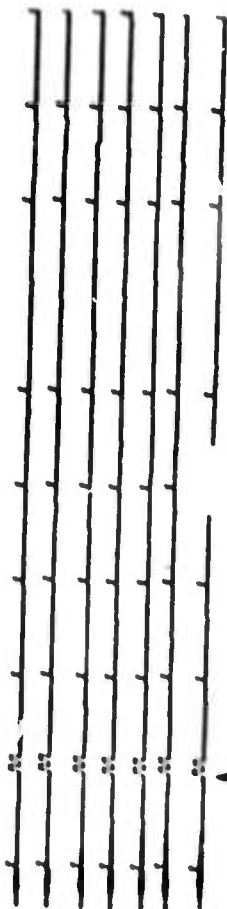
Figure 1

Figure 2

HARVARD, MASS.

15 NOVEMBER 1973

CONTINUOUS CHANNEL
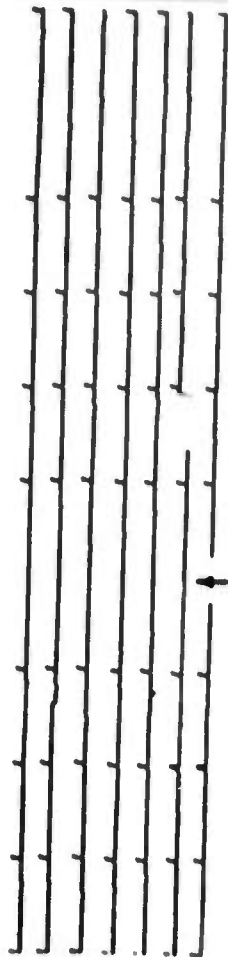
EVENT CHANNEL

20:40

22:00

Figure 4

6.   PUBLICATIONS DURING CONTRACT YEAR

Abe, K., Fault parameters determined by near- and far-field
data: The Wakasa-Bay earthquake of March 26, 1963,
submitted to Bull. Seism. Soc. Am., 1974a.

Abe, K., Seismic displacement and ground motion near a fault:
the Saitama earthquake of September 21, 1931, submitted
to J. Geophys. Res., 1974b.

Aki, K., M. Bouchon and P. Reasenberg, Seismic source function
for an underground nuclear explosion, Bull. Seism. Soc.
Am., 64, 131-148, 1974.

Ambuter, B.P. and S.C. Solomon, An event recording system for
monitoring small earthquakes, Bull. Seism. Soc. Am.,
in press, August 1974.

Brown, R., Precursory changes in Vp/Vs before strike-slip
events, Proc. Conf. Tectonic Problems of the San Andreas
Fault System, R.L. Kovach and A. Nur, eds., Geological
Sciences, Vol. XIII, Stanford University, 1973.

Kuster, G. and M.N. Toksöz, Velocity and attenuatio. of seismic
waves in two-phase media: I. Theoretical formulations,
Geophysics, in press, 1974.

Reasenberg, P. and K. Aki, A precise, continuous measurement
of seismic velocity for monitoring in situ stress, J.
Geophys. Res., 79, 399-406, 1974.

Richter, F.M. and C.E. Johnson, Stability of a chemically
  layered mantle, J. Geophys. Res., 79, 1635-1639, 1974.

Rosenman, M. and S.J. Singh, Quasi-static strains and tilts
  due to faulting in a viscoelastic half-space, Bull.
  Seism. Soc. Am., 63, 1737-1752, 1973a.

Rosenman, M. and S.J. Singh, Stress relaxation in a semi-
  infinite viscoelastic earth model, Bull. Seism. Soc. Am.,
  63, 2145-2154, 1973b.

Shlien, S. and M.N. Toksöz, Automatic event detection and
  location capabilities of large aperture seismic arrays,
  Bull. Seism. Soc. Am., 63, 1275-1288, 1973.

Shlien, S. and M.N. Toksöz, Automatic phase identification
  with one and two large aperture seismic arrays, Bull.
  Seism. Soc. Am., 64, 221-233, 1974.

Singh, S.J., Generation of SH-type motion by torsion-free
  sources, Bull. Seism. Soc. Am., 63, 1189-1200, 1973.

Singh, S.J. and M. Rosenman, On the disturbance due to a
  spherical distortional pulse in an elastic medium,
  Pure and Appl. Geophys. 110, 1946-1954, 1973.

Singh, S.J. and M. Rosenman, Quasi-static deformation of a
  viscoelastic half-space by a displacement dislocation,
  Phys. Earth Planet. Interiors, 8, 87-101, 1974.

Solomon, S.C., Shear wave attenuation and melting beneath the
  mid-Atlantic ridge, J. Geophys. Res., 78, 6044-6059, 1973.

Solomon, S.C. and R.G. Butler, Prospecting for dead slabs, Earth Planet. Sci. Lett., 21, 421-430, 1974.

Solomon, S.C. and B.R. Julian, Seismic constraints on ocean-ridge mantle structure: Anomalous fault-plane solutions from first motions, Geophys. J. Roy. Astr. Soc., in press, 1974.

Toksöz, M.N., N. Sleep and A.T. Smith, Evolution of the downgoing lithosphere and the mechanisms of deep focus earthquakes, Geophys. J. Roy. Astr. Soc., 35, 285-310, 1973.

7. THESES COMPLETED DURING CONTRACT YEAR

Chapman, E.D., Structure and tectonics of the Arctic
region, S.M. Thesis, M.I.T., June 1973.

Wang, C.F., Elastic wave propagation in homogeneous
transversely isotropic medium with symmetry axis
parallel to the free surface, S.M. Thesis, M.I.T.,
September 1973.